

## DISSERTATION

# Strong-Field Dynamics in Small Molecules

ausgeführt zum Zwecke der Erlangung des akademischen Grades einer  
Doktorin der technischen Wissenschaften  
unter der Leitung von

Univ.-Prof. Dr. Joachim Burgdörfer

E136 Institut für Theoretische Physik  
Technische Universität Wien

und

Univ.-Prof. Dr. Stefanie Gräfe

Institut für Physikalische Chemie  
Friedrich-Schiller Universität, Jena

eingereicht an der  
Technischen Universität Wien  
Fakultät für Physik

von

**Dipl.-Ing. Mag. Katharina Doblhoff-Dier**

e0525856  
Spitzweidenweg 59  
D-07743 Jena

Wien, im September 2014



## Abstract

Steering and guiding molecular reactions and molecular dynamics is a long standing goal in chemistry and physics. Strong and ultrashort infrared pulses with intensities around  $10^{14}$  W/cm<sup>2</sup> and pulse lengths of less than 5 fs, corresponding to 1-2 optical cycles, allow influencing the electronic and nuclear motion on femtosecond and even sub-femtosecond timescales. In order to analyse and interpret experimental results, detailed theoretical investigations are necessary.

This work focusses on three recent experiments, one addressing the electronic dynamics in molecules subject to intense fields and two addressing the strong field control of nuclear dynamics. This work provides an analysis of the processes involved in order to identify the relevant physical mechanisms governing the dynamics. This is achieved by applying a large variety of different approaches from physics and chemistry.

More precisely, the first part of this thesis deals with the strong field ionization of H<sub>2</sub><sup>+</sup> in circularly polarized fields and the resulting photoelectron spectrum, which is studied within a semi-classical model. The focus is to provide an analysis and interpretation of the observed rotation of the photoelectron momentum distribution compared to predictions from the strong-field approximation (SFA). The work shows that classical trajectory Monte Carlo calculations can reproduce and explain many experimentally observed features in the molecular strong-field ionization of H<sub>2</sub><sup>+</sup>: the classical trajectory calculations thus provide a simple approach to testing the influence of the Coulomb potential and multiple ionization bursts. For instance, the model allows interpreting the counter-intuitive intensity independence of the angular photoelectron spectrum as a result of two rivalling processes: the intensity dependence of the tunnel exit and the field interaction in the continuum. The model also illustrates the importance of the initial momentum distribution assigned to the trajectories on the momentum and angle resolved photoelectron spectrum and the rotation thereof. Multiple ionization bursts are found not to be responsible for the observed rotation of the photoelectron spectrum compared to SFA predictions.

The second and third part of the thesis deal with the interpretation of experiments investigating the possibility to control fragmentation reactions of C<sub>2</sub>H<sub>2</sub> using strong few-cycle laser pulses:

The second part deals with the reaction control of C<sub>2</sub>H<sub>2</sub> using the carrier-envelope phase of few-cycle infra-red laser fields as control tool. The combined analysis of quantum chemical calculations, quantum dynamical calculations, and a semi-classical model

for recollisional ionization allows identifying an energy threshold effect in recollisional ionization as the main control mechanism. Other influences, such as field excitations, are found to be of minor importance. The novel control mechanism discovered in the course of this work is likely to allow fragmentation control for a large number of small molecules.

In the third part of the thesis, the reaction control of  $C_2H_2$  via molecular alignment is investigated. A study of the alignment dependence of sequential ionization allows the qualitative and quantitative reproduction of several experimentally observed features. The alignment dependence of sequential ionization is thereby studied using both, a TD-DFT approach and a tunnel-ionization approach based on the Dyson orbital formalism. Although the two methods depend on different approximations and simplifications, the results are found to be consistent. For some fragmentation channels, recollisional ionization is found to play an important role. It is shown that the electron impact process, which is often neglected in models, may have a significant influence on the alignment dependence of recollisional ionization. This is illustrated by calculating singly-differential electron-impact ionization cross-sections within several different approximations. Field driven dipole transitions, which show a strong alignment dependence, have only little influence on the resulting fragmentation yield at the experimentally relevant intensities due to the small transition probabilities.



## Zusammenfassung

Chemische Reaktionen und molekulare Dynamik effizient zu kontrollieren und zu steuern ist nicht nur ein großes Ziel in der Grundlagenforschung, sondern auch von großem industriellen Interesse. Starke, ultrakurze Laserpulse mit Intensitäten um  $10^{14}$  W/cm<sup>2</sup> und Pulslängen, die nur wenige Schwingungsperioden umfassen, erlauben die Bewegung von Elektronen und Kernen auf einer Femtosekunden-Skala und sogar darunter zu kontrollieren. Die Analyse und Interpretation von Experimenten, die diese Möglichkeit belegen, erfordert jedoch Modellbildungen, die nur auf theoretischen Ansätzen beruhen können.

Ziel dieser Arbeit ist die Analyse von drei jüngst durchgeführten Experimenten. Fokus der Experimente war die Kontrolle sowohl der nuklearen als auch der elektronischen Dynamik in kleinen Molekülen. Die vorliegende theoretische Arbeit gibt einen Einblick in die zugrundeliegenden Prozesse und erlaubt es die relevanten Prozesse, die die Dynamik grundlegend steuern, zu identifizieren und zu verstehen. Um das zu erreichen werden verschiedene Ansätze aus der Physik und der Chemie angewandt und vereint.

Die Arbeit ist in drei Teilen strukturiert: Der erste Teil befasst sich mit der Starkfeld-Ionisation von  $H_2^+$ . Die folgenden zwei Teile beschäftigen sich mit der Analyse von Experimenten zur Kontrolle von chemischen Reaktionen, namentlich mit der Kontrolle der Fragmentierung von  $C_2H_2$  mittels der “carrier-envelope” Phase von ultrakurzen Pulsen und mittels der relativen Ausrichtung zwischen Molekül und Polarisationsachse.

Ziel des ersten Teiles der Arbeit ist es, Resultate von experimentell gemessenen Photoelektronenspektren von  $H_2^+$  in zirkular polarisierten Feldern zu interpretieren. Der Fokus liegt dabei auf der Analyse der experimentell beobachteten Rotation des winkelaufgelösten Photoelektronenspektrums relativ zu Vorhersagen, die auf Starkfeld-Näherungen beruhen. Zu diesem Zweck wurde ein semi-klassisches Modell entwickelt. Die vorliegenden Resultate zeigen, dass klassische Trajektorien Monte Carlo Rechnungen viele experimentelle Resultate korrekt widerspiegeln. In Folge dessen erlauben die semi-klassischen Rechnungen eine einfache und intuitive Interpretation von verschiedenen Einflussfaktoren, wie dem anisotropen Coulomb Potential des Ions und dem komplexen zeitlichen Verhalten der Ionisation. Dadurch ermöglichen die Rechnungen beispielsweise eine Interpretation der auf den ersten Blick widersinnig erscheinenden sehr schwachen Intensitätsabhängigkeit des Photoelektronenspektrums: Laut der semi-klassischen Analyse resultiert diese aus zwei konkurrierenden Prozessen mit gegensinniger Intensitätsabhängigkeit. Weitere Effekte illustrieren den Einfluss des Startimpulses der Trajektorien. Multiple-Ionisationsereignisse pro Laserperiode spielen laut dem semi-klassischen Modell jedoch

keine wesentliche Rolle für die resultierende Winkelabhängigkeit des Photoelektronenspektrum.

Der zweite Teil der Arbeit beschäftigt sich mit größeren Molekülen. Die Experimente zur Zerfallskontrolle von  $C_2H_2$  durch gezielte Kontrolle der “carrier-envelope” Phase werden anhand von quantenchemischen Rechnungen, Quantendynamik-Simulationen und semi-klassischen Modellen interpretiert. Als grundlegender Regelungsmechanismus wurde ein Energie-Schwellenwert-Effekt in der Doppelionisation via Elektronen-Rekollision identifiziert. Andere Einflüsse, so wie die “carrier-envelope” Phasenabhängigkeit von Feldanregungen, sind zwar vorhanden, dürften aber eine untergeordnete Rolle spielen. Der neu entdeckte Energie-Schwellenwert-Effekt könnte eine Fragmentierungskontrolle in einer ganzen Reihe von Molekülen erlauben.

Der dritte Teil der Arbeit beschäftigt sich mit der Kontrolle des Zerfalls von  $C_2H_2$  mittels der relativen Ausrichtung der Laserpolarisationsachse zur Molekülachse. Mittels eines Modells, das die sequentielle Ionisation beschreibt, konnte sowohl qualitative als auch quantitative Übereinstimmung mit den experimentellen Daten für mehrere Zerfallskanäle erzielt werden. Das Modell basiert auf TD-DFT Rechnungen und einem effektiven Einteilchenmodell zur Tunnel-Ionisation. Obwohl diese beiden Methoden auf unterschiedlichen Näherungen beruhen, sind die so erzielten Ergebnisse konsistent. Für einige Zerfallskanäle konnte gezeigt werden, dass Elektronenstoßionisation nach Elektronenrückstreuung des primären Elektrons eine wesentliche Rolle spielt. In diesem Zusammenhang konnte anhand von vereinfachten differentiellen Wirkungsquerschnitten gezeigt werden, dass der Stoßprozess selber einen nicht zu vernachlässigenden Einfluss auf die Winkelabhängigkeit von Elektronen-Rückstoß-Ionisation haben könnte. Dieser Stoßprozess wird üblicherweise in der Analyse der Winkelabhängigkeit von Elektronen-Rückstoß-Ionisation vernachlässigt. Die vorliegenden Rechnungen legen jedoch nahe, dass die Winkelabhängigkeit der Stoßquerschnitte in eine Gesamtanalyse des Prozesses eingehen sollte. Dagegen konnte gezeigt werden, dass die Winkelabhängigkeit von Dipolanregungen zwar stark ist, jedoch aufgrund ihrer relativ kleinen Wahrscheinlichkeit bei den verwendeten Intensitäten keine wesentliche Rolle in der Kontrolle des molekularen Zerfalls spielt.

## Acknowledgements

My last three years, the way to my PhD, were like a hike in the mountains: Sometimes the way would be stony and harsh and yet there would be the occasional flower to admire. But while the way was often beautiful, sometimes stony and always a challenge, it was most certainly not a path to be followed on my own. Many people, scientists and non-scientists, gave me a helping hand when climbing up the slope, or were simply there to talk with. I would like to thank all these people because they did not only make the goal achievable, but were and will be also my friends and companions.

While I will not be able to give an exhaustive list of all the people who took an important part in my last three years I would like to name some people personally. I will start with my PhD-advisor Dr. Stefanie Gräfe and my experimental collaborators Dr. Markus Kitzler and Xinhua Xie:

*Dear Steffi, I would like to thank you: thank you for introducing me to the exciting world of chemistry, thank you for allowing me to get on your nerves with all my questions, thank you for your scientific and non-scientific advice! You always thought that I do not believe you when you explained things, but that was one of the rare occasions on which you were wrong: you taught me to see results as achievements and your advice was often an important guidepost for me - a guidpost both, on the way through my thesis work and on my way to stand on my own two legs.*

*Dear Markus, I had great fun interpreting your absolutely cool experimental results. Theoretical physics would be an awfully dry subject without experimental collaborations! My discussions with you, Xinhua and Steffi were always a huge motivation-boost for me: there is actually somebody who is interested in my results! And you would always reveal so many scientific riddles that wanted to be solved by me!*

Then, I would like to thank Dr. Joachim Burgdörfer and his group, especially Paul Tiwald, Georg Wachter and Dr. Florian Libisch:

*Joachim, you always managed to fascinate me when establishing cross-connections I hadn't been aware of before and when showing how simple the theory of quantum physics actually is. You roused my ambition in wanting to understand it all! I was always welcomed in your group, where I felt very much at home.*

*Having friends at the institute only a door away was very important for me. Many a small problem was solved casually, while having a nice chat with you, Georg and Paul.*

*Dear Florian, I do not think you ever realized, but as a matter of fact, you might not have been quite innocent in my choice to do my PhD in quantum physics! Thank you!*

I would also like to thank Dr. André Staudte for his data and Dr. Konsatinos Dimitriou for helpful discussions.

*Dear André, unfortunately I didn't have the chance to get to know you in person. I would be very curious to learn who is behind these kind emails! Thank you for sending me your data and allowing me to reproduce them. This is a favour I would not take for granted.*

This already brings me to my family and my friends. I do not know how they do it, but my family is simply the best you could have.

*Thank you for being my haven in stormy waters and calm seas, thank you for giving me a place where I do not have to prove myself. Veronika, you are the best big sister one could have! Thank you and Stefan for reading my thesis, when you should actually be reading yours.*

*Dear Pierre, thank you for being there and for being so unbelievably patient! I am really lucky that you found me!*

Since these are the acknowledgements, this is probably also the best place to acknowledge financial support: during my PhD, I was part of the the International Max Planck Research School for Advanced Photon Science. This excellently organized doctoral college is not only invaluable for a theoretical physicist, since it opens the door to experimental collaborations and friendship, the research school also funded my trip to a conference and a summer school for which I could not be refunded by the university. I greatly enjoyed both of them and profited much!

I would like to conclude these acknowledgements by saying that I really enjoyed my work. It was fascinating and capturing and gave me the chance to dig deep into quantum theory and the numerics of calculations - it gave me the chance to learn.

Katharina Doblhoff-Dier

## Curriculum Vitae

Name: Katharina Doblhoff-Dier

Date of Birth: 13 May 1987

Nationality: Austrian

### Education

Since 03/2011: PhD program at the Vienna University of Technology, Austria  
Thesis title: Strong-field dynamics in small molecules  
PhD advisors: Dr. S. Gräfe and Dr. J. Burgdörfer

Since 04/2011: Member of the International Max Planck Research School for Advanced Photon Science

04/2011: Graduation diploma in Geophysics (passed with distinction)  
University of Vienna, Austria; Thesis title: Seismic signal analysis using polarization attributes

06/2010: Graduation diploma in Technical Physics (passed with distinction)  
Vienna University of Technology, Austria; Thesis title: Assessment of technological approaches for exhaust mass flow measurement

2008–2009: Study year abroad; University of Calgary, Canada

2006–2011: Study of Geophysics; University of Vienna, Austria

2005–2010: Study of Technical Physics; Vienna University of Technology, Austria

06/2005: School leaving examination; Gymnasium Billrothstraße 26-30, Vienna, Austria

01/2003–06/2003: Term abroad; Wakefield Girls' High School, Wakefield, England

### Affiliations

09/2013–09/2014: Institute for Physical Chemistry  
Friedrich-Schiller University, Germany

03/2011–08/2013: Institute for Theoretical Physics  
Vienna University of Technology, Austria

## Publications in refereed journals

- Thesis related      X. Xie, K. Doblhoff-Dier, H. Xu, S. Roither, M. S. Schöffler, D. Kartashov, S. Erattupuzha, T. Rathje, G. G. Paulus, K. Yamanouchi, A. Baltuška, S. Gräfe, and M. Kitzler. Selective control over fragmentation reactions in polyatomic molecules using impulsive laser alignment. *Phys. Rev. Lett.*, 112:163003, 2014.
- K. Doblhoff-Dier, K. I. Dimitriou, A. Staudte, and S. Gräfe. Classical analysis of Coulomb effects in strong-field ionization of  $H_2^+$  by intense circularly polarized laser fields. *Phys. Rev. A*, 88(3):033411, 2013.
- X. Xie, K. Doblhoff-Dier, S. Roither, M. S. Schöffler, D. Kartashov, H. Xu, T. Rathje, G. G. Paulus, A. Baltuška, S. Gräfe, and M. Kitzler. Attosecond-recollision-controlled selective fragmentation of polyatomic molecules. *Phys. Rev. Lett.*, 109:243001, 2012.
- others                 R. Pazourek, S. Nagele, K. Doblhoff-Dier, J. Feist, C. Lemell, K. Tökési, and J. Burgdörfer. Probing scattering phase shifts by attosecond streaking. *J. Phys. Conferene Series*, 388 (Part 1):012029, 2012.
- R. Pazourek, S. Nagele, K. Doblhoff-Dier, J. Feist, C. Lemell, K. Tökési, and J. Burgdörfer. Probing scattering phase shifts by attosecond streaking. *J. Phys. Conferene Series*, 388 (Part 2):022096, 2012.
- S. Nagele, R. Pazourek, J. Feist, K. Doblhoff-Dier, C. Lemell, K. Tökési, and J. Burgdörfer. Time-resolved photoemission by attosecond streaking: extraction of time information. *J. Phys. B: At. Mol. Phys.*, 44:081001, 2011.
- K. Doblhoff-Dier, K. Kudlaty, M. Wiesinger, and M. Gröschl. Time resolved measurement of pulsating flow using orifices. *Flow Measurement and Instrumentation*, 22:97–103, 2011.
- T. P. Peixoto, K. Doblhoff-Dier, and J. Davidsen. Spatiotemporal correlations of aftershock sequences. *Journal of Geophysical Research*, 115:B10309, 2010.

# Contents

Abstract	i
Zusammenfassung	iii
Acknowledgements	v
Curriculum Vitae	vii
<b>Introduction</b>	<b>5</b>
<b>I. Theory</b>	<b>9</b>
I.1. Ultra-short pulses and the carrier-envelope phase	9
I.2. Strong-field molecule interaction	11
I.2.1. Strong-field physics	11
I.2.2. Strong-field ionization	11
I.2.3. Strong-field approximation (SFA)	13
I.2.4. The three step model	14
I.2.5. Laser-matter interactions in the Schrödinger equation	15
I.3. Molecular quantum dynamics	19
I.3.1. The field-free, non-relativistic molecular Hamiltonian	19
I.3.2. The Born-Oppenheimer and Born-Huang approximation	20
I.3.3. Field excitations in Born-Huang approximation	23
I.4. Electronic structure Methods	27
I.4.1. Hartree-Fock method	27
I.4.2. Electron correlation methods	29
I.4.3. Density functional theory (DFT) and time-dependent DFT (TDDFT)	32
I.4.4. Quantum Chemistry software and basis sets	34
I.5. Electron scattering and impact ionization	35

<b>II. Numerical methods</b>	<b>37</b>
II.1. Solving the nuclear time-dependent Schrödinger equation	37
II.1.1. Basis representation	37
II.1.2. Time propagation and the split-operator method	39
II.1.3. Calculating eigenfunctions - Imaginary time propagation	40
II.1.4. Grid size, resolution and absorbing boundaries	41
II.2. Classical trajectory Monte Carlo	43
II.2.1. The Runge-Kutta-Fehlberg method	43
II.2.2. Gaussian distributed random numbers	44
<b>III. Strong-field ionization of <math>\text{H}_2^+</math> in circularly polarized light</b>	<b>47</b>
III.1. Introduction	47
III.2. The model	48
III.3. Numerical results and discussion	55
III.4. Summary and Conclusion	66
<b>IV. Reaction control of <math>\text{C}_2\text{H}_2^{2+}</math> via the carrier-envelope phase</b>	<b>69</b>
IV.1. Introduction	69
IV.2. Experimental results	70
IV.3. Potential landscape of acetylene and its cations	73
IV.3.1. The neutral species	73
IV.3.2. The cation	74
IV.3.3. The dication	74
IV.4. Discussion of possible fragmentation scenarios	78
IV.5. CEP dependence of field excitation processes	81
IV.6. CEP dependence of recollisional ionization	83
IV.6.1. Description of the model	84



IV.6.2. Results and Discussion	86
IV.7. Conclusion	90
<b>V. Reaction control of <math>C_2H_2^{2+}</math> via alignment</b>	<b>91</b>
V.1. Introduction	91
V.2. Experimental results	91
V.3. Alignment dependence of sequential ionization	95
V.3.1. Time-dependent density functional theory approach (TD-DFT)	97
V.3.2. Comparison of TDDFT with a Dyson orbital approach	104
V.3.3. Predicted yields assuming sequential ionization	108
V.4. Alignment dependence of recollision events	111
V.4.1. Alignment dependence of electron impact ionization	114
V.4.2. Conclusion	122
V.5. Field Excitation	123
V.6. Conclusion	127
<b>VI. Summary and Conclusion</b>	<b>129</b>
<b>Appendix</b>	<b>132</b>
A. Atomic units [au]	133
B. Integration schemes	135
C. Derivation of Eq. V.4.6	139
D. Derivation of Eq. (V.4.8)	141
E. Derivation of Eq. V.4.11	145
F. A note on special functions	147



# Introduction

The interaction of strong and short infrared (IR) laser pulses with atoms, molecules and solids is an active field of research since the late 1980s and 1990s. At that time, the development of new, broad band laser materials [1], novel mode-locking techniques [2], technological advances allowing dispersion control [3] and the concept of chirped-pulse amplification [4] allowed for the first time the production of (sub)-10 fs pulses and pulses with intensities up to  $1 \times 10^{21}$  W/cm<sup>2</sup> (see Ref. [5] for an excellent review on the early development of these laser systems). The control [6] and shot-to-shot measurement [7] of the carrier-envelope phase(CEP), nowadays allows to routinely generate CEP stable, ultra-strong few-cycle laser pulses in scientific laboratories.

In the context of this work, laser pulses with intensities of around  $1 \times 10^{14}$  W/cm<sup>2</sup> and pulse durations with a full-width at half-maximum of approximately 5 fs at a central wavelength of around 800 nm are considered. Such pulses are sufficiently strong to initiate besides excitation, (multiple) ionization and non-linear electronic response in atomic and molecular systems. Due to their high intensity, such fields require a non-perturbative treatment in theoretical calculations. On the other hand, these pulses are sufficiently weak to allow neglecting the magnetic field and relativistic effects.

Within this laser intensity regime, many new and interesting laser driven processes have been observed, using mainly atoms as targets. Some of the most important strong-field phenomena observed are the above-threshold photoionization (ATI) [8] and the presence of an ATI plateau [9], tunnelling ionization [10], non-sequential double ionization (NSDI) [11], the generation of high-harmonic radiation (HHG) [12] and the possibility to create attosecond pulse trains in the extended ultra-violet (XUV) regime from HHG [13]. Reviews can be found for example in Refs. [14, 15, 5, 16, 17, 18, 19].

From a theoretical point of view, dealing with such strong pulses required the development of new theoretical approaches, since common approximations describing the interaction of light with matter are insufficient: as the average energy of a free electron

in a field, the ponderomotive energy, becomes larger than the photon frequency, perturbative approaches do not converge any more and become invalid [20]. Two milestones in the theoretical understanding of strong-field processes were the development of the Keldysh theory for strong-field ionization [10] and the classical three-step model [21], which gives an intuitive physical motivation for the high energy ATI cut-off, HHG and recollisional ionization and excitation. Nowadays, many analytical models and equations (e.g. [21, 10, 22, 23, 20]) provide the basis to understand strong-field processes, while numerical modelling has become increasingly important in order to describe effects beyond these approximations, such as electron-electron correlation effects, effects of the Coulomb potential, etc.

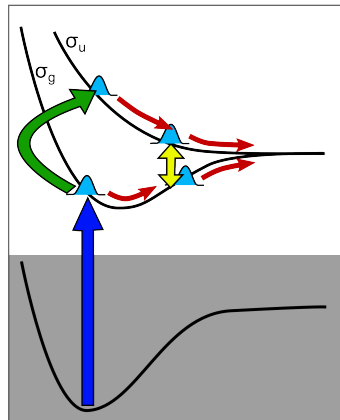
Formerly, mainly the atomic response to strong fields was studied; more recently, the attention has started to turn to more complex targets, such as molecules and nanostructures (e.g. [24, 25]). As opposed to atoms, molecular targets are far more difficult to treat theoretically due to the non-spherically symmetric potential and its multi-center nature as well as the presence of additional vibrational and rotational degrees of freedom. Therefore, effects so far neglected become important: The symmetry of the wavefunction plays a role in ionization [26]; due to the closer energetic spacing, contributions from several lower and higher electronic states become non-negligible; interatomic distances become relevant [27]; high-harmonic yields are influenced by orbital symmetry [28]; multiple orbital contributions play a role [29]; ATI photoelectron spectra are influenced [30], etc. At the same time, strong-field physics and the possibility to align molecules relatively to the laser polarization direction [31] open a new route to investigate molecular properties and molecular dynamics. Prominent examples are the imprint of molecular orbital symmetry on HHG and molecular orbital tomography [32, 33], probing molecular vibrational dynamics [34] and molecular reaction control in small molecules (e.g. [35, 36, 37, 38, 39, 40]).

Molecular reaction control with strong laser pulses is both challenging and exciting due to the fact that the dynamics in molecules take place on several timescales: while the motion of electrons evolves on attosecond to femtosecond timescales, the nuclear motion and thus chemical reactions proceed on much longer, femtosecond timescales. Early, light induced control schemes for molecular reactions therefore utilized weak laser pulses with a duration of hundreds of femtoseconds corresponding to the timescales of the nuclear motion and shaped the envelope, phase and chirp of the pulse to gain control [41, 42]. Few-cycle IR pulses, on the other hand, are slightly shorter than typical molecular vibrations and time shifts introduced by changing the carrier-envelope phase are even

on the timescale of the electronic motion. As a consequence, ultrashort pulses influence the nuclear dynamics mainly via accessing the electronic response prior to vibrational dynamics.

Ultrashort pulses are not only characterized by their envelope function and carrier frequency. The exact field shape of a few-cycle pulse is determined by the relative phase between the envelope function and the carrier wave, by the so called carrier-envelope phase. The carrier-envelope phase (CEP) has an important influence on several strong-field processes for systems ranging from atoms to nanostructures. To give a few examples, the carrier-envelope phase leads to an asymmetry in the ejection of photoelectrons from atoms (e.g. [43]), influences the HHG structure in atoms (e.g. [6, 44]) and the ATI photoelectron-spectrum from nanotips [25].

The CEP is also relevant for molecular processes (e.g. [35, 37, 38, 39, 40]), for which a CEP dependent directional asymmetry of the proton or deuteron ejection from  $\text{H}_2^+$ ,  $\text{D}_2^+$  and DCI was observed. The control scheme has been shown to be based on the coherent superposition of the population of the ionic ground- and excited state. The coherent superposition is thereby created via recollision and field-driven population transfer [36] (see Figure). When the wavepacket reaches bond distances, where the energy spacing between the ground and excited state goes to zero, the field driven electronic dynamics are frozen, leading to a carrier-envelope phase dependent charge localization on one of the nuclei [36].



Charge localization in  $\text{H}_2^+$ . Gray region: neutral; white region: cation; blue arrow: initial ionization step; green arrow: recollisional excitation; yellow arrow: field-driven coupling of the two states.

These experiments clearly show that molecular dynamics can be influenced and efficiently

controlled on a sub-cycle time scale using strong, ultrashort pulses. The reaction outcome itself is, however, not investigated in the above described experiments. A first experiment involving several different dissociation channels was performed by Liu et al. in Ref. [45]. In their experiment, they compared the asymmetry of the  $C^{2+}$  emission from CO for the  $C^{2+}+O$  and the  $C^{2+}+O^+$  channels.

In this work, together with the experimentalists Dr. M. Kitzler and Dr. X. Xie from the Vienna University of Technology, it has been shown for the first time that molecular reaction control using strong, few-cycle pulses is not only achievable, control can even be maintained for molecules significantly larger than diatoms [46, 47]. It is the goal of this work to identify the underlying control mechanisms using theoretical modelling. The challenge thereby lies in the necessity to combine molecular physics with strong-field physics in order to find models suitable to describe the molecule–strong-field interaction process.

Due to the different timescales involved, ranging from attoseconds to several tens of femto-seconds, the investigation of reaction control using strong, few-cycle pulses requires a multi-scale approach. Furthermore, the complexity of the problem, the presence of an inhomogeneous, multi-center potential and the comparatively large number of molecular degrees of freedom necessitate a multi-physics approach and the employment of several different methods from different fields, including quantum chemistry, quantum dynamical and semi-classical modelling, and scattering theory. Moreover, due to the complexity of the problem, simplifications have to be introduced to describe the physics relevant to the interaction of the molecules with intense few-cycle laser pulses.

The present work provides an interpretation of several recent experimental results, allows the identification of the underlying physical mechanisms and provides physical pictures enhancing our intuitive understanding of these new processes.

Still, many exciting questions in the topic of strong-field interaction with molecules remain open or have not been touched upon yet. It can therefore be expected that this field of research will continue to attract considerable attention in the scientific community.

# Part I.

## Theory

“It doesn’t matter how beautiful your theory is, it doesn’t matter how smart you are. If it doesn’t agree with experiment, it’s wrong.”

---

*(Richard Feynman)*

In this chapter, a brief introduction to the interaction of strong and short laser pulses with atoms and molecules and a brief introduction to molecular dynamics and electronic structure methods will be given. Throughout this chapter and in the entire work, atomic units will be used, in which the electronic charge  $e$ , the electronic mass  $m_e$  and the reduced Planck’s constant  $\hbar$  are set to one. A summary and conversion table for the atomic unit system is given in appendix A.

### I.1. Ultra-short pulses and the carrier-envelope phase

Advances in modern technology of designing ultra-broadband laser amplifiers and dispersion management allow today the routine generation of high intensity laser pulses with pulse durations down to a few optical cycles. (See Ref. [5] for a review.). At infrared wavelengths with  $\lambda \approx 800$  nm, full-width at half maximum pulse durations of less than 5 fs can be obtained. Much of the work presented in this thesis will focus on the interaction of these extremely short pulses with molecules.

The short duration of the total pulse compared to the optical cycle implies that the pulse envelope changes appreciably during one laser cycle. Therefore, the peak intensity and the exact form of the field will depend on the relative phase,  $\phi_{CE}$ , of the carrier wave to the envelope (compare dark and light blue line in Fig. I.1.1). This carrier-envelope

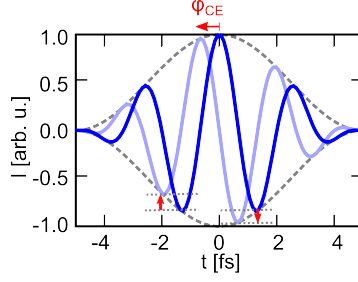


Figure I.1.1.: Change of pulse shape with changing carrier-envelope phase. Dark blue: symmetric pulse ( $\phi_{CE} = 0^\circ$ ), light blue: anti-symmetric pulse ( $\phi_{CE} = -90^\circ$ ).

phase shift (CEP) can nowadays be efficiently controlled in experimental laser setups [6] and measured on a shot-to-shot basis [7].

The vector potential  $\mathbf{A}(\mathbf{r}, t)$  of a few cycle field is thus fully defined by

$$\mathbf{A}(\mathbf{r}, t) = \mathbf{A}_0 f(t) \cdot \cos(\mathbf{k}\mathbf{r} + \omega t + \phi_{CE}), \quad (\text{I.1.1})$$

where  $t$  is time,  $\mathbf{A}_0$  the maximum of the vector potential,  $f(t)$  a smoothly varying envelope function,  $\omega$  the carrier frequency and  $\phi_{CE}$  the carrier envelope phase. The k-vector  $\mathbf{k} = \frac{2\pi}{\lambda} \hat{\mathbf{e}}$  is defined through the wavelength  $\lambda = \frac{2\pi c}{\omega}$  and the propagation direction  $\hat{\mathbf{e}}$ . Since the envelope function,  $f(t)$  is zero for  $t \rightarrow -\infty$  and  $t \rightarrow \infty$ , this definition ensures that the vector potential vanishes before and after the pulse. Within the Coulomb gauge, the electric field is given by

$$E(t) = -\frac{1}{c} \frac{\partial}{\partial t} \mathbf{A}(\mathbf{r}, t) = \mathbf{E}_0 \left[ \frac{1}{\omega} f'(t) \cdot \cos(\mathbf{k}\mathbf{r} + \omega t + \phi_{CE}) - f(t) \cdot \sin(\mathbf{k}\mathbf{r} + \omega t + \phi_{CE}) \right], \quad (\text{I.1.2})$$

where  $c$  the speed of light and  $\mathbf{E}_0 = \frac{\mathbf{A}_0 \omega}{c}$ . For long pulses, the first term in the square brackets is approximately zero and can be dropped.

Since the carrier-envelope phase-shift corresponds to effective time shifts on the sub-wavecycle scale, few-cycle pulses with controlled CEP allow addressing dynamics on a sub-cycle time scale. It has been shown that the carrier-envelope phase can indeed have a substantial influence on the laser-driven dynamics of atoms and small molecules [35, 48, 37, 38, 39, 40, 45, 49, 50].



## I.2. Strong-field molecule interaction

“A new laser material [...], and a new amplification technique [...], made high-power lasers accessible to many university laboratories. This research has become one of the most exciting fields of research in atomic, molecular and optical physics.”

---

(Anne L’Huillier; *Europhysics News*, 33, 2002)

### I.2.1. Strong-field physics

The most fundamental way to treat laser-matter interaction is to solve the Schrödinger equation in the presence of an electromagnetic field. At low intensities, perturbative approaches allow both, a large degree of physical understanding of the underlying field driven processes as well as their quantitative description. However, as the intensity of the laser field increases and as the ponderomotive potential, i.e. the cycle averaged energy of a free electron in the electromagnetic field, increases and becomes much larger than the energy of a single photon, perturbation theory breaks down [14]. The ponderomotive energy,  $U_P$ , that can easily be derived from the motion of a classical electron in a cw field

$$U_P = \frac{1}{2} \frac{(p_{\max})^2}{2} = \frac{1}{2} \frac{A^2}{2c^2} = \frac{E^2}{4\omega^2} \quad (\text{I.2.1})$$

thus provides an important strong-field parameter.

### I.2.2. Strong-field ionization

In the strong-field regime, ionization can usually not be understood in terms of single or few photon absorption. While resonances may enhance ionization [51, 52], efficient ionization by ultrastrong fields is also possible when the ionization potential is well above the photon energy and when no resonances are present. A fundamental understanding

## I.2. Strong-field molecule interaction

of the strong field ionization process was first acquired by Keldysh [10]. Keldysh distinguished two strong field ionization regimes: the multi-photon regime and the tunnelling regime. The tunnelling regime is thereby characterized by  $\gamma \ll 1$  and the multi-photon regime by  $\gamma \gg 1$ , where the Keldysh parameter  $\gamma$  is given by

$$\gamma = \sqrt{\frac{I_P}{2U_P}} = \frac{\omega\sqrt{2I_P}}{E}, \quad (\text{I.2.2})$$

and  $I_P$  is the ionization potential of the system.

The physical idea behind multi-photon ionization is that the electron is propelled to the continuum by the simultaneous absorption of several photon as shown in Fig. I.2.1.a). In this case, the ionization rate,  $\Gamma$ , can be expected to depend on the field strength,  $E$ , according to a power law [53]

$$\Gamma_{\text{MPI}} \propto E^{2K}, \quad (\text{I.2.3})$$

where  $K$  is the number of photons absorbed.

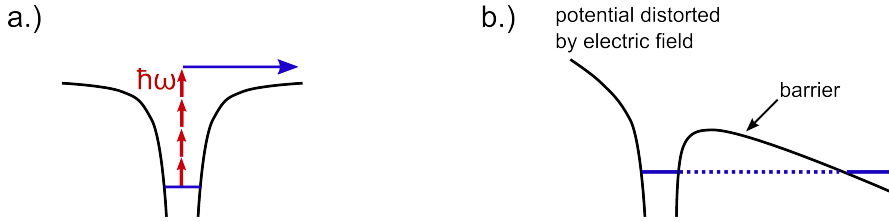


Figure I.2.1.: Physical picture of a.) multi-photon ionization and b.) tunneling ionization.

Tunnelling ionization describes the limiting case when the electric field oscillates sufficiently slowly that the electron can tunnel to the continuum through the barrier formed by the combined atomic(molecular) and electric field as shown in Fig. I.2.1.b.) [54]. A first approximation for the tunnelling rate can be obtained considering a narrow square well potential in a static field and using the WKB-approximation [55]. This yields an exponential dependence of the ionization rate,  $\Gamma$ , on the electric field,  $E$ .

$$\Gamma_{\text{TU}} = e^{-\frac{2}{3} \frac{\sqrt{2I_P}^3}{E}}. \quad (\text{I.2.4})$$

After Keldysh had discovered the tunnelling mechanism in the 1860's, several refinements to his model were suggested, taking into account, for example, the shape of the (atomic) wavefunction, the time dependence of the field, Coulomb corrections, the suppression of

the barrier or the molecular structure (e.g. [56, 57, 26, 58, 59]). A review can be found in Ref. [60]. Early improvements to the Keldysh theory are due to Perelomov et al. [23]. Later, a different approach involving infinite sums over the number of photons absorbed was developed by Faisal and Reiss, which is generally referred to as KFR (Keldysh, Faisal and Reiss [10, 61, 20]) method. A widely used expression due to Ammosov, Delone and Krařnov, usually referred to as ADK-Rate, is only valid in the quasistatic regime. The following expression, which was used in the course of this work, and which includes the dependence on the initial momentum of the electron after tunnelling is due to Delone and Krařnov [59].

$$\Gamma_{\text{ADK}} \propto e^{-\frac{2}{3} \frac{\sqrt{2I_P^3}}{E} - \frac{p_{\perp}^2 \sqrt{2I_P}}{E} - \frac{p_{\parallel}^2 \omega^2 \sqrt{2I_P^3}}{3E^3}}, \quad (\text{I.2.5})$$

where all pre-exponential factors have been ignored, and  $p_{\parallel}$  and  $p_{\perp}$  denote the electronic initial momentum after tunnelling parallel and orthogonal to the electric field. This equation will be referred to as ADK-like ionization rate in the following.

### 1.2.3. Strong-field approximation (SFA)

Once the electron is propelled to the continuum by a strong field, it is often a reasonably good approximation to neglect the interaction of the electron with the residual ion in comparison with the (strong) interaction with the field. Within this approximation, the continuum wavefunctions are Volkov states, which are solution to the Schrödinger equation of a free electron in an electric field [62]

$$\phi_{\mathbf{k}}(\mathbf{r}, t)_{\text{length gauge}} = \frac{1}{\sqrt{2\pi}^3} e^{i(\mathbf{k}-\mathbf{A})\mathbf{r} - \int_0^t \frac{1}{2}(\mathbf{k}-\mathbf{A}(t'))^2 dt'}, \quad (\text{I.2.6})$$

where  $\mathbf{A}(t)$  is the vector-potential.

In the classical formulation, the SFA implies that the momentum of an electron released to the continuum at  $t = t_0$  is given by

$$\mathbf{p}^{\text{SFA}}(t) = \mathbf{p}_0 - \int_{t_0}^t \mathbf{E}(t') dt' = \mathbf{p}_0 + \frac{1}{c}(\mathbf{A}(t) - \mathbf{A}(t_0)), \quad (\text{I.2.7})$$

where  $t_0$  is the moment of ionization and  $\mathbf{p}_0$  is the initial momentum. The Coulomb force is neglected in the equation of motion. After the end of the pulse, the final momentum

of a classical electron starting with zero velocity is thus

$$\mathbf{p}_f^{\text{SFA}} = -\frac{1}{c}\mathbf{A}(t_0). \quad (\text{I.2.8})$$

While the strong-field approximation often provides useful insight into physical problems, its application is problematic since it is not gauge invariant. Furthermore, although several important strong-field effects in which an interaction with the residual ion plays a role are captured by the three-step model, due to the neglect of the Coulomb field in the SFA, some physically relevant effects cannot be described (e.g. [63, 64, 65]).

### I.2.4. The three step model

The three-step model by Corkum [21] is a semi-classical model that allows the interpretation of several strong-field processes, including high-energy above-threshold ionization (ATI), high-harmonic generation and nonsequential ionization. The semi-classical model describes these processes in three steps:

1. An electron is released to the continuum by tunnelling ionization at time  $t_1$ . The tunnelling probability as a function of  $t_1$  is given by an ADK-like ionization rate.
2. The electron is propagated in the laser field using the strong-field approximation

$$\mathbf{x}(t; t_1) = \mathbf{x}_0 + \mathbf{v}_0(t - t_1) - \frac{1}{c}\mathbf{A}(t_1)(t - t_1) + \frac{1}{c}\int_{t_1}^t \mathbf{A}(t')dt'. \quad (\text{I.2.9})$$

3. In linear polarized light, depending on the moment of ionization, the electron may return to the origin,  $\mathbf{x}(t_2; t_1) = 0$ , where it recollides with the nucleus. The maximum possible recollision energy can be determined numerically and is given by [21]

$$\varepsilon_{\text{rec.}}^{\text{max}} = 3.17U_P. \quad (\text{I.2.10})$$

At 800 nm and  $1 \times 10^{14} \text{ W/cm}^2$ , this corresponds to approximately 20 eV.

Upon recollision, the electron may recombine with the ion or scatter elastically or inelastically. Depending on the type of interaction, this may lead to high-harmonic generation, high-energy ATI and recollisional excitation and ionization:

- **Recombination.** If the electron recombines with the ion, the excess energy given by  $\varepsilon_{\text{rec}} + I_P$ , where  $I_P$  is the ionization potential, can be released by emitting a photon. This is the origin of high-harmonic generation. A more detailed, quantum-mechanical treatment of this process is given by the Lewenstein model [22].
- **Elastic scattering.** While direct (i.e. not rescattered) photoelectrons can have a maximum energy of  $2U_P$  after the end of the laser pulse, rescattered photoelectrons can have an energy up to approximately  $10U_P$ . This can be explained by the fact that, upon recollision, the electrons can be reflected by a hard collision with the ion:  $\mathbf{p}(t_2) \rightarrow -\mathbf{p}(t_2)$ , leading to a final momentum after the end of the pulse of

$$\mathbf{p}_f = -(\mathbf{A}(t_2) - \mathbf{A}(t_1)) - \mathbf{A}(t_2), \quad (\text{I.2.11})$$

where the first term in brackets corresponds to the momentum the electron has upon recollision, and the second term corresponds to the momentum the electron gains thereafter due to the acceleration in the field. The times  $t_2$  and  $t_1$  are related by the recollision condition  $\mathbf{x}(t_2; t_1) = 0$ . This explains qualitatively the spectrum of the above threshold ionization photoelectrons, which exhibits a cutoff at  $10U_P$ .

- **Inelastic scattering.** Inelastic scattering can lead to the excitation of the residual ion and, possibly, subsequent field ionization (RESI - recollision-excitation with subsequent ionization). If the recollision energy is sufficiently high, the recolliding electron can even induce ionization via electron impact ionization (RI - recollisional ionization).

### 1.2.5. Laser-matter interactions in the Schrödinger equation

While the above described physical pictures allow a basic analysis of several strong-field processes, an exact treatment of laser-matter interactions can only be achieved by solving the many-body Schrödinger equation in the presence of an electromagnetic field<sup>1</sup>. The non-relativistic, quantum-mechanical treatment of laser-matter interactions

<sup>1</sup>It is noted parenthetically that the solution of the full Schrödinger equation is only feasible for very small systems such as the hydrogen atom,  $\text{H}_2^+$  or He. For larger system, approximations to the exact expression have to be made in order to allow solving the equation analytically or numerically.

would thereby require both, the correct treatment of the quantum nature of electrons and nuclei and the quantization of the radiation field. However, if the number of photons is high enough, a semi-classical description can be used in which the radiation field is treated classically through Maxwell's equations, while the atomic or molecular system is described quantum-mechanically [66].

### The non-relativistic Hamiltonian in velocity gauge representation

Within the Coulomb gauge,  $\nabla \mathbf{A}(\mathbf{r}, t) = 0$ , the non-relativistic Hamiltonian of a charged particle with mass  $m$  and charge  $q$  can be written as [67]

$$H_v = \frac{1}{2m} \left[ \mathbf{p} - \frac{q}{c} \mathbf{A}(\mathbf{r}, t) \right]^2 + qU(\mathbf{r}, t), \quad (\text{I.2.12})$$

where  $\mathbf{p}$  denotes the canonical momentum and the subscript  $v$  stands for “velocity gauge”. The electric field is fully described by the vector potential  $\mathbf{A}$ . The potential  $U$  describes the potential created by a static external charge distribution.

In general, one would have to include the Hamiltonian of the electromagnetic field,  $H_{\text{em}} = \frac{1}{8\pi} \int (\mathbf{E}^2 + \mathbf{B}^2) d^3r$  in the above expression [67]. In the external field approximation, however, the influence of the quantum system on the electromagnetic field is neglected. In this case, the field Hamiltonian can be dropped, as has been done in Eq. (I.2.12).

Relativistic effects, which are neglected in the above expression, will only become important when the energy gained by a classical electron in the field is comparable to  $mc^2$ , i.e. when  $I \approx 2c^4\omega^2$ , corresponding to  $I \approx 8 \times 10^{18} \text{ W/cm}^2$  for 800 nm radiation (see Eq. (I.2.1)), which is several orders of magnitudes above the intensities considered in this work.

### Dipole Approximation

If the system size  $\lambda_c$  is much smaller than the wavelength  $\lambda$  of the electromagnetic field ( $\lambda_c \ll \lambda$ ) and if the interaction with the magnetic field  $B = \nabla \times \mathbf{A}(\mathbf{r}, t)$  can be neglected, the spacial dependence in the vector potential can be dropped

$$\mathbf{A}(\mathbf{r}, t) \approx \mathbf{A}(t). \quad (\text{I.2.13})$$

At infrared wave lengths with  $\lambda \approx 800$  nm,  $\lambda_c \ll \lambda$  for atoms and small molecules [68]. Neglecting the magnetic field can be expected to be a good approximation as long as the trajectory described by a classical electron in the electromagnetic field is not strongly distorted by the magnetic field. This limit is reached for intensities given by  $I \approx 8c\omega^3$  [69, 70], which corresponds to  $I \approx 7 \times 10^{15}$  W/cm<sup>2</sup> for 800 nm radiation.

### The Hamiltonian in length gauge representation

Within the dipole approximation,

$$\mathbf{E}(\mathbf{r}, t) = \mathbf{E}(\mathbf{k}\mathbf{x} - \omega t) \approx \mathbf{E}(\omega t) = \mathbf{E}(t), \quad (\text{I.2.14})$$

the velocity gauge expression, Eq. (I.2.12), can be transformed to the so-called length gauge via

$$\psi_l = e^{i\frac{q}{c}\mathbf{A}(t)\mathbf{r}}\psi_v. \quad (\text{I.2.15})$$

This leads to the length gauge Hamiltonian [67]

$$H_l = \frac{1}{2m}\mathbf{p}^2 - q\mathbf{r}\mathbf{E}_e(t) + qU_e(\mathbf{r}). \quad (\text{I.2.16})$$

### Hamiltonian of atoms and molecules in electromagnetic fields

Using Eq. (I.2.12), the Hamiltonian of an atom or molecule in an electromagnetic field is given by

$$H_v = \sum_n \frac{1}{2M_n} \left[ \mathbf{p}_n - \frac{Z_n}{c}\mathbf{A}(\mathbf{r}, t) \right]^2 + \sum_i \frac{1}{2} \left[ \mathbf{p}_i + \frac{1}{c}\mathbf{A}(\mathbf{r}, t) \right]^2 + \frac{1}{2} \sum_{i,j} \frac{1}{|\mathbf{r}_i - \mathbf{r}_j|} + \frac{1}{2} \sum_{m,n} \frac{Z_m Z_n}{|\mathbf{R}_m - \mathbf{R}_n|} - \sum_{m,i} \frac{Z_m}{|\mathbf{R}_m - \mathbf{r}_i|}, \quad (\text{I.2.17})$$

where the  $M_n$  denote the nuclear masses,  $\mathbf{R}_n$  the nuclear coordinates,  $Z_n$  the nuclear charges and  $\mathbf{r}_i$  the electronic coordinates. The sums over  $m$  and  $n$  run over all nuclei, those over  $i$  and  $j$  over the electrons. The first two terms of this equation describe the momenta of the nuclei and the electrons. The third and fourth term are the repulsive electron-electron and nucleus-nucleus interaction. The fifth term is the attractive electron-nucleus interaction.

After the transformation to the length gauge, the Hamiltonian is given by

$$H(\mathbf{r}_i, \mathbf{R}_i, t) = H_0 + \left( \sum_i \mathbf{r}_i - \sum_n Z_n \mathbf{R}_n \right) \mathbf{E}(t), \quad (\text{I.2.18})$$

where  $H_0$  denotes the field free Hamiltonian of the atom or molecule. As discussed above, this expression is only valid within the dipole-approximation.



## I.3. Molecular quantum dynamics

Now we come to the heart of chemistry. If we can understand what holds atoms together as molecules we may also start to understand why, under certain conditions, old arrangements change in favour of new ones. We shall understand structure, and through structure, the mechanism of change.

---

(*P. W. Atkins, Molecular Quantum Mechanics, 1983*)

### I.3.1. The field-free, non-relativistic molecular Hamiltonian

The non-relativistic Hamiltonian of a molecule with  $N_n$  nuclei and  $N_e$  electrons is given by the sum of the nuclear and electronic kinetic energy operators,  $T_n$  and  $T_e$  and the nucleus-nucleus, electron-electron and nucleus-electron interactions,  $V_{n,n}$ ,  $V_{e,e}$  and  $V_{n,e}$ :

$$H = \underbrace{\sum_{\alpha}^{N_n} \frac{\mathbf{p}_{\alpha}^2}{2M_{\alpha}}}_{T_n} + \underbrace{\sum_i^{N_e} \frac{\mathbf{p}_i^2}{2}}_{T_e} + \underbrace{\frac{1}{2} \sum_{\alpha}^{N_n} \sum_{\beta \neq \alpha}^{N_n} \frac{Z_{\alpha} Z_{\beta}}{|\mathbf{R}_{\alpha} - \mathbf{R}_{\beta}|}}_{V_{n,n}} + \underbrace{\frac{1}{2} \sum_i^{N_e} \sum_{j \neq i}^{N_e} \frac{1}{|\mathbf{r}_i - \mathbf{r}_j|}}_{V_{e,e}} - \underbrace{\sum_{\alpha}^{N_n} \sum_i^{N_e} \frac{Z_{\alpha}}{|\mathbf{R}_{\alpha} - \mathbf{r}_i|}}_{V_{n,e}}. \quad (\text{I.3.1})$$

The sums over Greek letters run over the nuclei, while sums over Latin letters run over electrons. Equally, the  $\mathbf{R}_{\alpha}$  denote the spatial coordinates the nuclei and the  $\mathbf{r}_i$  the spatial degrees of freedom of the electrons. The nuclear masses are given by  $M_{\alpha}$ . The momentum operator  $\mathbf{p}_{\alpha}$  is given by  $\mathbf{p}(\mathbf{R}_{\alpha}) = -i\nabla_{\mathbf{R}_{\alpha}}$  and  $\mathbf{p}_i$  is given by  $\mathbf{p}(\mathbf{r}_i) = -i\nabla_{\mathbf{r}_i}$ .

The molecular wavefunction  $\Psi$  is a function of all nuclear and electronic degrees of freedom and is defined through the Schrödinger equation

$$H\Psi(\mathbf{R}_1, \dots, \mathbf{R}_{N_n}, \mathbf{r}_1, \dots, \mathbf{r}_{N_e}, t) = -i\frac{\partial}{\partial t}\Psi(\mathbf{R}_1, \dots, \mathbf{R}_{N_n}, \mathbf{r}_1, \dots, \mathbf{r}_{N_e}, t), \quad (\text{I.3.2})$$

where  $H$  is the Hamiltonian. If the Hamiltonian is time independent, as in Eq. (I.3.1),

the equation is separable which leads to

$$H\Psi(\mathbf{R}, \mathbf{r}) = E\Psi(\mathbf{R}, \mathbf{r}), \quad (\text{I.3.3})$$

where  $\Psi(\mathbf{R}, \mathbf{r}, t) = \Psi(\mathbf{R}, \mathbf{r})e^{iEt}$ . (Here and in the following  $\mathbf{R}$  denotes  $\{\mathbf{R}_1, \dots, \mathbf{R}_{N_N}\}$  and  $\mathbf{r}$  denotes  $\{\mathbf{r}_1, \dots, \mathbf{r}_{N_e}\}$ .)

The wave function  $\Psi(\mathbf{R}, \mathbf{r})$ , which depends on  $D = 3 \cdot (N_N + N_e)$  spatial degrees of freedom, can be solved exactly neither analytically nor numerically for most physical systems of interest. Even for the smallest of molecules,  $\text{H}_2$ , simplifications such as the Born-Oppenheimer approximation, discussed in the following, will be necessary to allow the investigation of molecular electronic states and dynamics.

### I.3.2. The Born-Oppenheimer and Born-Huang approximation

The mass ration of electrons to nuclei is  $\frac{M_{\text{nuc}}}{m_{\text{elec}}} \gtrsim 1836$ . The electrons thus move much faster than the nuclei. One can therefore, at every moment in time, view the electrons in a molecule to move in the quasi-static potential of the slow nuclei. This picture motivates the (formally exact) expansion of the total wavefunction  $\Psi$  in a basis of electronic wavefunctions  $\psi$  [71]

$$\Psi(\mathbf{R}, \mathbf{r}) = \sum_{i=0}^{\infty} \psi_i^a(\mathbf{r}; \mathbf{R}) \cdot \chi_i^a(\mathbf{R}), \quad (\text{I.3.4})$$

where the  $\psi$  are eigenfunctions of the electronic Hamiltonian  $H_e$ , which contains all terms of the molecular Hamiltonian which explicitly depend on the electronic coordinates:

$$H_e \psi^a(\mathbf{r}; \mathbf{R}) = [T_e + V_{e,e} + V_{n,e}] \psi^a(\mathbf{r}; \mathbf{R}) = E_{\text{elec}}(\mathbf{R}) \psi^a(\mathbf{r}; \mathbf{R}) \quad (\text{I.3.5})$$

The superscript “a” denotes the “adiabatic representation” as opposed to the diabatic representation, “d” introduced later.

Substituting the ansatz Eq. (I.3.4) into the time-independent Schrödinger equation, Eq. (I.3.3) and using the Hamiltonian from Eq. (I.3.1), multiplication with  $\langle \psi_i |$ , leads

to the following infinite set of coupled equations:

$$\begin{aligned}
 & \overbrace{(T_n + E_i^{\text{elec}}(\mathbf{R}) + V_{n,n}(\mathbf{R}))}^{U_i^{\text{a}}} \chi_i^{\text{a}}(\mathbf{R}) \\
 & - \sum_{j=0}^{\infty} \left[ \sum_{\alpha} \frac{1}{2M_{\alpha}} \left( 2 \overbrace{\langle \psi_i | \nabla_{\alpha} | \psi_j \rangle}^{\mathbf{T}_{ij}^{(1)}} \cdot \nabla_{\alpha} + \overbrace{\langle \psi_i | \nabla_{\alpha}^2 | \psi_j \rangle}^{T_{ij}^{(2)}} \right) \right] \chi_j^{\text{a}}(\mathbf{R}) \\
 & = E \chi_i^{\text{a}}(\mathbf{R}), \quad (\text{I.3.6})
 \end{aligned}$$

where the integration  $\langle \bullet \rangle$  is performed over all electronic degrees of freedom. The nuclear wavefunctions  $\chi_i^{\text{a}}$  are thus the solutions of Schrödinger-like equations coupled via the non-adiabatic coupling elements, the matrices  $\mathbf{T}_{ij}^{(1)}$ , and the scalar second order couplings,  $T_{ij}^{(2)}$ , which depend on the derivatives of the electronic wavefunctions with respect to the nuclear coordinates.

### Born-Oppenheimer approximation

So far, the ansatz for the wavefunction and the coupled equations are exact. In the adiabatic Born-Oppenheimer approximation and the Born-Huang approximation, however, the sum in Eq. (I.3.4) is truncated: in the adiabatic approximation to one electronic state only ( $N_{\text{st}} = 1$ ) and in the Born-Huang approximation to  $N_{\text{st}}$  states.

Additionally, in the Born-Oppenheimer approximation and often also in the Born-Huang approximation, the first and second order couplings are neglected ( $\mathbf{T}^{(1)} = 0$ ,  $T^{(2)} = 0$ ). Due to their scaling with  $\frac{1}{M_{\alpha}}$ , these couplings can be expected to be small and these terms are usually only large in regions where electronic states are energetically close and the character of the electronic wave function changes rapidly with changing nuclear configuration [71].

In the Born-Oppenheimer approximation, the nuclear Schrödinger reads

$$\underbrace{(T_n + E_{\text{elec}}(\mathbf{R}) + V_{n,n})}_{U(\mathbf{R})} \chi(\mathbf{R}) = E \chi(\mathbf{R}). \quad (\text{I.3.7})$$

The nuclear wavefunction,  $\chi(\mathbf{R})$ , thus evolves on a single effective  $3N_n$ -dimensional potential energy landscape  $U(\mathbf{R})$ . The potential  $U(\mathbf{R}) = E_{\text{elec}}(\mathbf{R}) + V_{n,n}(\mathbf{R})$  is thereby defined via the electronic energy corresponding to the electronic eigenstate  $\psi$  as shown

schematically in Fig. I.3.1. This eigenstate is assumed not to change throughout the dynamical process.

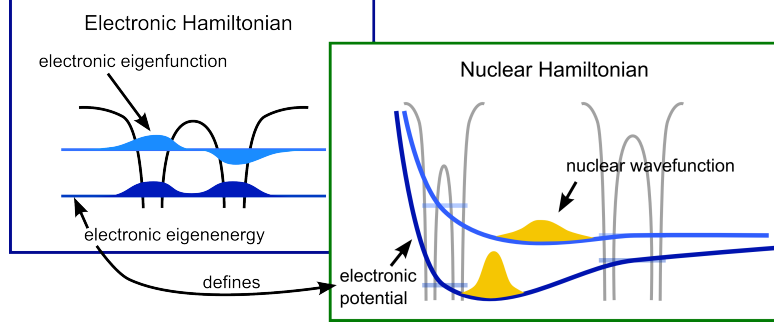


Figure I.3.1.: Schematic of the Born-Oppenheimer (BO) and Born-Huang approximation. In BO, only one electronic potential is taken into account.

### Beyond Born-Oppenheimer

If the non-adiabatic couplings are large, and especially at conical intersections, where the non-adiabatic couplings can have a singularity, the Born-Oppenheimer approximation is not valid. In this case, the Born-Huang ansatz may be used, where the sum in Eq. (I.3.4) is truncated at  $i = N_{\text{st}}$ , including all strongly coupled states. The infinite set of coupled equations then reduces to a set of  $N_{\text{st}}$  equations, coupled via  $\mathbf{T}_{ij}^{(1)}$  and  $T_{ij}^{(2)}$ .

$$\begin{aligned}
 & (T_n + U_i^a)\chi_i(\mathbf{R})^a \\
 & - \sum_{j=1}^{N_{\text{st}}} \underbrace{\left[ \sum_{\alpha} \frac{1}{2M_{\alpha}} \left( 2 \overbrace{\langle \psi_i | \nabla_{\alpha} | \psi_j \rangle}^{\mathbf{T}_{ij}^{(1)}} \cdot \nabla_{\alpha} + \overbrace{\langle \psi_i | \nabla_{\alpha}^2 | \psi_j \rangle}^{T_{ij}^{(2)}} \right) \right]}_{\hat{N}_{ij}} \chi_j(\mathbf{R})^a \\
 & = E\chi_i(\mathbf{R})^a, \quad (\text{I.3.8})
 \end{aligned}$$

with  $i \in [1, N_{\text{st}}]$ .

In time-dependent problems, in which  $\chi_i(\mathbf{R})$  is replaced by  $\chi_i(\mathbf{R}, t)$  and  $E$  by  $-i\frac{\partial}{\partial t}$ , this means that during the time evolution, parts of the nuclear wavepacket can switch the electronic state. The switching probability thereby depends on the size of the non-adiabatic coupling terms,  $\mathbf{T}_{ij}^{(1)}$  and  $T_{ij}^{(2)}$ .

## Diabatic representation

The coupled equations can either be solved directly, or, alternatively, can be transformed to the diabatic representation. In the diabatic representation, the wavefunction is defined as [72]

$$\Psi(\mathbf{R}, \mathbf{r}) = \sum_{i=0}^{\infty} \psi_i^{\text{d}}(\mathbf{r}; \mathbf{R}) \cdot \chi_i^{\text{d}}(\mathbf{R}), \quad (\text{I.3.9})$$

where the  $\psi_i^{\text{d}}$  are no longer eigenfunctions of the electronic Schrödinger equation, but are related to the  $\psi_i^{\text{a}}$  via the unitary transform  $A$

$$\psi_i^{\text{a}}(\mathbf{r}; \mathbf{R}) = \sum_{j=1}^{N_{\text{st}}} A_{ij}^{\dagger}(\mathbf{R}) \psi_j^{\text{d}}(\mathbf{r}; \mathbf{R}). \quad (\text{I.3.10})$$

The goal is to define the unitary transform,  $A_{ij}(\mathbf{R})$ , such that the new functions  $\psi_i^{\text{d}}$  have vanishing derivative couplings. This leads to the requirement [72]

$$\nabla_{\alpha} A_{ij}(\mathbf{R}) + \sum_{k=1}^{N_{\text{st}}} \mathbf{T}_{ik}^{(1)\text{a}} A_{kj}(\mathbf{R}) = 0. \quad (\text{I.3.11})$$

If a diabatic representation can be found, this leads to

$$\left( T_n + \sum_{j=1}^{N_{\text{st}}} \sum_{k,l}^{N_{\text{st}}} \overbrace{A_{ij}^{\dagger} U_{jk}^{\text{a}} A_{kl}}^{U_{il}^{\text{d}}} \right) \chi_l^{\text{d}}(\mathbf{R}) = E \chi_i^{\text{d}}(\mathbf{R}). \quad (\text{I.3.12})$$

This expression has the advantage that it does not depend on any derivative terms. The cost is a full, i.e. non-diagonal, matrix expression for the potential  $U_{il}^{\text{d}}$ , compared to a diagonal matrix  $U_{jk}^{\text{a}} = \sum_{j=1}^{N_{\text{st}}} U_j^{\text{a}} \delta_{jk}$  in the adiabatic case.

### 1.3.3. Field excitations in Born-Huang approximation

With the approximations discussed in section I.2.5, the Hamiltonian of a molecule in an electric field is given by (see Eq. (I.2.18))

$$H = T_n + T_e + V_{n,n} + V_{e,e} + V_{n,e} + \left( \sum_i \mathbf{r}_i - \sum_n Z_n \mathbf{R}_n \right) \mathbf{E}(t), \quad (\text{I.3.13})$$

where the abbreviations defined in Eq. (I.3.1) have been used, the sum over  $i$  runs over all electrons with coordinates  $\mathbf{r}_i$  and  $n$  runs over all nuclei with charge  $Z_n$  and coordinates  $\mathbf{R}_n$ . The external, time-dependent electric field is given by  $E(t)$ .

Inserting the time-dependent Born-Huang ansatz

$$\Psi(\mathbf{R}, \mathbf{r}, t) = \sum_{i=0}^{N_{\text{st}}} \psi_i^a(\mathbf{r}; \mathbf{R}) \cdot \chi_i^a(\mathbf{R}, t) \quad (\text{I.3.14})$$

and Eq. (I.3.13) into the time-dependent Schrödinger equation, leads to the following set of equations coupled via the non-adiabatic couplings,  $\hat{N}_{ij}$ , and the dipole couplings,  $\mathbf{d}_{ij}(\mathbf{R})$ :

$$\begin{aligned} & \left( T_n + E_i^{\text{elec}}(\mathbf{R}) + V_{n,n}(\mathbf{R}) \right) \chi_i(\mathbf{R}, t) \\ & - \sum_{j=1}^{N_{\text{st}}} \left( \hat{N}_{ij} + \underbrace{\left\langle \psi_i(\mathbf{r}; \mathbf{R}) \left| \sum_a \mathbf{r}_a - \sum_n Z_n \mathbf{R}_n \right| \psi_j(\mathbf{r}; \mathbf{R}) \right\rangle}_{\mathbf{d}_{ij}(\mathbf{R})} \mathbf{E}(t) \right) \chi_j(\mathbf{R}, t) \\ & = -i \frac{\partial}{\partial t} \chi_i(\mathbf{R}, t), \quad (\text{I.3.15}) \end{aligned}$$

where the indices  $i$  and  $j$  count electronic states, the index  $a$  runs over the electrons and  $n$  over the nuclei with charge  $Z_n$ .

Neglecting the nonadiabatic couplings, Eq. (I.3.15) can thus be written in a matrix notation as

$$\begin{aligned} & \left[ \begin{pmatrix} T_N & & 0 \\ & \ddots & \\ 0 & & T_N \end{pmatrix} + \right. \\ & \left. \begin{pmatrix} U_1 + \mathbf{d}_{1,1}\mathbf{E}(t) & \mathbf{d}_{1,2}\mathbf{E}(t) & \dots & \mathbf{d}_{1,N_{\text{st}}}\mathbf{E}(t) \\ \mathbf{d}_{2,1}\mathbf{E}(t) & \ddots & \ddots & \vdots \\ \vdots & \ddots & \ddots & \mathbf{d}_{N_{\text{st}}-1,N_{\text{st}}}\mathbf{E}(t) \\ \mathbf{d}_{N_{\text{st}},1}\mathbf{E}(t) & \dots & \mathbf{d}_{N_{\text{st}},N_{\text{st}}-1}\mathbf{E}(t) & U_{N_{\text{st}}} + \mathbf{d}_{N_{\text{st}},N_{\text{st}}}\mathbf{E}(t) \end{pmatrix} \right] \begin{pmatrix} \chi_1 \\ \vdots \\ \chi_{N_{\text{st}}} \end{pmatrix} \\ & = -i \frac{\partial}{\partial t} \begin{pmatrix} \chi_1 \\ \vdots \\ \chi_{N_{\text{st}}} \end{pmatrix}, \quad (\text{I.3.16}) \end{aligned}$$

where  $U_i = E_i^{\text{elec}} + V_{n,n}$ . Restricting the basis to  $N_{\text{st}}$  electronic states is equivalent to neglecting any dipole couplings to electronic states not included in the basis.





## I.4. Electronic structure Methods

Nuclear dynamics simulations and methods based on the knowledge of the electronic wavefunction require the solution of the  $N_e$ -particle electronic Schrödinger equation, Eq. (I.3.5):

$$H_e(\mathbf{r}; \mathbf{R})\psi(\mathbf{x}; \mathbf{R}) = [T_e + V_{e,e} + V_{N,e} + V_{N,N}]\psi(\mathbf{x}; \mathbf{R}) = U(\mathbf{R})\psi(\mathbf{x}; \mathbf{R}), \quad (\text{I.4.1})$$

where  $\mathbf{x} = (\mathbf{r}, \sigma)$  denotes both, spacial and spin coordinates. (For convenience, the parametric dependence on  $\mathbf{R}$  will be dropped in the following.)

For systems with several electrons, this equation can be solved exactly neither analytically nor numerically. In the following, several different approximate methods will be discussed. The idea behind most approximate ansätze is thereby to express the  $N_e$ -electron wavefunction in a basis of several effective single-electron wavefunctions, while fulfilling the Pauli principle, i.e. while being antisymmetric with respect to the exchange of any two of the  $N_e$  electrons present in the molecular system.

### I.4.1. Hartree-Fock method

The conceptionally simplest method is the Hartree-Fock method. In the Hartree-Fock approximation, it is assumed that the electronic wavefunction can be written as an antisymmetrized product state of single particle functions, i.e. as a single Slater determinant or configuration,  $\Phi(\mathbf{x})$ , of spin orbitals,  $\phi_i(\mathbf{x}_i)$  [73, 74]

$$\psi(\mathbf{x}) = \Phi(\mathbf{x}) = \hat{A}[\phi_1(\mathbf{x}_1)\phi_2(\mathbf{x}_2)\dots\phi_{N_e}(\mathbf{x}_{N_e})] \quad (\text{I.4.2})$$

$$= \frac{1}{\sqrt{N_e!}} \begin{vmatrix} \phi_1(\mathbf{x}_1) & \dots & \phi_{N_e}(\mathbf{x}_1) \\ \vdots & \ddots & \vdots \\ \phi_1(\mathbf{x}_{N_e}) & \dots & \phi_{N_e}(\mathbf{x}_{N_e}) \end{vmatrix}, \quad (\text{I.4.3})$$

where the operator  $\hat{A}$  denotes the antisymmetrization operator and  $|\bullet|$  denotes the determinant.

The Hartree-Fock wavefunction minimizes the energy  $U(\mathbf{R})$ .

$$U = \frac{\langle \psi | H_e | \psi \rangle}{\langle \psi | \psi \rangle} \rightarrow \min. \quad (\text{I.4.4})$$

under the side condition  $\langle \phi_i | \phi_j \rangle = \delta_{i,j}$  for any  $i, j \in [1, N_e]$ . After minimization and a unitary transform of the single particle wavefunctions  $\phi$ , this variational ansatz leads to a set of pseudo single particle equations, the Hartree-Fock equations [73]

$$F_i |\phi_i\rangle = \underbrace{(T_i + V_{n,i}) |\phi_i\rangle}_{h_i |\phi_i\rangle} + \sum_{j=1}^{N_e} \underbrace{\langle \phi_j | g_{12} | \phi_j \rangle |\phi_i\rangle}_{J_j |\phi_i\rangle} - \sum_{j=1}^{N_e} \underbrace{\langle \phi_j | g_{12} | \phi_i \rangle |\phi_j\rangle}_{K_j \phi_i} = \varepsilon_i |\phi_i\rangle,$$

where  $F_i$  denotes the Fock operator,  $T_i$  the single particle kinetic energy operator and  $V_{n,i}$  the interaction of electron  $i$  with the nuclei. The integration implied by the bracket notation runs over the spatial and spin coordinates of electron 2. The operator  $g_{12}$  is given in real space representation as  $g_{12}(\mathbf{r}_1, \mathbf{r}_2) = \frac{1}{|\mathbf{r}_1 - \mathbf{r}_2|}$ .

The pseudo single particle wavefunctions  $\phi_i$  are thus defined through a Schrödinger-like equation consisting of the sum of a single particle Hamiltonian,  $h_i$ , the Coulomb operator,  $J_i$ , and the exchange operator,  $K_i$ . The single particle wavefunctions  $\phi_i(\mathbf{x}_i)$  can be interpreted as molecular spin-orbitals and the Lagrange multipliers  $\varepsilon_i$  as orbital energies. Since the Fock operator,  $F_i$ , which defines the single particle wavefunction  $\phi_i$ , depends on all other single particle wavefunctions  $\phi_j$ , these equations have to be solved self-consistently in an iterative way. This is generally done numerically using an atom centred basis of Slater type or Gaussian shaped functions  $\varphi_\alpha$ ,  $\phi_i = \sum_\alpha c_{i;\alpha} \varphi_\alpha$  and varying the coefficients  $c_{i;\alpha}$ . Special basis sets have been designed for different atoms which ensure faster convergence than grid based approaches.

The total electronic energy in Hartree-Fock approximation is given by [73]

$$U = \sum_{i=1}^{N_e} \langle \phi_i | h_i | \phi_i \rangle + \frac{1}{2} \sum_{i=1}^{N_e} \sum_{j=1}^{N_e} (\langle \phi_j | J_i | \phi_j \rangle - \langle \phi_j | K_i | \phi_j \rangle) + V_{N,N}. \quad (\text{I.4.5})$$

## 1.4.2. Electron correlation methods

In many cases, the HF method is insufficient to describe the molecular electronic structure and electronic energies adequately and thus often only provides a starting point for other more advanced methods. This is due to the fact that in Hartree-Fock, only the Fermi correlation is considered, i.e. the correlation due to the Pauli principle which prevents same-spin electrons from being at the same point in space. The Coulomb correlation is not accounted for in Hartree-Fock, where every electron moves in the averaged potential of the other electrons.

Including several, instead of one single determinant in the ansatz for the  $N_e$  particle wavefunction can lead to the incorporation of Coulomb correlation effects. Including infinity many determinants in the ansatz, would allow the exact representation of the wavefunction. The following ansatz can thus provide an improvement over the Hartree-Fock method [73]:

$$\psi(\mathbf{x}) = \sum_{i=1}^{N_{\text{det}}} c_i \Phi_i(\mathbf{x}) = \sum_{i=1}^{N_{\text{CSF}}} c_i^{\text{CSF}} \Phi_i^{\text{SCF}}(\mathbf{x}), \quad (\text{I.4.6})$$

where the  $\Phi_i$  denote different Slater determinants, corresponding to excitations. The configuration state functions,  $\Phi_i^{\text{CSF}}(\mathbf{x})$ , are linear combinations of  $\Phi_i$  and are eigenfunctions of the spin  $S^2$  operator. While the description via Slater determinants and configuration state functions is physically equivalent (if the same excitations are included in the ansatz), the use of configuration state functions is numerically favourable since the electronic eigenfunctions  $\psi(\mathbf{x})$  are eigenfunctions of the spin operator, if spin-orbit coupling can be neglected. In this case, only  $\Phi_i^{\text{CSF}}$  corresponding to the required spin quantum number have to be included in the ansatz, which reduces the number of variational parameters  $c_i$  in the wavefunction.

The total number of possible configurations depends exponentially on the system size and it remains a difficult question to decide which configurations to include in the ansatz. One very popular choice is known as complete active space self consistent field (CASSCF) calculation.

### 1.4.2.1. Complete active space calculations (CAS)

In complete active space self consistent field (CASSCF) calculations, the complete space of molecular orbitals (resulting for example from a Hartree-Fock calculation or from a

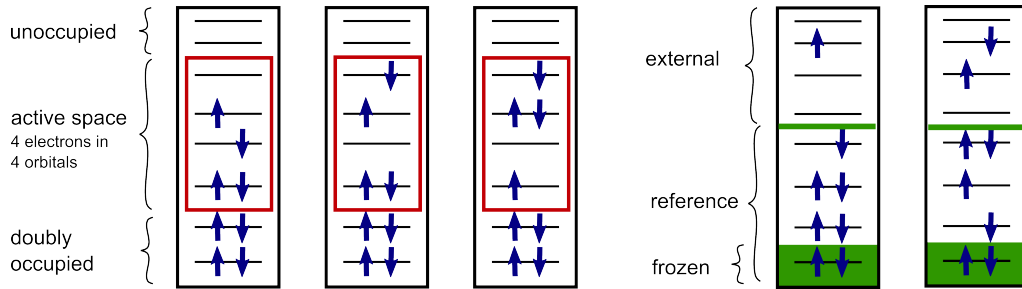


Figure I.4.1.: Examples for determinants included in the multi-configuration ansatz in a.) CAS and b.) CI-SD calculations. Arrows up denote spin-up electrons, arrows down spin-down electrons.

previous run at a similar geometry) is split into three regions [73]. A  $\text{CAS}(N_e^{\text{act}}, N_{\text{orb}}^{\text{act}})$  includes

- $N_{\text{orb}}^{\text{occ}}$  orbitals that are doubly occupied in all CSFs,
- $N_{\text{orb}}^{\text{act}}$  active orbitals that are occupied in total by  $N_e^{\text{act}} = N_e - 2N_{\text{orb}}^{\text{occ}}$  electrons as shown schematically in Figure I.4.1.a) and
- all other orbitals that are unoccupied in all CSFs.

In a CASSCF calculation, both the weights of the CSFs,  $c_i^{\text{CSF}}$ , and the molecular orbitals  $\phi_i(\mathbf{r}_i)$  (or, more specifically, the coefficients  $c_{i,\alpha}$ ) are optimized to minimize the electronic ground state energy of the molecular system. In a state averaged CAS (SA-CAS) calculation, not only the electronic ground state energy is optimized, but the minimization targets all states in the state average. This can be of interest, if a good description of excited states is needed.

Overall, CASSCF calculation allow including what is usually termed static correlation in quantum chemistry, but it completely misses the dynamic correlation, which refers to the influence of many, highly excited determinants, and which is crucial in order to obtain correct energies. Dynamic correlation can be recovered by MRCI calculations or by using perturbative methods.

#### I.4.2.2. Configuration interaction singles-doubles (CI-SD)

In CI-SD calculations, all those determinants are taken into account that correspond to single or double excitations from the single-determinant ground-state configuration. To

reduce the number of determinants, sometimes “frozen” orbitals are defined from which excitations are not allowed (see Fig. I.4.1.b).

In CI-SD calculations typically a much larger number of CSF and thus CSF-weights  $c_i^{\text{CSF}}$  is taken into account compared to CASSCF calculations. However, unlike CASSCF calculations, in CI-SD calculations only the weights  $c_i^{\text{CSF}}$  are optimized, while the molecular wavefunctions are kept fixed. Furthermore, CI-SD suffers from a size consistency problem, i.e. twice the energy of system  $A$  calculated by CI-SD does not equal to the energy of a system  $B$  consisting of two times system  $A$  at large distances. In total, the larger the system, the less correlation energy is recovered by the CI-SD ansatz.

In multi-reference configuration interaction methods (MRCI-SD) a preselected set of configurations is considered as reference configurations from which single and double excitations are allowed. This greatly increases the number of CSF, but allows a better description of excited states.

### I.4.2.3. Perturbative methods

An alternative method to include dynamic correlation effects is the use of perturbative methods. The underlying idea is to partition the electronic Hamiltonian,  $H_e$ , into a reference Hamiltonian,  $H_0$ , and a small perturbation,  $\lambda H'$ , where  $\lambda$  is a scalar scaling the strength of the perturbation:

$$H_e = H_0 + \lambda H'. \quad (\text{I.4.7})$$

The energy,  $U_a$ , of state  $a$  and the corresponding wavefunction  $|a\rangle$  are expanded as

$$U_a = U_{a0} + \lambda U_{a1} + \lambda^2 U_{a2} + \dots \quad \text{and} \quad (\text{I.4.8})$$

$$|a\rangle = |a_0\rangle + \lambda |a_1\rangle + \lambda^2 |a_2\rangle + \dots, \quad (\text{I.4.9})$$

with

$$U_0 = \langle a_0 | H_0 | a_0 \rangle \quad (\text{I.4.10})$$

$$U_1 = \langle a_0 | H' | a_0 \rangle \quad (\text{I.4.11})$$

$$U_2 = \sum_{a \neq b} \frac{\langle a_0 | H' | b_0 \rangle}{U_{a0} - U_{b0}}. \quad (\text{I.4.12})$$

In Möller-Plesset perturbation theory [75], the reference wave function,  $|a_0\rangle$ , is the Hartree-Fock wavefunction and  $H_0$  is typically set to

$$H_0 = \sum_{i=1}^N F_i, \quad (\text{I.4.13})$$

where  $F_i$  is the Fock operator of the  $i$ -th orbital and the sum runs over all occupied orbitals. In this case, the first order energy  $U_0 + U_1$  is equal to the Hartree-Fock energy and the second order correction,  $U_2$  will gradually improve the Hartree-Fock result. Higher order corrections are usually not taken into account. Möller-Plesset perturbation theory usually gives good results for ground state calculations.

In CASPT2, the reference wave function is a CAS wavefunction and the partitioning of the Hamiltonian becomes more complicated. The precise form can be found in Ref. [76, 77] and will not be given in detail here.

### I.4.3. Density functional theory (DFT) and time-dependent DFT (TDDFT)

Density functional theory is a formally exact method to calculate the ground state energy of a system and is computationally more efficient than the high level *ab initio* methods (CAS, MRCI) described in the last section.

Time-independent DFT is based on the Hohenberg-Kohn theorems, which state that in a non-degenerate system,

1. there is a one-to-one mapping of the electronic groundstate density,  $n(\mathbf{r})$  (which depends only on three spatial coordinate) and the groundstate wavefunction (which depends on  $3N_e$  spatial coordinates and  $N_e$  spin coordinates) and
2. there is a one-to-one mapping between the the groundstate wavefunction and the groundstate energy [78].

The energy is calculated from the energy functional

$$E[n(\mathbf{r})] = V[n(\mathbf{r})] + U[n(\mathbf{r})] + T[n(\mathbf{r})] + E_{xc}[n(\mathbf{r})], \quad (\text{I.4.14})$$

where  $V$  is an external potential (i.e.  $V_{n,e} + V_{n,n}$ ). The electron-electron interaction,  $U[n(\mathbf{r})]$ , is given by

$$U[n(\mathbf{r})] = \frac{1}{2} \int d\mathbf{r} \int d\mathbf{r}' \frac{n(\mathbf{r})n(\mathbf{r}')}{|\mathbf{r} - \mathbf{r}'|}. \quad (\text{I.4.15})$$

$T$  is the kinetic energy functional and  $E_{xc}$  denotes the exchange-correlation potential. If the functional form of  $T$  and  $E_{xc}$  were known, density functional theory would yield the exact groundstate energy.

Assuming that the density of this interacting system can also correspond to the density of a yet unknown effective one particle Hamiltonian, one can write [78]

$$n(\mathbf{r}) = \sum_{i=1}^{N_e} |\phi_i^{\text{KS}}(\mathbf{r})|^2, \quad (\text{I.4.16})$$

where the  $\phi_i^{\text{KS}}$  are one-particle functions usually referred to as Kohn-Sham orbitals. This assumption allows the evaluation of the kinetic energy functional using the following expression:  $T = \sum_i \int d^3r \phi_i^{\text{KS}*}(\mathbf{r}) \left(-\frac{\nabla^2}{2}\right) \phi_i^{\text{KS}}(\mathbf{r})$ . The functional  $T$  will then only account for the kinetic energy of the effective non-interacting system and not for that of the complete system. The contributions to the energy not included in  $T$ ,  $V$  and  $U$  are assumed to be taken care of by the unknown exchange-correlation functional  $E_{xc}$ .

Several different functional forms of the exchange-correlation potential have been devised, all of which are only approximations to the true and unknown functional. A popular, but rather simple approximation is the local-density approximation (LDA). In LDA [79, 80, 81, 82] the exchange functional  $E_{xc}$  is an expression of the density  $n(\mathbf{r})$  and does not depend for example on the derivative thereof. The LDA exchange energy is generally calculated analytically from the Hartree-Fock result of the exchange energy for a homogeneous electron gas. The correlation energy for a homogeneous electron gas can only be derived analytically for the limiting cases of high and low density. Most LDA exchange-correlation potentials interpolate between these two limits.

For time-dependent problems, the Runge-Gross theorem takes the role of the Hohenberg-Kohn theorem on which DFT are based [83]. The exchange and correlation functionals may now in principle depend on the entire time evolution of the density, a possibility that is excluded in the adiabatic approximation [83]. A popular choice for a time-dependent exchange-correlation functional is the adiabatic local-density approximation (ALDA).

TDDFT can not only be used to compute the time evolution of a system, TDDFT can also be used to calculate the energies of excited states. This is attained by subjecting

the system to a small time dependent perturbation field. The excitation energies can then be extracted from the poles of the linear-response function of the density [83].

#### **I.4.4. Quantum Chemistry software and basis sets**

Several commercial and non-commercial software packages are available to solve the electronic Schrödinger equation using the afore mentioned methods. In the course of this work, the software package Columbus 7 [84, 85, 86, 87, 88], and Molcas [89] were used for CASSCF, MRCI and CASPT2 methods. These programs are also capable of calculating dipole transition elements and Columbus 7 can calculate nonadiabatic couplings using analytic gradients. For density functional theory calculations (including time dependent calculations) the software package Octopus [90, 91, 92] was used.

While Octopus is grid-based, Columbus and Molcas both make use of atomic basis sets as spatial basis for the electron wavepacket. This limits the calculations to bound electrons, but greatly reduces the numerical effort of the calculation.



## I.5. Electron scattering and impact ionization

One could say that physicists just love to perform or interpret scattering experiments.

---

*(Clifford G. Shull; Nobel Banquet Speech (10 Dec 1994) in Tore Frängsmyr (ed.), Les Prix Nobel)*

In this chapter, a brief introduction to the calculation of electron impact ionization cross-sections will be given.

Assuming the mass of the target to be large compared to the electron mass, the single channel, triply differential cross-section for electron impact ionization is given by [93]

$$\frac{d^3\sigma}{d\Omega_1 d\Omega_2 dE_1} \propto \frac{k_1 k_2}{k_0} |T_{fi}|^2 \delta(E_f - E_i), \quad (\text{I.5.1})$$

where  $T_{fi}$  denotes the transition matrix element from the initial state with energy  $E_i$  to the final state with energy  $E_f$ . The momenta of the two outgoing electrons are given by  $k_1 = \sqrt{2E_1}$  and  $k_2$ ;  $k_0$  denotes the momentum of the incident electron. (Note that this cross-section is sometimes also referred to fivefold differential cross-section, since  $\Omega = (\theta, \phi)$ .)

The transition matrix element is given by [94]

$$T_{fi} = \langle \Psi_f^- | V_{\text{int}} | \Phi_i \rangle, \quad (\text{I.5.2})$$

where  $V_{\text{int}}$  is the interaction of the incoming electron with the target system. If the target system is described via the Hamiltonian  $H_0$ , then the total Hamiltonian is given by

$$H = H_0 + K + V_{\text{int}} = \tilde{H} + V_{\text{int}},$$

where  $K$  is the kinetic energy operator of the incident electron. The final wavefunction  $\Psi_f^-$  is the solution of the full Hamiltonian  $H$  for outgoing boundary conditions. The

wavefunction  $\Phi_i$  is a solution of the non-interacting Hamiltonian  $\tilde{H}$  and is thus given by an anti-symmetrized product of an incident plane wave with momentum  $k_0$  and the  $N$ -particle target state, which is a solution to  $H_0$ .

Equivalently, the transition matrix element can be written as

$$T_{fi} = \langle \Phi_f | V_{\text{int}} | \Psi_i^+ \rangle, \quad (\text{I.5.3})$$

where  $\Phi_f$  is a solution of  $\tilde{H}$  and  $\Psi_i^+$  a solution for  $H$  with incoming boundary conditions.

In a two active electron picture, and random orientation of the spins of the incoming particles, the triply differential cross-section should account for spin singlet and spin triplet configurations and thus [95, 66]

$$\frac{d^3\sigma}{d\Omega_s d\Omega_e dE} = \frac{k_e k_s}{k_i} \left[ \frac{1}{4} |T^+|^2 + \frac{3}{4} |T^-|^2 \right], \quad (\text{I.5.4})$$

where  $T^+$  corresponds to the transition matrix for a symmetrized spatial wavefunction and  $T^-$  the transition matrix for an anti-symmetrized wavefunction.

## Part II.

# Numerical methods

## II.1. Solving the nuclear time-dependent Schrödinger equation

To study nuclear dynamics, it is necessary to integrate the nuclear Schrödinger equation

$$(T\delta_{ab} + U_{ab})\chi_b(\mathbf{R}, t) = -i\frac{\partial}{\partial t}\chi_a(\mathbf{R}, t), \quad (\text{II.1.1})$$

where here and in the following Einstein's summation notation is used. The electronic potential  $U$  may include dipole couplings and non-adiabatic couplings as in Eq. (I.3.15) and Eq. (I.3.12). The indices  $a$  and  $b$  run over all  $N_{\text{st}}$  electronic states included in the ansatz (I.3.14).

Even for a small number  $N_{\text{st}}$  of electronic states, if the molecule has many nuclear degrees of freedom, it is neither feasible to calculate  $U(\mathbf{R})$ , the dipole couplings and non-adiabatic couplings for the entire space, nor to solve the nuclear Schrödinger equation itself. One thus has to resort to approximate methods, such as multi-configurational time dependent Hartree calculations [96] or classical simulations (e.g. [97, 98]). In few dimensions, however, the full equation can be solved numerically.

### II.1.1. Basis representation

The infinite dimensional Hilbert space of the nuclear Hamiltonian is represented in a finite basis. This basis can either be a spectral basis, i.e. orthogonal functions such as plane waves, or a pseudo-spectral basis, i.e. localized functions, which are related to

the spectral basis functions via a unitary transform [71]. In quantum mechanics, both basis representations have their advantages [71]: In spectral basis sets, the kinetic energy operator  $T$  is usually simple to evaluate. In a plane wave basis set, for example, the matrix element  $T_{ij}$  is given by

$$T_{ij} = \langle k|T|k' \rangle = \frac{k^2}{2M} \delta(k - k') \quad (\text{II.1.2})$$

and  $T$  forms a diagonal matrix, allowing fast evaluation of the matrix vector product  $T\chi$ . Furthermore, this expression is more precise than evaluating the action of  $T$  via a finite element representation of the derivative in real space.

Pseudo-spectral basis sets, on the other hand, allow easy evaluation of the potential matrix

$$U_{ij} = \langle f_i|U|f_j \rangle \simeq U(x_i)\delta_{ij}, \quad (\text{II.1.3})$$

where  $f_i$  and  $f_j$  are pseudo-spectral basis functions centred at  $i$  and  $j$  respectively.

One choice of pseudo-spectral basis, which is related to the plane wave basis,  $k_i$ , via the discrete Fourier transform,  $\mathcal{F}_i\{\chi(x_j)\} = \sum_j e^{ik_i x_j} \chi(x_j)$ , is the evenly spaced grid,  $x_i$ . For this basis

$$\langle x_i|f(U)|\chi \rangle = \sum_j \langle x_i|f(U)|x_j \rangle \langle x_j|\chi \rangle = f(U(x_i))\chi(x_i) \quad (\text{II.1.4})$$

$$\langle x_i|f(T)|\chi \rangle = \sum_j \underbrace{\langle x_i|f(T)|x_j \rangle}_{\sum_m \langle x_i|k_m \rangle f(k_m) \langle k_m|x_j \rangle} \quad \langle x_j|\chi \rangle = \mathcal{F}_i^{-1}\{f(k_m) \mathcal{F}_m\{\chi(x_j)\}\} \quad (\text{II.1.5})$$

and

$$\langle k_i|f(T)|\chi \rangle = \sum_j \langle k_i|f(T)|k_j \rangle \langle k_j|\chi \rangle = f(k_i)\chi(k_i) \quad (\text{II.1.6})$$

$$\langle k_i|f(U)|\chi \rangle = \sum_j \underbrace{\langle k_i|f(U)|k_j \rangle}_{\sum_m \langle k_i|x_m \rangle f(U(x_m)) \langle x_m|k_j \rangle} \quad \langle k_j|\chi \rangle = \mathcal{F}_i\{f(U(x_m)) \mathcal{F}_m^{-1}\{\chi(k_j)\}\}, \quad (\text{II.1.7})$$

where  $f(X)$  denotes an arbitrary function of the operator  $X$ .

The split-operator method, which was used in the course of this work and which is described below, can make use of this basis and the above stated relations.

### II.1.2. Time propagation and the split-operator method

To solve the time-dependent Schrödinger equation, several efficient propagation schemes exist. Examples are second order differencing, the short iterative Lanczos scheme [99] or, as applied in this work, the split-operator method, which will be explained in the following [100].

For a sufficiently slowly varying Hamiltonian,  $H(t)$ , and sufficiently small time steps,  $\Delta t$ , the short time propagation  $t \rightarrow t + \Delta t$  of the wavefunction  $\chi(t)$  can be written as [101]

$$|\chi(t + \Delta t)\rangle \approx e^{-iH(t)\Delta t}|\chi(t)\rangle, \quad (\text{II.1.8})$$

This equation can be solved by diagonalizing the Hamiltonian, which is numerically very expensive. The spectral split-operator method, which makes use of the Fourier basis, provides a possibility to avoid the diagonalization of the Hamiltonian. In the Fourier basis, the kinetic energy operator is diagonal in  $k$ -space and the potential energy operator is diagonal in real space. Therefore

$$e^{-iT\Delta t}|k\rangle = e^{-i\frac{k^2\Delta t}{2}}|k\rangle \quad (\text{II.1.9})$$

$$e^{-iU\Delta t}|x\rangle = e^{-iU(x)\Delta t}|x\rangle. \quad (\text{II.1.10})$$

Since  $T$  and  $U$  do not commute  $e^{-i(T+U)\Delta t} \neq e^{-iT\Delta t}e^{-iU\Delta t}$ . However, up to third order in  $\Delta t$ , the propagation operator  $e^{-iH\Delta t}$  can be written approximately as split-operator [71]

$$e^{-iH\Delta t} \approx e^{-\frac{i}{2}U\Delta t}e^{-iT\Delta t}e^{-\frac{i}{2}U\Delta t} + \mathcal{O}(\Delta t^3) \quad (\text{II.1.11})$$

$$\approx e^{-\frac{i}{2}T\Delta t}e^{-iU\Delta t}e^{-\frac{i}{2}T\Delta t} + \mathcal{O}(\Delta t^3). \quad (\text{II.1.12})$$

The split-operator method is both stable and norm conserving [99].

Using the split-operator Eq. (II.1.12), the Schrödinger equation  $(T+U)\chi(\mathbf{R}, t) = -i\frac{\partial}{\partial t}\chi(\mathbf{R}, t)$  can easily be propagated using Eq. (II.1.8)

$$\begin{pmatrix} \chi(k_1, t + \Delta t) \\ \vdots \\ \chi(k_N, t + \Delta t) \end{pmatrix} \approx \left[ \begin{pmatrix} e^{-\frac{i}{2}\frac{k_1^2\Delta t}{2}} & & 0 \\ & \ddots & \\ 0 & & e^{-\frac{i}{2}\frac{k_N^2\Delta t}{2}} \end{pmatrix} \right] \mathcal{F}^{-1}.$$

$$\cdot \begin{pmatrix} e^{-iU(x_1)\Delta t} & & 0 \\ & \ddots & \\ 0 & & e^{-iU(x_N)\Delta t} \end{pmatrix} \cdot \mathcal{F} \begin{pmatrix} e^{-\frac{i}{2} \frac{k_1^2 \Delta t}{2}} & & 0 \\ & \ddots & \\ 0 & & e^{-\frac{i}{2} \frac{k_N^2 \Delta t}{2}} \end{pmatrix} \Bigg] \begin{pmatrix} \chi(k_1, t) \\ \vdots \\ \chi(k_N, t) \end{pmatrix}. \quad (\text{II.1.13})$$

If multiple electronic states and couplings should be included in the calculation ( $T\delta_{ab} + U_{ab}$ ) $\chi_b(\mathbf{R}, t) = -i\frac{\partial}{\partial t}\chi_a(\mathbf{R}, t)$  with  $a \in [1, N_{\text{st}}]$ , the potential  $U_{ab}(x_i)$  will in general not be a diagonal matrix and an additional diagonalization step is necessary in the propagation, i.e.

$$e^{-iU_{ab}(x_i)\Delta t}\chi_b(x_i, t) \Rightarrow M_{ab}e^{-iu_b(x_i)\Delta t}M_{bc}^\dagger\chi_c(x_i, t), \quad (\text{II.1.14})$$

where  $u_a(x_i)$  are the eigenvalues to  $U_{ab}(x_i)$  with  $U_{ad}(x_i) = M_{ab}u_b(x_i)\delta_{bc}M_{cd}$ . Using this transformation, Eq. (II.1.12) can be applied to every component  $\chi_a$ .

### II.1.3. Calculating eigenfunctions - Imaginary time propagation

Eigenfunctions can be obtained from the diagonalization of the nuclear Hamiltonian,  $H$ . An alternative method is to use imaginary time propagation. In this method, a reasonable start wave function is chosen and propagated according to

$$\chi(t_0 + N\Delta t) = \prod_{i_1}^N \hat{N}_i e^{-H\Delta t} \chi(t_0), \quad (\text{II.1.15})$$

where  $\hat{N}_i$  renormalizes the wavefunction  $e^{-H\Delta t}\chi(t_{i-1})$ . Apart from the necessary renormalization, this is equivalent to replacing  $\Delta t \rightarrow -i\Delta t$  in the propagation equation Eq. (II.1.8) [102].

To see that this procedure yields the ground state, we write  $\chi_0$  as a sum of eigenstates  $\phi_i$  of the Hamiltonian  $H$

$$\chi(t_0) = \sum_{i=1}^{N_0} a_i(t_0)\phi_i. \quad (\text{II.1.16})$$

It follows that

$$\chi(t_0 + \Delta t) = \sum_{i=1}^{N_0} \underbrace{e^{-\epsilon_i \Delta t} a_i(t_0)}_{a_i(t_0 + \Delta t)} \phi_i. \quad (\text{II.1.17})$$

The coefficients  $a_i$  are thus exponentially damped (or amplified) according to the eigenenergy of the state  $\phi_i$ . Since the ground state has the smallest energy, the damping of  $a_0$ , will be smallest and after a long enough propagation time, the wavefunction  $\chi(t)$  will approximate the vibrational ground state:  $\chi(t) \approx \phi_0$ . This is only true, however, if the trial wavefunction  $\chi(t_0)$  contains the vibrational ground state. To calculate higher excited states, it is necessary to project lower lying states out after each time step.

#### II.1.4. Grid size, resolution and absorbing boundaries

To obtain correct results in a dynamics calculation, the spacial grid size  $L$  has to be large enough to capture the entire wavepacket and the grid resolution  $\Delta x$  has to be dense enough to resolve the wavepacket spatially. At the same time, the grid size in  $k$ -space,  $k \in [-\frac{\pi}{\Delta x}, \frac{\pi}{\Delta x}]$ , has to be larger than the maximum momentum of the wavepacket and the resolution in  $k$ -space,  $\Delta k = \frac{2\pi}{L}$  has to resolve the momentum during the entire propagation. If either the spacial or the momentum grid are too small, and the wavepacket reaches the edge of the grid, it will be wrapped around at the grid boundary as shown in figure II.1.1 for a free wavepacket.

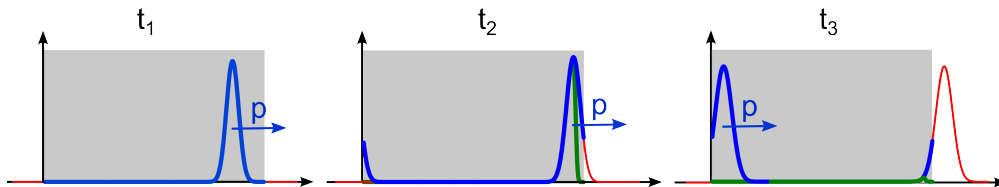


Figure II.1.1.: Wrapping at grid boundaries: red line: correct result, blue line: result for a grid length as indicated by the gray square, green line: result for the same grid, but using absorbing boundaries (note the decreasing norm of the wavefunction shown in green).

Especially if dissociating wavepackets are propagated over a long time period, this causes computational problems since the grid would have to be very large. A possible alternative is to use absorbing boundaries. This can be achieved by applying a smooth mask function to the wavefunction after every propagation step, or, equivalently, by introducing a short ranged negative imaginary potential in the Hamiltonian at the boundaries [103].

## *II.1. Solving the nuclear time-dependent Schrödinger equation*

---

The mask function has to be smooth enough to avoid reflections and the creation of strong spurious frequency components due to the sharp cutoff. Alternative and typically superior methods are the use of complex potentials [104] or exterior complex scaling [105]. For the simulations performed in the course of this work, mask functions were used which decrease smoothly from one to zero at the boundaries. If mask functions are applied, the norm of the wavefunction is no longer conserved.



## II.2. Classical trajectory Monte Carlo

In Classical trajectory Monte Carlo (CTMC) simulations, the evolution of a quantum mechanical object is approximated semi-classically by propagating an ensemble of trajectories. Each trajectory is assigned an initial phase-space coordinate, which is randomly chosen from a distribution representing the quantum object. Then, each trajectory is propagated classically in time according to Newton's equations of motion.

$$\mathbf{p} = m \frac{\partial \mathbf{x}}{\partial t}, \quad (\text{II.2.1})$$

$$\frac{\partial \mathbf{p}}{\partial t} = \mathbf{F} = -\nabla_{\mathbf{x}} V \quad (\text{II.2.2})$$

CTMC calculations allow analysing dynamics in a much larger dimensional space than quantum simulations, since the computational effort only scales with the number of trajectories propagated and not exponentially with the dimension of the configuration space. A drawback is of course, that the semi-classical method cannot capture all quantum effects inherent to the system.

### II.2.1. The Runge-Kutta-Fehlberg method

To solve the classical equations of motion, Eqs. (II.2.1) and (II.2.2), the Runge-Kutta-Fehlberg method was used. This iterative method for numerically solving ordinary differential equations belongs to the class of Runge-Kutta algorithms and uses an adaptive stepsize in the propagation [106, 107].

The Runge-Kutta-Fehlberg-4(5) method starts by applying the Runge-Kutta algorithm

of fourth and fifth order with a stepsize  $h$  to the differential equation  $y' = f(x, y)$ :

$$y_1 = y_0 + h \sum_{\kappa=0}^4 c_{\kappa} f_{\kappa} + \mathcal{O}(h^5) \quad (\text{II.2.3})$$

$$\hat{y}_1 = y_0 + h \sum_{\kappa=0}^5 \hat{c}_{\kappa} f_{\kappa} + \mathcal{O}(h^5), \quad (\text{II.2.4})$$

where

$$f_{\kappa} = f\left(x_0 + \alpha_{\kappa} h, \sum_{\lambda=0}^{\kappa-1} \beta_{\kappa\lambda} f_{\lambda}\right) \quad \kappa \geq 1, \quad (\text{II.2.5})$$

and  $f_0$  is defined via the initial values  $(x_0, y_0)$  as  $f_0 = f(x_0, y_0)$ . For the parameters  $\alpha$ ,  $\beta$ ,  $c$  and  $\hat{c}$  different choices exist. One choice proposed in Ref. [106] is given by

$\alpha_{\kappa}$	$\beta_{\kappa\lambda}$					$c_{\kappa}$	$\hat{c}_{\kappa}$
0						$\frac{25}{216}$	$\frac{16}{135}$
$\frac{1}{4}$	$\frac{1}{4}$					0	0
$\frac{3}{8}$	$\frac{3}{32}$	$\frac{9}{32}$				$\frac{1408}{2565}$	$\frac{6656}{12825}$
$\frac{12}{13}$	$\frac{1932}{2197}$	$-\frac{7200}{2197}$	$\frac{7296}{2197}$			$\frac{2197}{4104}$	$\frac{28561}{56430}$
1	$\frac{439}{216}$	-8	$\frac{3680}{513}$	$-\frac{845}{4104}$		$-\frac{1}{5}$	$-\frac{9}{50}$
$\frac{1}{2}$	$-\frac{8}{27}$	2	$-\frac{3544}{2565}$	$\frac{1859}{4104}$	$-\frac{11}{40}$		$\frac{2}{55}$

If the error estimate,  $\varepsilon = |y_1 - \hat{y}_1|$ , is larger than the error tolerance  $\varepsilon_{\text{tol}}$ , the step is rejected and the stepsize decreased. If  $\varepsilon < \varepsilon_{\text{tol}}$  the step is accepted and the stepsize,  $h$  is adjusted for the next step [108]

$$h_{\text{new}} = 0.9 h \left( \frac{\varepsilon_{\text{tol}}}{\varepsilon} \right)^{0.2}. \quad (\text{II.2.6})$$

## II.2.2. Gaussian distributed random numbers

In most programming languages, it is only possible to generate evenly spaced pseudo-random numbers. To generate Gaussian distributed random numbers for the initial values from evenly distributed random numbers, the Box-Muller transform can be used: Consider two random numbers,  $u$  and  $v$ , drawn from a uniform distribution in the interval  $]0, 1[$ . Then

$$x = \sqrt{-2 \ln(u)} \cos(2\pi v) \quad (\text{II.2.7})$$

is normal distributed [109] and hence

$$y = x\sigma + \mu \tag{II.2.8}$$

is Gaussian distributed around  $\mu$  with a standard-deviation of  $\sigma$ .



## Part III.

# Strong-field ionization of $\text{H}_2^+$ in circularly polarized light

### III.1. Introduction

Strong-field ionization can be described qualitatively within the tunnelling and multi-photon picture. The full numerical description of the ionization process is only possible for very small systems, such as H, He and  $\text{H}_2^+$ . For larger systems, electron-electron correlation, multi-electron effects and the anisotropy of the Coulomb potential are usually neglected in theoretical calculations and the strong-field approximation (SFA) is invoked, in which the Coulomb potential is neglected in the continuum. These assumptions form, for example, the basis of the molecular ionization-rate equation derived by Tong, Zhao and Lin [26]. However, experimental and theoretical investigations have shown that both these assumptions lead to severe shortcomings of the derived theories even in the atomic case and even if recollision events are not of interest (see e.g. [110, 64, 63, 111, 65, 112, 113]). Recently, several experiments have been performed investigating the strong-field ionization of molecules [114, 115, 116, 117, 118, 119, 120], including  $\text{H}_2^+$  in circularly polarized fields. This smallest of molecules,  $\text{H}_2^+$ , can in principle be fully described by quantum dynamics calculations. But even in this case, open questions remain.

Strong deviations are observed for example in the photoelectron momentum spectrum (PES) of  $\text{H}_2^+$  in circularly polarized fields between the experimental results and SFA predictions. The origin of these discrepancies is still debated: is it the long-range Coulomb potential causing the deviations from SFA or is it laser-driven electron dynamics prior to ionization? Instead of trying to reproduce the results using a fully quantum description, as for example in Ref. [116], this work focusses on analysing the various factors

of influence possibly contributing to the PES and at disentangling their respective contributions. To this end, classical trajectory Monte Carlo (CTMC) simulations are performed. Although it is not a priori clear to what extent semi-classical approximations can capture the relevant processes, CTMC calculations have the advantage of allowing an intuitive and straight-forward interpretation of the results. As will be shown, many experimentally observed trends can be reproduced by the model.

## III.2. The model

The ionization dynamics in  $\text{H}_2^+$  due to a strong, circularly polarized laser-field is modelled using a two dimensional semi-classical model. The model is restricted to the  $x, y$ -plane, corresponding to the polarization plane of the laser. The molecule is aligned along the  $x$  axis, as shown in Fig. III.2.1.

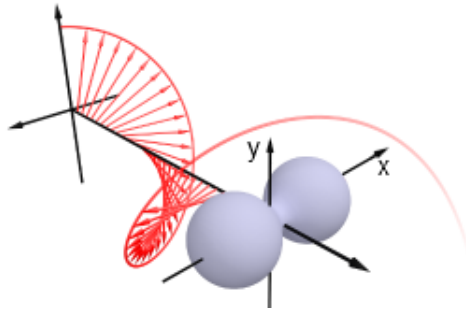


Figure III.2.1.: Geometrical setup of the numerical calculations: Molecule aligned along  $x$ , laser polarization plane:  $x - y$  plane, circularly polarized in clockwise direction.

An ensemble of classical trajectories, consisting typically of around 100 000 trajectories, is propagated in the combined action of the Coulombic and the electric field according Newton's equation of motion

$$\ddot{\mathbf{r}}(t) = -\nabla V(\mathbf{r}(t)) - \mathbf{E}(t) \quad (\text{III.2.1})$$

using a Runge-Kutta-Fehlberg algorithm with adaptive stepsize (see Sec. II.2.1). The trajectories are started at a time  $t_0$ , which is considered as the moment of ionization. Each

trajectory is assigned a time dependent weight-factor,  $w(t_0)$ , representing the tunnelling probability at  $t_0$ , an initial coordinate  $\mathbf{r}_0$  in the continuum and an initial momentum  $\mathbf{p}_0$ . The initial phase-space coordinates are sampled randomly from a time dependent phase-space distribution  $\rho(\mathbf{r}_0, \mathbf{p}_0; t_0)$ , as described in the next section. For very large field strengths, ionization can proceed classically over-the-barrier. To allow a smooth transition from tunnelling to over-the-barrier ionization, tunnelling ionization and over-the-barrier ionization are described on equal footing: In both cases, the trajectories are released at a moment  $t_0$  with a probability  $w(t_0)$  at a point  $\mathbf{r}_0(t_0)$  into the continuum with a smooth transition from the below-barrier to the over-the-barrier case.

In the present simulations, the starting times,  $t_0$ , of the trajectories are restricted to the central field cycle to prevent smearing of the results due to intensity averaging and the central field cycle is evenly sampled.

The ionic potential of the molecule acting on the electron is represented by a soft-core potential

$$V(x, y) = \frac{1}{R} - \frac{1}{\sqrt{\left(x - \frac{R}{2}\right)^2 + y^2 + a^2}} - \frac{1}{\sqrt{\left(x + \frac{R}{2}\right)^2 + y^2 + a^2}}, \quad (\text{III.2.2})$$

where  $a = 0.5 \text{ au}$  is the soft core parameter. The internuclear distance,  $R$ , is kept fixed during the propagation of the trajectories. Although the molecule, once subjected to the laser field, will move through a range of internuclear distances with varying ionization probability [121], this approximation is reasonable: due to the large mass ratio between electron and nuclei, the electron moves much faster than the nuclei, and in a circularly polarized field, the probability of the electron returning to the ion is low. It is therefore a reasonable assumption to keep the nuclei fixed during the propagation of the electron after ionization.

Trajectories, which have a negative total energy after one half-cycle propagation in the field are considered to be bound and are not taken into account in the evaluation.

The electric field,  $\mathbf{E}(t) = \frac{1}{c} \frac{\partial \mathbf{A}(t)}{\partial t}$ , shown in Fig. III.2.2, is defined via vector potential

$$\mathbf{A}(t) = \frac{c}{\omega} E_0 f(t) \begin{pmatrix} -\sin(\omega t) \\ -\cos(\omega t) \end{pmatrix}, \quad (\text{III.2.3})$$

where  $c$  is the speed of light and the rotational frequency  $\omega = 0.057 \text{ au}$  corresponding to carrier wavelength of  $\lambda = 800 \text{ nm}$ . The envelope function  $f(t)$  is given by a  $\sin^2$  pulse

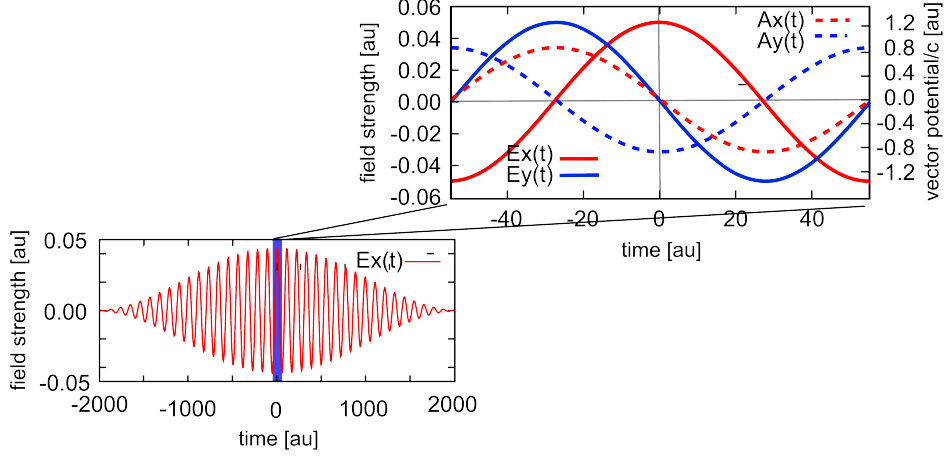


Figure III.2.2.: Electric field and vector potential.

with a full width at half maximum of 50 fs. Maximum intensities in the range from  $6 \times 10^{13} \text{ W/cm}^2$  to  $6 \times 10^{14} \text{ W/cm}^2$  are analysed.

### III.2.1 Initial phase-space distribution and weight factors

Since tunnelling is an intrinsically quantum mechanical process, it is not a priori clear how to choose the initial values  $w(t_0)$ ,  $\mathbf{r}(t_0)$  and  $\mathbf{p}(t_0)$ . The Delone-Krařnov [59] expression, Eq. (I.2.5), provides a semi-classical phase-space distribution for the electrons after tunnelling which is used in the present work.

Since the Delone-Krařnov expression was derived for atoms, whenever necessary,  $\text{H}_2^+$  is treated as two individual atomic cores, distinguished by the subscripts  $l$  (left) and  $r$  (right). Each core is assigned a weight-factors,  $w_{l/r}(t_0)$ , defined via tunnelling rate and the probability to find the electron on the left or right core, and an initial phase-space distribution  $\rho_{l/r}(\mathbf{x}_0, \mathbf{p}_0; t_0)$  according to the Delone-Krařnov expression. It should be noted parenthetically that the Keldysh parameter (Eq. (I.2.2)) is around one for the laser parameters used. According to Keldysh [10] (see section I.2.2), the present conditions thus do not correspond unambiguously to the tunnelling regime. Additionally, the parameters are near or in the over-the-barrier regime.

Additionally to the Delone-Krařnov expression, a modified ionization rate equation was used: as mentioned in the introduction, field-driven electronic dynamics are debated to have a strong influence on the ionization dynamics and the photoelectron spectrum. Two



dimensional quantum dynamical calculations for  $H_2^+$  in a short, intense laser pulse indeed show that the outward electron flux shows a complicated time behaviour with multiple ionization events per laser cycle (see Fig. III.2.3). These are not reproduced by the Delone-Krařnov expression. In fact, they have been associated to the bound sub-cycle electron dynamics [122]. In the present work, the influence of electronic dynamics was

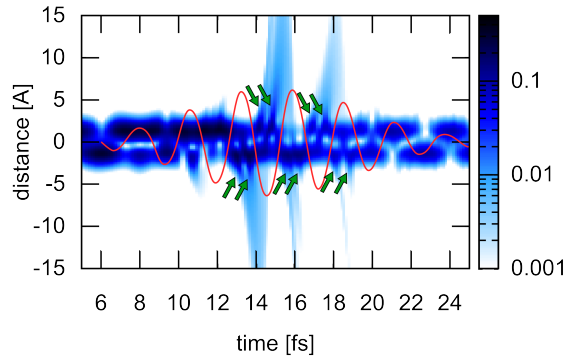


Figure III.2.3.: Electron density in a 2D quantum model of  $H_2^+$  subjected to an intense laser field. The arrows indicate the multiple ionization bursts per half cycle.

examined by altering the Delone-Krařnov expression for the tunnelling rate to mimic the complex temporal ionization dynamics and by adding an additional initial momentum component.

The following paragraphs detail the choice and definition of the initial conditions and weight factors.

### The ionization potential

The ionization potential enters both, the weight factors,  $w(t_0)$ , and the initial phase-space distribution,  $\rho(\mathbf{x}_0, \mathbf{p}_0; t_0)$ . However, since the laser field influences the electronic states, the following three models were applied:

- In the field-free case, the ionization potential of the first two electronic states of  $H_2^+$ , the gerade ( $g$ ) and ungerade ( $u$ ) state, is given by

$$I_P^{\text{field free}} = \frac{1}{R} - U_i(R), \quad (\text{III.2.4})$$

where  $i \in \{g, u\}$  and the potentials  $U_i$ , shown in Fig. III.2.4, are given by  $U_i(R) = E_{\text{elec}}^i(R) + V_{nn}(R)$ , where  $E_{\text{elec}}^i$  are the electronic eigenenergies of state  $i$ , as detailed in chapter I.3.

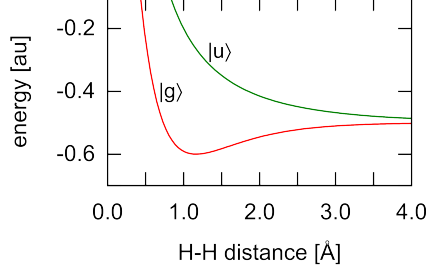


Figure III.2.4.: Potentials for the gerade (g) and ungerade (u) state.

- In a (quasi-)static field, the light induced potentials, which correspond to eigenstates in the static field case, take the role of  $U_{g/u}$ . The light induced potentials are given approximately by

$$T(t_0) \begin{pmatrix} U_g & -\mu E_x(t_0) \\ -\mu E_x(t_0) & U_u \end{pmatrix} T(t_0)^\dagger = \begin{pmatrix} U_{\text{low}}^{\text{LI}}(t_0) & 0 \\ 0 & U_{\text{up}}^{\text{LI}}(t_0) \end{pmatrix}, \quad (\text{III.2.5})$$

where  $T$  is a unitary matrix. In this approximation, higher excited states were neglected due to their weak coupling to the gerade and ungerade state. For the dipole moment, only the component parallel to the molecular axis,  $\mu \approx \frac{R}{2}$ , was taken into account, since it is much larger than the orthogonal component.

- Alternatively, the eigenenergies  $U^{\text{Fl}}$  of semiclassical dressed states (Floquet states) in a two level system were considered [123]. The  $U_i^{\text{Fl}}$  are given by

$$\begin{pmatrix} U_{\text{low}}^{\text{Fl}}(t_0) \\ U_{\text{low}}^{\text{Fl}}(t_0) \end{pmatrix} \approx \begin{pmatrix} -1 \\ 1 \end{pmatrix} \frac{U_u - U_g}{2\omega} J_0(\zeta(t_0)) + 0.5 (U_u + U_g), \quad (\text{III.2.6})$$

where  $J_0(\zeta)$  are Bessel functions and  $\zeta = 2\mu \cdot \tilde{f}(t_0)/\omega$ , where  $\tilde{f}(t)$  denotes the envelope function of the electric field. The above expression is expected to be a good approximation if  $(U_u - U_g)/\omega \ll \sqrt{\frac{\mu E_0}{\omega}} \gg 1$  [123].

### The weight factor

The weight factor  $w_{l/r}(t_0)$  was chosen to be proportional to the ionization rate,  $\Gamma_{l,r}(t_0)$ , times the probability  $\sigma_{l/r}$ , to find the electron on the left or right core

$$\sigma_{l/r}(t_0) = \frac{1}{2} \left| \left( \langle g | \pm \langle u | \right) \phi(t_0) \right|^2, \quad (\text{III.2.7})$$

where  $\phi(t_0)$  is the electronic eigenstate considered. For the field-free gerade and ungerade states ( $|g\rangle$  and  $|u\rangle$ ), this probability is always 0.5. For statically polarized states corresponding to the light-induced potentials,  $\sigma_{l/r}(t_0)$  can be calculated from

$$|\phi(t_0)\rangle = T(t_0) \begin{pmatrix} c_g^0 \\ c_u^0 \end{pmatrix} \cdot \begin{pmatrix} |g\rangle \\ |u\rangle \end{pmatrix}, \quad (\text{III.2.8})$$

where the matrix  $T$  is defined via Eq. III.2.5, and the coefficients  $c_i^0$  define the state the system occupied before the laser pulse, i.e.  $(c_g^0, c_u^0) = (1, 0)$  if the system is assumed to have been in gerade state prior to the advent of the laser pulse. The semiclassical dressed states corresponding to  $U^{\text{Fl}}$ , are given in Ref. [123]. Their overlap with  $(|g\rangle \pm |u\rangle)$  is given by [124]

$$\sigma_{l/r}(t_0) = 0.5 \pm \frac{U_u - U_g}{\omega} \sum_k \frac{1}{2k+1} J_{2k+1}(\zeta(t_0)) \cos(\omega t_0 (2k+1)), \quad (\text{III.2.9})$$

when starting from the gerade state.

### The ionization rate

The ionization rate,  $\Gamma_{l/r}(t_0)$ , was chosen to be either described by the Delone-Krařnov expression (in the following referred to as ADK-like) or to mimic the multiple ionization bursts described above. In the former case, the rate  $\Gamma^{\text{ADK}}$  is given by the  $p$ -independent part of Eq. (I.2.5) where only the  $E_x$  component of the electric field entered the equation to mimic the fact, that  $H_2^+$  will preferentially ionize along the molecular axis. To account for the spatial extent of the molecule, with one core situated at  $\frac{R}{2}$  and the other at  $-\frac{R}{2}$ , the ionization potential was replaced by  $\tilde{I}_P = I_P \pm E_x \frac{R}{2}$  for the field facing and averted nucleus, respectively. (This shifted ionization potential  $\tilde{I}_P$  only entered the Delone-Krařnov expression. The original definition of  $I_P$  was kept when calculating the starting point of the trajectory.)

In Ref. [122], the multiple ionization bursts (MIBs) (Fig. III.2.3) have been related to the electron localization dynamics of Floquet states. To mimic multiple ionization bursts in the semiclassical calculations, the Delone-Krařnov expression is altered according to

$$\Gamma_{l/r}^{\text{MIB}}(t_0) = \Gamma^{\text{ADK}}(t_0)e^{\alpha(\sigma_{l/r}(t_0)-0.5)}, \quad (\text{III.2.10})$$

where  $\alpha = 50$  controls the modulation depth of the multiple ionizations with changing localization  $\sigma_{l/r}$  of the electron. For consistency and as only the temporal behaviour of the Floquet states will lead to multi-ionization bursts when applying the above expression, this ionization rate was only applied in connection with an ionization potential and electronic density resulting from Floquet states. Changing from an ADK-like ionization behaviour to  $\Gamma^{\text{MIB}}$ , allows comparing the two different models and analysing the influence of MIBs on the resulting photoelectron spectrum.

### Starting point $\mathbf{r}_0$ of the trajectories

For each trajectory, the tunnel-exit  $\mathbf{r}_0$  was defined as shown in Fig. III.2.5: For each

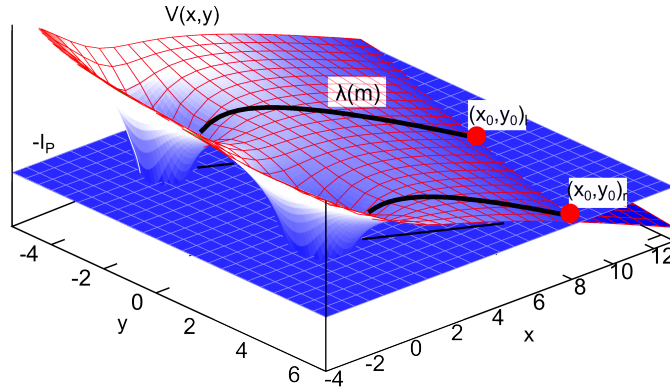


Figure III.2.5.: Definition of the start position  $(x_0, y_0)$  for the left ( $l$ ) and right ( $r$ ) core in the below-barrier case.

nucleus, a parametric line  $\lambda(m)$ , running in  $-\mathbf{E}(t_0)$ -direction and starting at the core was defined. The tunnel exit  $\mathbf{r}_0 = (x_0, y_0)$ , was then defined as the point where  $V(\lambda(m)) = -I_p$ . In the over-the-barrier case, i.e. if  $V(\lambda(m)) < -I_p$ , the tunnel exit was set to the coordinate along  $\lambda(m)$ , where  $V(\lambda(m))$  is extremal.

### Initial momentum distribution

The initial momenta,  $p_0^{\parallel}$  and  $p_0^{\perp}$ , parallel and orthogonal to the instantaneous electric field  $\mathbf{E}(t_0)$ , were chosen from two Gaussian distributions as defined by the Delone-Krařnov expression, Eq. (I.2.5) using  $\tilde{I}_P$  as ionization potential. This definition was also kept in the above barrier case to allow a smooth transition from the below to the over-the-barrier regime.

## III.3. Numerical results and discussion

Figure III.3.1 shows results for the angle-resolved photoelectron spectrum (PES) obtained with the above described method for an intensity of  $1.5 \times 10^{14} \text{ W/cm}^2$ , an internuclear distance of  $R = 2 \text{ \AA}$  and an ADK-type ionization rate. The ionization potential

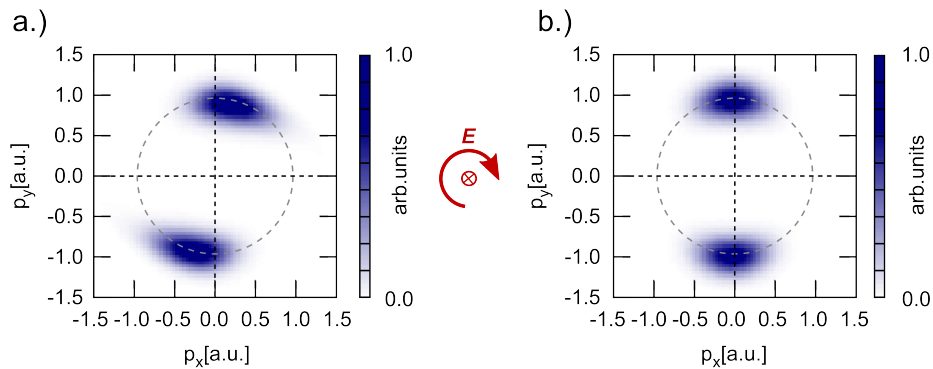


Figure III.3.1.: Photoelectron momentum spectrum for an intensity of  $1.5 \times 10^{14} \text{ W/cm}^2$ , an internuclear distance of  $R = 2 \text{ \AA}$ , an ADK-type ionization rate and  $I_P$  defined via light induced potentials. a.) with Coulomb field, b.) neglecting the Coulomb attraction during the propagation in the continuum. The dashed circle indicates  $p = E/\omega$ .

was assumed to be given via the energetically lower lying light-induced potential,  $V_{\text{low}}^{\text{LI}}$ . For these parameters, ionization is always below barrier. The dashed circle corresponds to  $\frac{A_0}{c} \approx \frac{E_0}{\omega}$ .

A striking feature is that the calculated PES is not centred along the  $y$ -axis if the Coulomb attraction is taken into account (Fig. III.3.1.a), but shows an angular shift

in the rotation direction of the electric field. This shift is also observed in the experiments [116, 119]. In contrast, neglecting the Coulomb force in the propagation of the trajectories (see Fig. III.3.1.b), leads to a PES which is centred around the y-axis, i.e. orthogonal to the molecular axis. This can be expected from the SFA: According to the SFA, a trajectory with zero initial momentum will have a final momentum given by  $\mathbf{p}_f^{\text{SFA}} = -\frac{1}{c}\mathbf{A}(t_0)$ . For  $\text{H}_2^+$ , the largest ionization probability is expected for  $|E_x(t_0)| = E_0$ , i.e. when  $A_x(t_0) = 0$  and  $|A_y(t_0)| = A_0$  and therefore  $\mathbf{p}_f^{\text{SFA}} = (0, \pm\frac{A_0}{c})$ . Taking into account the initial velocity distribution, which is centred around zero and the temporal distribution of the ionization probability, which is centred around the maxima of the electric field, the final momenta can thus be expected to be centred around  $\mathbf{p}_f^{\text{SFA}} = \pm A_0 \hat{\mathbf{y}}$ .

When including the Coulomb potential a clockwise shift observed for clockwise circularly polarized light. This can easily be understood when considering the course of the classical trajectories and the action of the Coulomb force, as shown schematically in Fig. III.3.2. For anticlockwise polarization, the situation is similar, but an electron released at  $\mathbf{E}(t) = E_0 \hat{\mathbf{x}}$  will drift in  $-\hat{\mathbf{y}}$  direction and the Coulomb force will thus lead to a shift in anticlockwise direction.

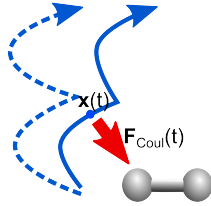


Figure III.3.2.: Schematic pathway of trajectories released at  $\mathbf{E}(t) = E_0 \hat{\mathbf{x}}$  including (solid line) and neglecting (broken line) the Coulomb field in the propagation.

Overall, this situation is very similar to atoms in elliptically polarized or very short laser pulses [65, 125, 126, 127, 128]. In the atomic case, the ellipticity of the field leads to a maximum in the ionization rate in the direction of the semi-major axis of the field, in the molecular case, we expect the ionization rate to be large parallel to the molecular axis. In both cases, deviations from the SFA predictions are found. In the case of molecules, the situation is more complicated though, since the molecular Coulomb potential is not rotationally symmetric and the electronic dynamics prior to ionization may play a relevant role.

To allow a quantitative analysis, we define the mean rotation angle  $\alpha$ . The angle  $\alpha$  is

measured from the molecular axis (x-axis) in the rotational direction of the electric field, i.e. clockwise in the present calculations. The angle  $\alpha$  is the weighted mean of the angular distribution obtained from the final photoelectron spectrum integrated over all radial momenta. The average is thereby taken from one minimum in the distribution to the next, such that  $\alpha$  lies in the upper hemisphere. The mean rotation angle corresponding to the PES shown in Fig. III.3.1.a, is given by  $\alpha = 105^\circ$ . Neglecting the Coulomb force in the propagation (Fig. III.3.1.b),  $\alpha = 90^\circ$ . The Coulomb field thus leads to a  $15^\circ$  shift in the PES.

For higher laser intensities, the observed shift remains and even increases as can be seen in Fig. III.3.3, where the broken lines indicate the value of  $\alpha$ .

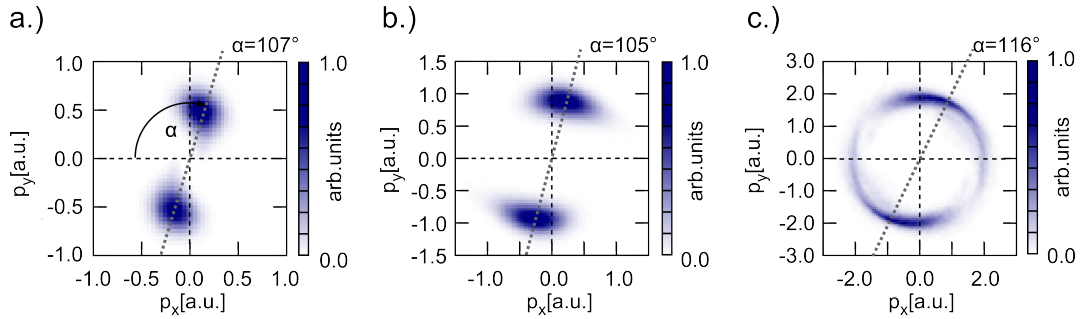


Figure III.3.3.: Photoelectron momentum spectrum for different intensities: a.)  $6.0 \times 10^{13} \text{ W/cm}^2$ , b.)  $1.5 \times 10^{14} \text{ W/cm}^2$ , c.)  $6.0 \times 10^{14} \text{ W/cm}^2$ . (Note the different axis range.) All other parameters as in Fig. III.3.1.

Similarly, the rotation angle  $\alpha$  increases for increasing internuclear distances as shown in Fig. III.3.4. The discontinuity in the line for  $6 \times 10^{14} \text{ W/cm}^2$  at  $R = 2 \text{ \AA}$  occurs, where ionization starts to proceed over the barrier. Fig. III.3.4 also shows once more the intensity dependence of the results: Over a large range of intensities, the angular shifts depend only weakly on the intensity. Only at very high intensities, the rotation of the PES increases. This observation agrees well with the experimental observations in Ref. [119], but is — at a first glance — rather astonishing, since, at higher intensities, one would expect the results to approach the SFA limit. Within the classical trajectory picture, however, the intensity independence can easily be explained: The intensity does not only influence the forces acting on the electron in the continuum, it also affects the tunnel exit.

To allow a detailed analysis, Fig. III.3.5 shows the mean rotation angle obtained for a

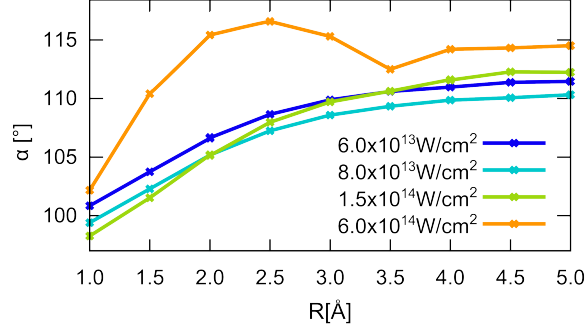


Figure III.3.4.: Mean angle  $\alpha$  for different internuclear distances,  $R$ , and intensities,  $I$ . The ionization potential,  $I_P$ , is defined via the light-induced potential.

modified tunnelling exit

$$x_0 = -r_0 \cos \phi - \frac{R}{2} \cos \phi \quad (\text{III.3.1})$$

$$y_0 = -r_0 \sin \phi \quad (\text{III.3.2})$$

at fixed distance  $r_0$  to the cores. The angle  $\phi$  in the above expression corresponds to the instantaneous polarization direction of  $\mathbf{E}(t_0)$  at the time of birth  $t_0$  of the trajectory. The shift of  $\frac{R}{2}$  in the  $x$ -component accounts for the spacial extent of the molecule with one nucleus lying at  $\frac{R}{2}$  and the other at  $-\frac{R}{2}$ .

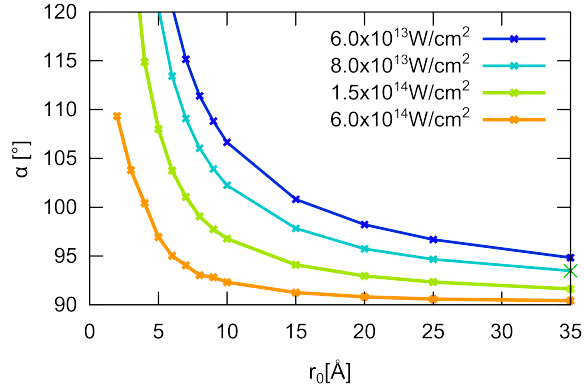


Figure III.3.5.: Mean angle of the final photoelectron momentum for tunnel exits as defined by Eqs. (III.3.1) and (III.3.2) for  $R = 3 \text{ \AA}$

As the distance,  $r_0$ , of the tunnel exit from the ion increases, the rotation angle  $\alpha$



approaches  $90^\circ$ . Additionally, for a fixed tunnelling exit, increasing intensities lead to results which are closer to the SFA predictions of  $\alpha = 90^\circ$ . This is clearly in agreement with the expectations from SFA: The further the tunnel exit from the molecule and the larger the intensity, the smaller the relative influence of the Coulomb field and hence the smaller the deviation from the SFA predictions.

The fact that the rotation angle is independent of the field strength over a wide range of intensities can thus be understood as the consequence of two rivalling processes: on the one hand, the stronger field strength will reduce the relative effect of the Coulomb field at a fixed distance; on the other hand, the trajectories will start closer to the nucleus, in a region of strong Coulomb interaction.

A similar argument also explains the increasing rotation angle for increasing internuclear distance as shown in Fig. III.3.4: The ionization potential  $I_P$  decreases for increasing internuclear distances. Therefore, the tunnel exit,  $r \approx \frac{I_P}{E(t_0)}$ , moves closer to the nuclei which results in a stronger Coulomb attraction and a stronger rotation of the PES. This is also in accordance with experimental results.

So far, only radial momentum-integrated results have been presented. In Fig. III.3.6, the angular distribution for three different integration ranges of the final momentum  $p_f$  are shown: (a) low final momenta with  $p_f < 0.7$  au, (b) medium final momenta with  $0.7 \leq p_f \leq 1.2$  au and (c) high momenta with  $p_f > 1.2$  au for a laser intensity of  $1.5 \times 10^{14}$  W/cm<sup>2</sup> and two different internuclear distances,  $R = 2$  Å and  $R = 4$  Å.

In both cases, the angular rotation increases with increasing final momentum. In the case of  $R = 2$  Å, the mean angle increases from  $\alpha = 100^\circ$  over  $105^\circ$  to  $117^\circ$ . For  $R = 4$  Å, the rotation is generally more pronounced starting at  $\alpha = 99^\circ$  at low final momenta and increases much more strongly, such that  $\alpha$  reaches  $109^\circ$  at intermediate momenta and  $145^\circ$  for final momenta above 1.2 au.

The trend of increasing rotation angle  $\alpha$  with increasing final momentum is also shown in Fig. III.3.7, where additionally a comparison for two different intensities is shown ( $I = 1.5 \times 10^{14}$  W/cm<sup>2</sup> and  $I = 4.0 \times 10^{14}$  W/cm<sup>2</sup>). The increase of  $\alpha$  with increasing final momentum is apparent at both intensities. The phenomenon thus seems to be stable with respect to the laser intensity.

Before analysing this effect in more detail, we will present a comparison with experimental results by M. Spanner et al. [119]. Experimentally, the approximate internuclear distance at which ionization occurred, can be extracted in a three-body coincidence

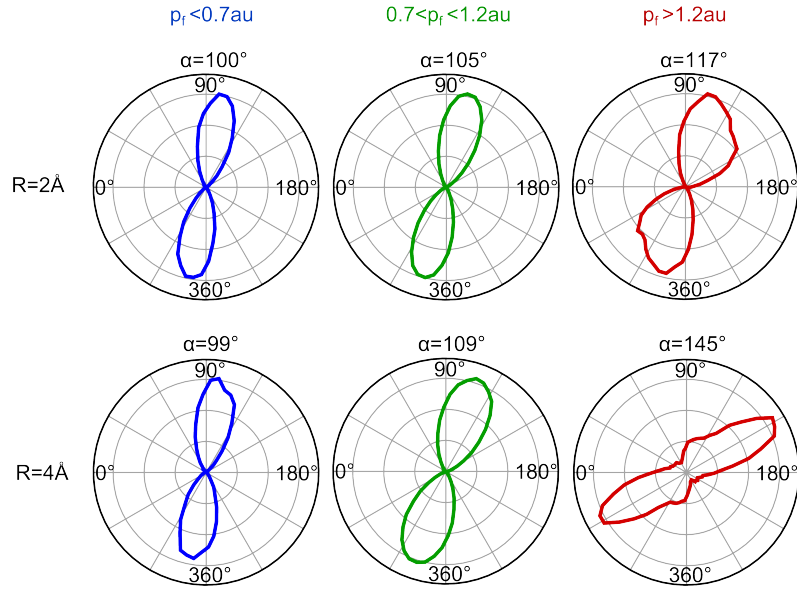


Figure III.3.6.: Momentum and angle resolved photoelectron momentum spectra for two different internuclear distances,  $R = 2 \text{ \AA}$  (upper row) and  $R = 4 \text{ \AA}$  (lower row) for small momenta (left column,  $p_f < 0.7 \text{ au}$ ), medium momenta (middle column,  $0.7 < p_f < 1.2 \text{ au}$ ) and large momenta (right column,  $p_f > 1.2 \text{ au}$ ). All remaining parameters as in Fig. III.3.1.

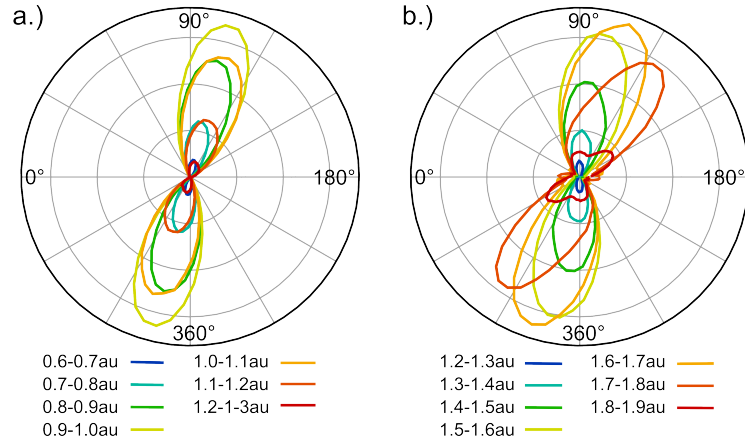


Figure III.3.7.: Comparison of the momentum resolved angular photoelectron momentum distribution for a.)  $I = 1.5 \times 10^{14} \text{ W/cm}^2$  and b.)  $I = 4.0 \times 10^{14} \text{ W/cm}^2$ . Note the increasing rotation of the momentum distribution with increasing final momentum (blue: low final momenta, red: high final momenta).

measurement from the kinetic energy release (KER) of the two nuclei via  $KER \approx c - \frac{1}{R}$  [129, 119], where  $c$  accounts for the initial energy of the molecule prior to dissociation. Such three-body coincidence measurements thus allow the experimental investigation of the momentum and angle resolved photoelectron spectrum for different internuclear distances and can be used for a comparison with the present theoretical results. Fig. III.3.8 shows a reproduction of the experimental results by M. Spanner et al. [119]. Although

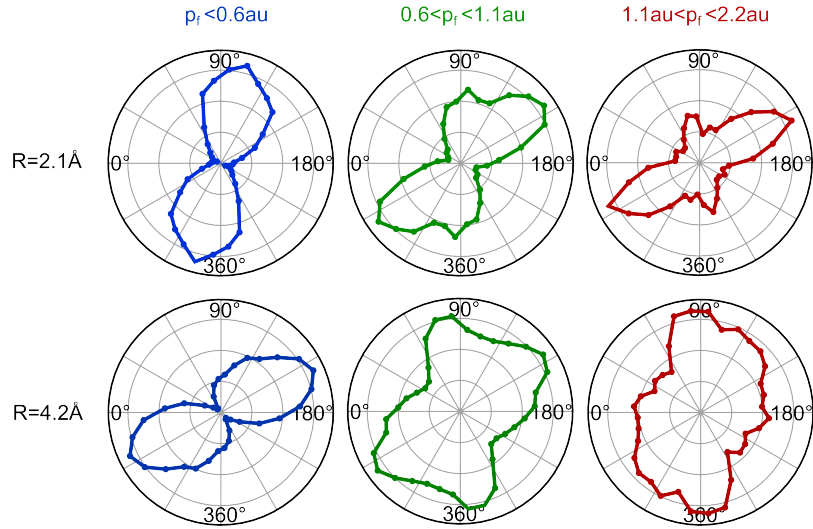


Figure III.3.8.: Reproduction of the results for the momentum and angle resolved PES taken from three body coincidence measurements performed by M. Spanner et al. [119]. ( $I = 3 \times 10^{14} \text{ W/cm}^2$ ). Compare with Fig. III.3.6.

some details, such as the broadening of the momentum distribution with increasing internuclear distance,  $R$ , and some sidelobes observed in the experiment [119], cannot be reproduced by the semiclassical model, several general features apparent in the experiment are well reproduced within the simple model applied in this work. This includes the increase of the rotation angle,  $\alpha$  for increasing internuclear distance discussed earlier, and the increase of  $\alpha$  for increasing final momentum  $p_f$ .

To analyse the dependence of  $\alpha$  on  $p_f$  in more detail, we take advantage of the possibility to perform a one-to-one mapping of the final onto the initial phase-space coordinates of each trajectory. This mapping is shown in Fig. III.3.9 for  $R = 2 \text{ \AA}$  and  $1.5 \times 10^{14} \text{ W/cm}^2$ . Fig. III.3.9 clearly shows that trajectories with very low and very high final momenta correspond to trajectories starting with extreme initial momentum values in both  $x$  and  $y$  direction. This is also true for larger internuclear distances as shown exemplary in Fig. III.3.10 for the  $p_x$ -distribution. While the initial momenta have extremal values for

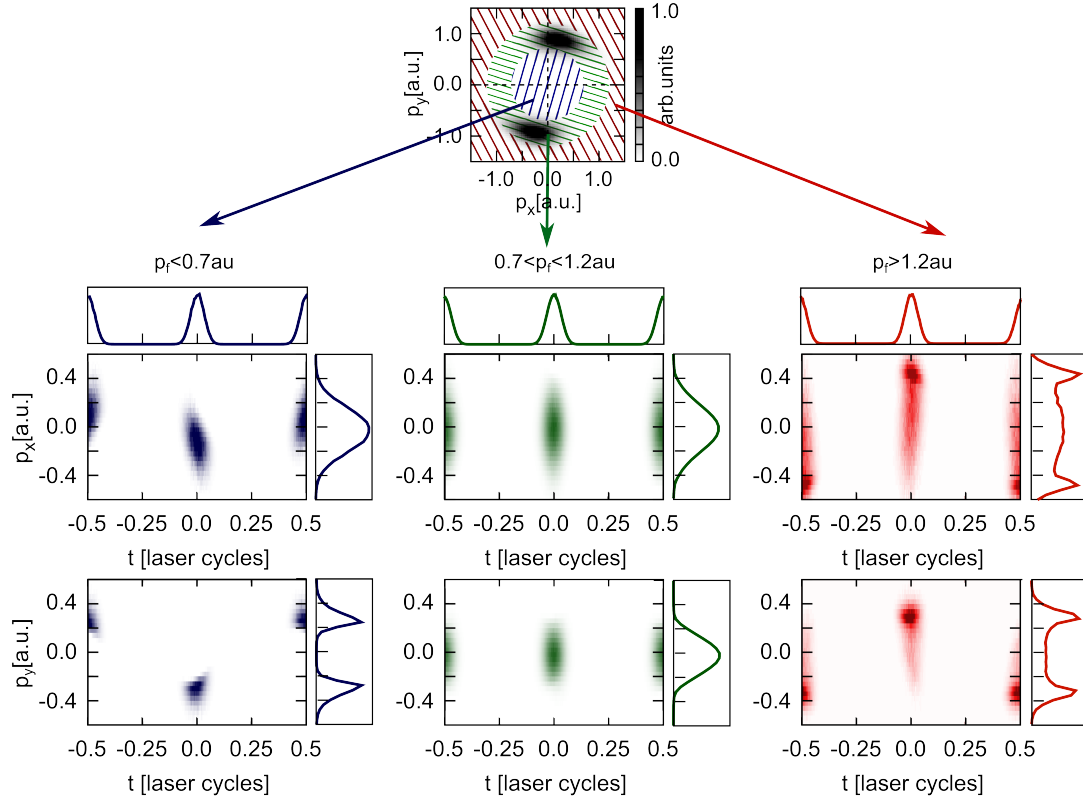


Figure III.3.9.: Mapping of final momenta (uppermost panel) to starting time and initial momenta, in  $x$ - (upper row) and  $y$ -direction (lower row) for low (left column), medium (middle column) and high (right column) final momenta of the trajectories. ( $R = 2 \text{ \AA}$ ,  $I = 1.5 \times 10^{14} \text{ W/cm}^2$ )

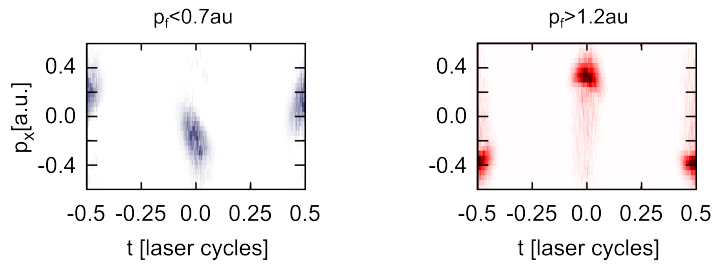


Figure III.3.10.: As Fig. III.3.9 but for  $R = 4 \text{ \AA}$ .

fast and slow trajectories, the birth-time,  $t_0$ , of slow, intermediate and fast trajectories is centred around the maxima of  $E_x$ . It is thereby noted parenthetically that especially for trajectories with low final momenta, a correlation between the initial momenta,  $p_x^0$  and  $p_y^0$ , and the time of birth,  $t_0$ , exists: for example,  $|p_x^0|$  increases from early to late ejection times, while  $p_y^0$  decreases for trajectories with low final momenta.

The analysis of the initial momenta and the birth time allows gaining an intuitive understanding for the observed dependence of  $\alpha$  on  $p_f$ : Tracing trajectories with low final momenta back in time to their time of birth (see III.3.9), shows that the  $x$ -component of the initial momentum of these trajectories points in the direction of the negative electric field,  $\mathbf{E}(t_0)$ , i.e. in the direction away from the nucleus and the  $y$ -component points in the direction of  $\mathbf{A}(t_0)$  and is thus anti-parallel to the final momentum  $\mathbf{p}_f^{\text{SFA}} = -\frac{1}{c}\mathbf{A}(t_0)$ , expected from SFA. Schematically, a trajectory as shown in blue in Fig. III.3.11 can thus be expected for the slow trajectories.

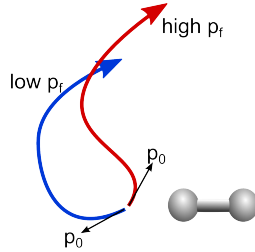


Figure III.3.11.: Schematic representation of a trajectory ending with high final momentum (red) and with low final momentum (blue). Black arrows indicate the initial momentum.

For the fast trajectories, the opposite is true: these trajectories preferentially start with  $\mathbf{p}_x^0$  parallel to  $\mathbf{E}(t_0)$  and  $\mathbf{p}_y^0$  anti-parallel to  $\mathbf{A}(t_0)$  as shown in red in Fig. III.3.11.

In both cases, the initial momentum component in  $y$ -direction mainly has the role of modulating the final momentum: While  $p_y^0$  is parallel to the momentum gained in the field for electrons with high  $p_f$ , it is anti-parallel for electrons with low  $p_f$ . The difference in rotation angle  $\alpha$  is due to the initial momentum in  $x$  direction: Trajectories with low final momentum, having an initial momentum in  $x$ -direction pointing away from the nuclei, rapidly leave the vicinity of the ion and hence only feel a weak Coulomb interaction, which explains the small deviation of  $\alpha$  from  $90^\circ$  of the slow trajectories. Trajectories with high final momentum, on the other hand, are ejected towards the nuclei, where they are subject to strong Coulombic forces, which results in a strong shift from the SFA predictions. Within the semi-classical model used in this work, the initial

momentum in  $x$ -direction,  $p_x^0$  thus plays an important role and the neglect of the latter would lead to results which do not follow the experimentally observed trend.

The semiclassical simulations leave, however, a certain ambiguity to the interpretation of the increasing rotation with increasing final momentum. The reason lies in the fact that the analysis depends so strongly on the initial values. As explained above, the initial value distribution used in the model does not necessarily correctly represent the quantum system. A different model, for example, in which the initial momentum  $p_x^0$  is set to zero, and the tunnel exit is restricted to the molecular axis, would also reproduce the experimentally observed trend. Using these restricted initial conditions, would lead to trajectories with low final momentum being preferentially born before the maximum of the field. Within the strong field approximation, trajectories born before the field maximum are rotated counterclockwise to angles lower than  $90^\circ$ . Together with the Coulomb attraction which leads to a clockwise shift, the birth of electrons with low final momenta before the field maximum would lead to a weakly or counterclockwise rotated PES, as observed in the experiment. This model is, however, less likely to capture the correct physics of the ionization process, since alignment dependent ionization rates from  $\text{H}_2^+$  show that ionization is preferred but not restricted to the molecular axis [130, 131].

Having discussed the influence of the initial values and the time of birth on the final momentum, we will now turn to analyzing the influence of the initial state description (field dressed vs. Floquet states) and multiple ionization bursts, Eq. (III.2.10). In Fig. III.3.12, a comparison of the angular distribution of the final PES for light induced versus Floquet states with and without multiple ionization bursts is shown for  $I = 1.5 \times 10^{14} \text{ W/cm}^2$  and  $R = 3 \text{ \AA}$ . The strong changes in the PES from Fig. a.) to b.) are due to the change

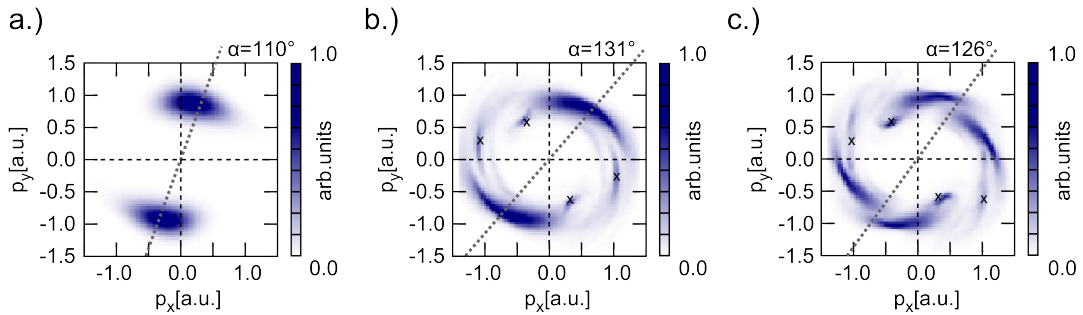


Figure III.3.12.: Photoelectron momentum spectrum obtained at  $I = 1.5 \times 10^{14} \text{ W/cm}^2$  and  $R = 3 \text{ \AA}$  for  $I_P$  defined via light induced potentials (a.), Floquet states (b. and c.); in a.) and b.) the ionization rate is ADK-like, in c.) the ionization rate mimics multiple ionization bursts, Eq. (III.2.10).

in  $I_P$  and the population  $\sigma_{l/r}$  of the left and right core. Furthermore, while for field induced potentials ionization proceeds via tunnelling at  $I = 1.5 \times 10^{14} \text{ W/cm}^2$ , due to the lower ionization potential of the Floquet states, in the latter case ionization proceeds over the barrier. This leads to the additional features marked with x in Fig. III.3.12: the corresponding final momenta are due to trajectories which, after being released into the classically allowed corridor, head back to the residual ion, cycle around one of the nuclei once and leave the molecule thereafter. Classically, this is easily possible in the over-the-barrier case, since there is no potential barrier hindering electrons with an initial momentum pointing towards the ion to fall back into the core region. If an initial momentum component pointing outwards from the ion is added to  $p_0$  or if  $p_0$  is randomly picked only in the hemisphere pointing in negative  $\mathbf{E}$ -direction, the components marked with  $x$  vanish (see Fig. III.3.13).

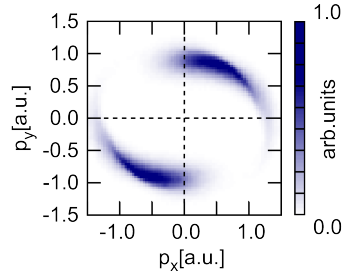


Figure III.3.13.: As Fig. III.3.12.b but rejecting trajectories with initial momentum  $\mathbf{p}_0 \cdot \mathbf{E}(t_0) > 0$ , i.e. rejecting electrons with initial momentum towards the ion. Note that the features marked with “x” in Fig. III.3.12 vanish.

When multiple ionization bursts are included, a clear double structure appears, where each peak in the PES corresponds to one ionization maximum. The angular distributions, shown in Fig. III.3.14, clearly show a broadening of the distribution due to the multiple ionization bursts. The mean angle,  $\alpha$ , however, does not depend strongly on whether multiple ionization bursts are considered or not. This can be understood, looking at Fig. III.3.14.d, where the Coulomb field is neglected in the propagation. Since the multiple ionization bursts obtained from Eq. (III.2.10) are symmetric around the field maximum, the two lobes to the left and to the right of the right of  $90^\circ$  have the same weight. The multiple ionization bursts thus do not lead to a rotation of the PES and  $\alpha = 90^\circ$  as expected in SFA. However, the change in ionization rate may well be responsible for the broadening of the PES observed experimentally.

The last panel in Fig. III.3.14 corresponds to a case in which an initial momentum  $\mathbf{p}_{\text{add}}$  added to  $\mathbf{p}_0$ . The kinetic energy due to the additional momentum was thereby set to

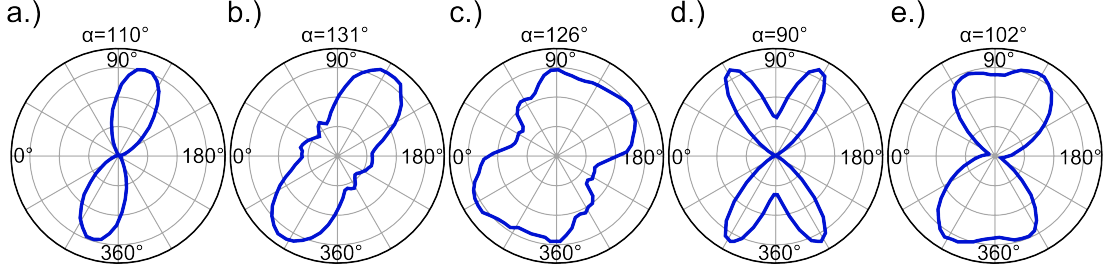


Figure III.3.14.: Comparison of models: angular photoelectron spectra for a.) light induced potentials + Delone-Krařnov rate, b.) Floquet states + Delone-Krařnov rate, c.) Floquet states + multiple ionization bursts, d.) as c.) but neglecting the Coulomb field in the propagation, e.) as c.) but with an additional initial momentum component as described in the text.

the over-the-barrier energy,  $\mathbf{p}_{\text{add}} = -\sqrt{2(-I_p - V_{\text{max}}(t_0))}\hat{\mathbf{E}}(t_0)$ , where  $V_{\text{max}}$  denotes the maximum of the combined nuclear and field potential in the corridor and  $\hat{\mathbf{E}}$  denotes the unit vector of the electric field at the time of birth. In this case, the mean rotation angle (depicted by a line in the graphs) is clearly shifted counter-clockwise, resulting in a rotation angle,  $\alpha$ , relatively close to  $90^\circ$ . In the experimental results by Spanner et al. [119], which are reproduced in Fig. III.3.8, a strong double lobe structure is apparent at high and intermediate momenta, with one lobe around  $\alpha \approx 90^\circ$  and the second lobe with a much larger rotation. The present results thus offer a possible explanation for the second lobe as being due to an outward directed flux of the electron density in the ionization process.

## III.4. Summary and Conclusion

In summary, the present work shows to what extent classical trajectory Monte Carlo calculations within the tunnelling picture can be used explain the experimental results for molecular strong-field ionization of  $\text{H}_2^+$  in circularly polarized fields. By including or neglecting the Coulomb forces in the propagation, the classical trajectory calculations provide a simple approach to test the influence of the anisotropic Coulomb potential on the final photoelectron momentum distribution. The model provides intuitive explana-



tions for the effects observed at increasing intensities and varying internuclear distances: the counterintuitive fact that the results do not tend towards the SFA-predictions for increasing intensity is explained via the interplay of two rivalling effects, the tunnel exit moving closer to the ion and the stronger electric field strength. The increasing rotation with increasing internuclear distance is explained via the change in  $I_P$  and hence the change of the location of the tunnel exit. The model also illustrates the importance of the initial momentum distribution of the classical trajectories in the analysis of the momentum-resolved angular PES. The possible influence of electronic dynamics prior to ionization is modelled via a modified ionization rate and modified initial momentum values. While the modification of the ionization rate broadens the distribution, an anisotropic initial momentum distribution rotates the PES.

In conclusion, many agreements between the semiclassical model and the experimental results could be shown and analysed. The results hence encourage studying molecular strong field ionization via classical trajectories. An extension to the present results would be the investigation of wavelength dependent effects and the influence of elliptical polarization. A classical description of over-the-barrier dynamics could possibly amend some of the difficulties in choosing the initial values for the trajectories in the over-the-barrier case.



## Part IV.

# Reaction control of $\text{C}_2\text{H}_2^{2+}$ via the carrier-envelope phase

“Man resorts to magic only where chance and circumstances are not fully controlled by knowledge.”

---

*(Bronislaw Malinowski; Culture (1931), 636.)*

## IV.1. Introduction

Efficiently controlling and steering molecular reactions is a long standing goal in chemistry and physics [132]. External perturbations allow influencing the molecular dynamics and thus gaining quantum control. Coherent control schemes, making use of weak, femtosecond laser pulses with a duration between 10s and 100s of fs to induce interferences in the molecular wavefunction, have been proposed since the late 1980s [133, 134, 135, 136] for reaction control. Experimental realization followed shortly after [41, 42]. The durations of these control pulses are on the same time-scale or longer than typical molecular vibrations. Therefore, these control schemes access the dynamics on the intrinsic timescales of the nuclear motion.

With the accessibility to few-cycle IR-pulses, with durations of less than 5 fs and a controlled carrier-envelope phase (CEP), the dynamics can be accessed on much shorter time scales. The control of the CE-phase, which directly determines the exact field shape on a sub-fs time scale, has been shown to significantly influence dissociative ionization of diatoms via the time dependence of the electronic dynamics, i.e. ionization and/or recollision [35, 36, 37, 38, 40, 45].

In 2012, our experimental collaboration partners, Dr. Xinhua Xie and Dr. Markus Kitzler from the Vienna University of Technology, applied CEP stabilized few-cycle IR pulses

to control fragmentation reactions of larger, polyatomic molecules. Using three different hydrocarbons as test systems, they demonstrated that changing the CE-phase can lead to a significant modulation of the observed fragmentation yield.

The present chapter is structured as follows: After a brief overview over the experimental results, the latter are analysed and interpreted theoretically. To this end, a short analysis of the properties of acetylene, the smallest of the molecules considered experimentally, provides the necessary primary knowledge to allow a theoretical investigation. Then, different scenarios that may induce the CEP dependence are discussed. Finally it is shown that the experiment can be explained via an energy threshold effect in recollisional ionization. The results of the combined experimental and theoretical investigations have been published in Physical Review Letters in 2012 and highlighted as Physics Viewpoint.

## IV.2. Experimental results

In their experiment [46], Dr. Xinhua Xie and Dr. Markus Kitzler investigated and proved the possibility to control the fragmentation reactions of acetylene ( $\text{C}_2\text{H}_2$ ), ethylene ( $\text{C}_2\text{H}_4$ ), and 1,3-butadiene ( $\text{C}_4\text{H}_6$ ) by tuning the CEP of few-cycle laser pulses.

Details on the experimental setup can be found in the supplementary material to Ref. [46], hence only a short description is given in the following: in an ultra-high vacuum chamber, linearly-polarized, sub-5fs IR-pulses are focused on a supersonic gas jet of unaligned molecules. The carrier-envelope phase of the pulses is measured on a shot-to-shot basis using the stereo-detection of high-energetic photoelectrons [7]. With peak intensities between  $1.1 \times 10^{14} \text{ W/cm}^2$  and  $3.0 \times 10^{14} \text{ W/cm}^2$ , the laser pulses are sufficiently strong to allow multiple ionization and subsequent fragmentation of the molecules. Fragments from the dicationic species are measured in coincidence using cold target recoil ion momentum spectroscopy. Since neutral particles cannot be detected directly, only reaction channels leading to two singly charged fragments are considered.

Figs. IV.2.1 to IV.2.3 show the measured channel resolved yields for acetylene, ethylene and butadiene at low intensities: while the yields of the cation and the dication are not or only weakly modulated by the CEP, the yields of the fragmentation channels exhibit

a strong dependence on the CEP, with modulation depths of up to  $\sim 70\%$ . Interestingly, all fragmentation channels show the same dependence on the CEP.

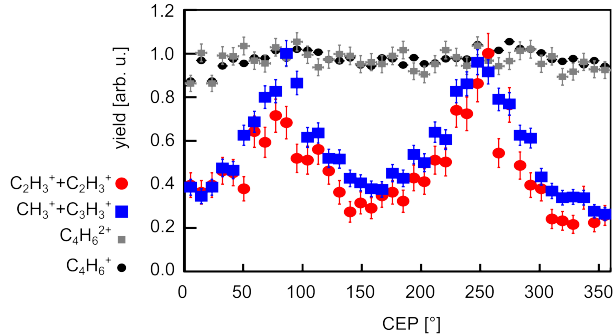


Figure IV.2.1.: Channel resolved yield for  $C_4H_6$  at  $1.1 \times 10^{14} \text{ W/cm}^2$  as a function of CEP.

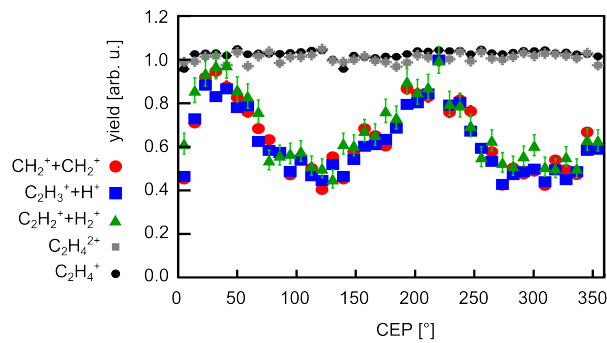


Figure IV.2.2.: Channel resolved yield for  $C_2H_4$  at  $1.5 \times 10^{14} \text{ W/cm}^2$  as a function of CEP.

When the intensity of the laser pulse is increased, the modulation depth decreases, as shown for the  $C_4H_6 \rightarrow CH_3^+ + C_3H_3^+$  channel in Fig. IV.2.4. In the case of acetylene, and ethylene (not shown) no CEP dependence can be observed at  $I = 3.0 \times 10^{14} \text{ W/cm}^2$ .

These results clearly demonstrate that controlling the CEP of the ionizing pulse allows predetermining the fragmentation and isomerization yield of small hydrocarbons. Fragmentation control is thus achievable on a sub-femtosecond time scale even for systems significantly larger than the diatoms studied before. This observation roused the question if the mechanism leading to this control is still the same as in the much smaller systems investigated previously. To answer this question a detailed theoretical analysis was necessary. For this analysis, acetylene was chosen as model system since it is the

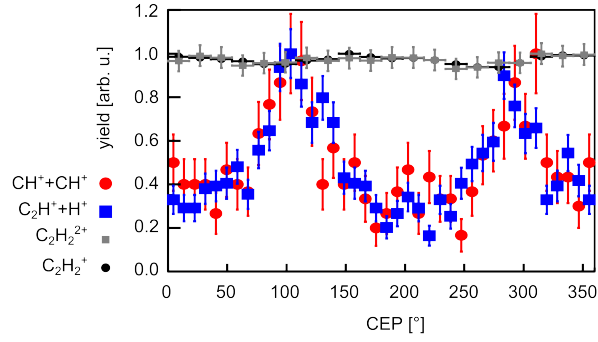


Figure IV.2.3.: Channel resolved yield for  $C_2H_2$  at  $1.5 \times 10^{14} \text{ W/cm}^2$  as a function of CEP.

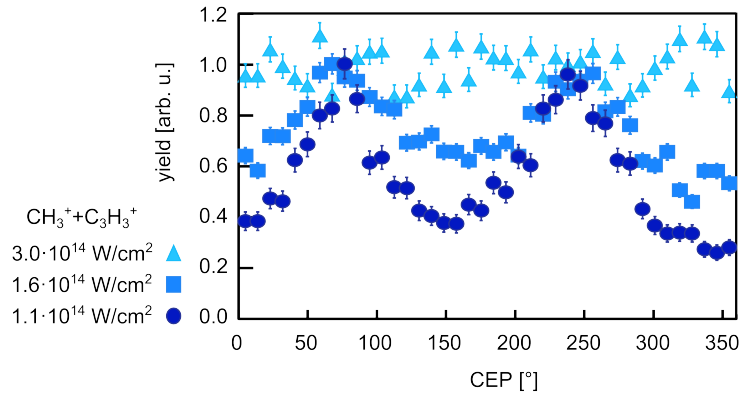


Figure IV.2.4.: Yield of the  $C_4H_6 \rightarrow CH_3^+ + C_3H_3^+$  channel as a function of CEP for increasing intensity.

smallest of the systems and can thus be treated more easily in theoretical calculations than the even larger molecules, ethylene and butadien.

## IV.3. Potential landscape of acetylene and its cations

Due to the complexity of molecular systems, preliminary knowledge on the energy structure is necessary to reduce the possible reaction pathways considered. In the following, the most important features of the potential landscape of acetylene are presented. The neutral species, the cation, and, most importantly, the dication for which the fragmentation reactions were studied, are considered.

### IV.3.1. The neutral species

In its neutral ground state, acetylene has a linear equilibrium geometry. The experimentally determined equilibrium bond lengths are C-C  $\approx 1.20$  Å and C-H  $\approx 1.06$  Å (see Fig. IV.3.1) [137]. Using the symmetry labels of the  $D_{\infty h}$  point group, to which the

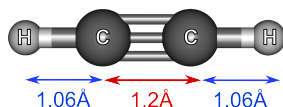


Figure IV.3.1.: Equilibrium geometry of neutral acetylene [137].

equilibrium geometry corresponds, the Hartree-Fock configuration for the  $^1\Sigma_g^+$  ground state of acetylene is given by  $1\sigma_g^2, 1\sigma_u^2, 2\sigma_g^2, 2\sigma_u^2, 3\sigma_g^2, 1\pi_u^4$ . The highest occupied orbitals are thus bonding  $\pi_u$ -orbitals, i.e. the bonding linear combination of a  $2p$  orbital lying orthogonal to the molecular axis from each carbon atom. The next lower lying orbital is a bonding  $\sigma_g$  orbital resulting from a linear combination of the hydrogen  $1s$  orbitals and the carbon  $2s$  and  $2p_z$  orbitals. Most excited states of  $C_2H_2$  are considerably stabilized either by cis- or by trans-bending [138] leading to a preference of non-linear geometries. The vertical excitation energy to the first excited state lies slightly above 4.5 eV [138].

### IV.3.2. The cation

The cationic  ${}^2\Pi_u$  ground state has a linear equilibrium geometry. The equilibrium bond lengths are similar to, but slightly longer than, those of the neutral (C-C  $\approx 1.24$  Å and C-H  $\approx 1.08$  Å) [139]. The ionization energy is 11.4 eV [140]. An excellent overview over the ionic ground and excited states and their potential curves, most of which are stabilized either for trans- or cis- bending, is given in Refs. [141, 142].

### IV.3.3. The dication

Since, in the experiment, fragmentation reactions of the dication were considered, the dicationic electronic states will be the most important for the present analysis. The vertical double ionization potentials for several dicationic singlet and triplet states are reported in Ref. [143]. Thiessen et al. [144] provide schematic potential energy surfaces for the lowest lying dicationic states along the C-C and the C-H stretching mode.

To allow a detailed analysis, SA-CAS and MRCI calculations were performed in the course of this work. Table IV.3.1 gives an overview over the calculated vertical excitation energies to the lowest lying dicationic states.

State	SA-CAS calculations		MRCI calculations	comparison with Ref. [143]	
	$\Delta E$ from neutr. ${}^1\Sigma_g^+$	$\Delta E$ to ${}^3\Sigma_g^-$	$\Delta E$ to ${}^3\Sigma_g^-$	$\Delta E$ from neutr. ${}^1\Sigma_g^+$	$\Delta E$ to ${}^3\Sigma_g^-$
${}^3\Sigma_g^-$	30.9			31.4	
${}^1\Delta_g$	31.8	0.9	1.0	32.5	1.1
${}^1\Sigma_g^+$	32.3	1.6	1.7	33.2	1.9
${}^3\Pi_u$	36.4	5.5	5.8	36.8	5.4
${}^1\Pi_u$	37.2	6.3	6.7	37.6	6.3
${}^3\Pi_g$	37.7	6.9	7.3	38.2	6.8

Table IV.3.1.: Vertical excitation energies from the neutral ground state to the lowest lying dicationic states and vertical excitation energies relative to the dicationic ground-state. SA-CAS: 2 frozen and 10 active orbitals, all valence electrons active, aug-cc-pVTZ basis, no symmetry used; MRCI: SA-CAS(8,11)+MRCI(8,9), aug-cc-pVDZ basis,  $C_{2v}$  symmetry.

Figs. IV.3.3 and IV.3.4 show cuts through the potential landscape and the resulting fragmentation products along the C-H and the C-C stretching modes. The calculations



were performed in the  $C_{2v}$  subgroup of  $D_{\infty h}$  (C-C stretching mode) and  $C_{\infty v}$  (C-H stretching mode) and the state average was performed over all states of one symmetry element of  $C_{2v}$ . (The relation of symmetry elements of the different point groups is shown in Fig. IV.3.2.) Due to the smaller CAS space used to calculate the potential curves compared to the space used to calculate the vertical excitation energies in Tab. IV.3.1, the vertical excitation energies are slightly shifted compared to the values given in Tab. IV.3.1.

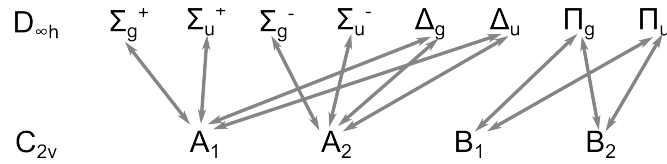


Figure IV.3.2.: Correspondence of symmetry elements in  $C_{2v}$  and  $D_{\infty h}$ .

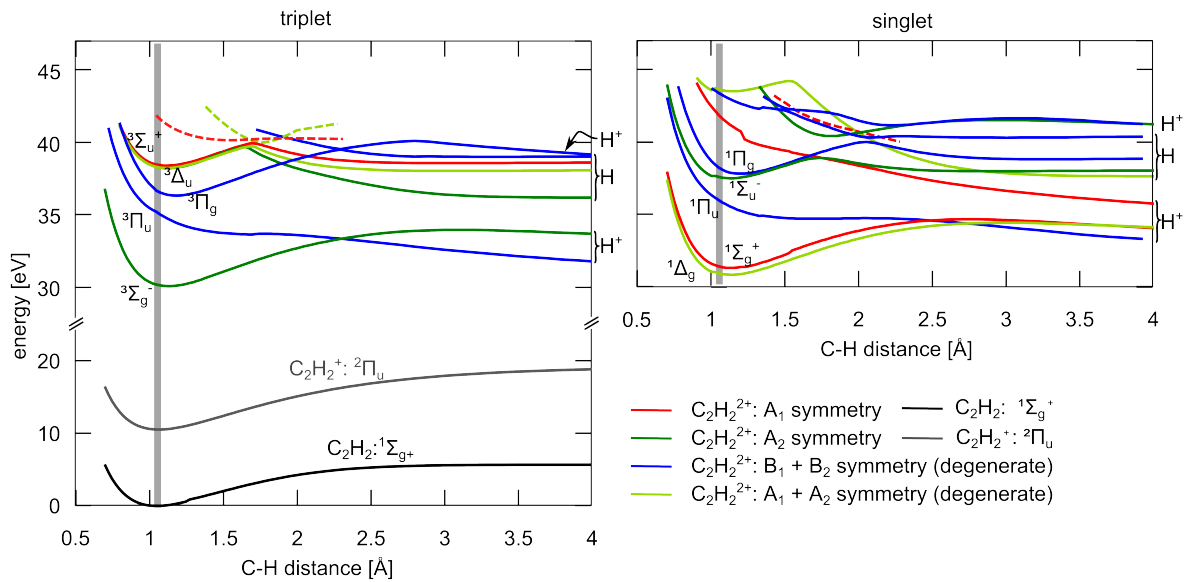


Figure IV.3.3.: The C-H stretching mode of acetylene calculated by SA-CAS(9,8) or SA-CAS(10,8) for the dicationic states and CAS(8,8) else. Basis set: aug-cc-pVTZ. C-C = 1.2 Å, other C-H = 1.06 Å. The nomenclature of states follows the nomenclature in the linear, symmetric groundstate geometry. The symbols  $H^+$  and  $H$  at the right hand side of the panels denote dissociation into  $C_2H^+ + H^+$  and  $C_2H_2^+ + H$ . The gray bar indicates the Franck-Condon region and thus the vertical excitation energies.

Figs. IV.3.3 and IV.3.4 show that the dicationic groundstate and the first two singlet states are metastable. Lifetimes up to more than 1  $\mu$ s have been suggested in Ref. [144] for

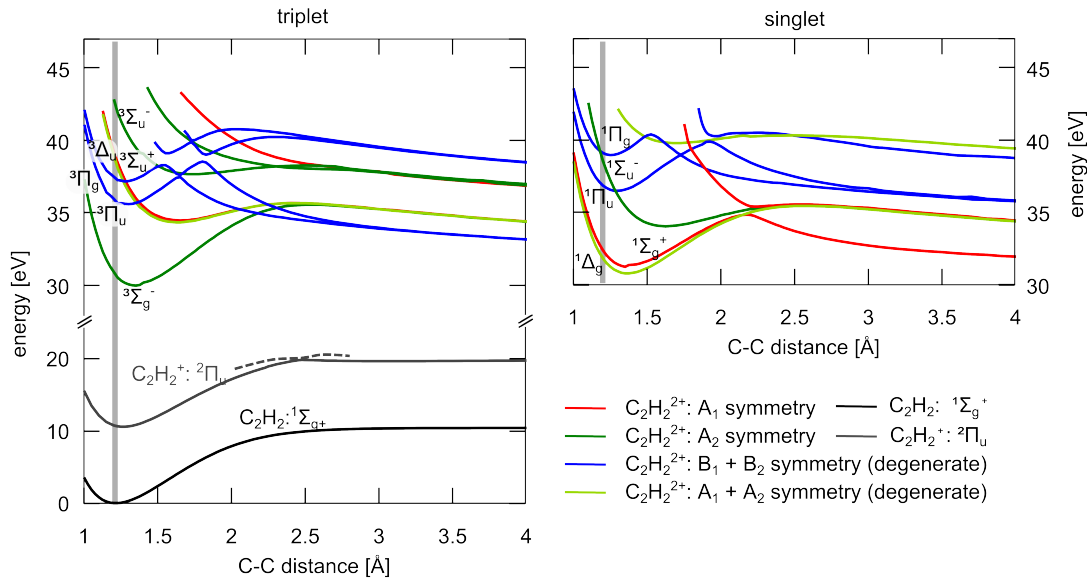


Figure IV.3.4.: As Fig. IV.3.3 for the C-C stretching mode (SA-CAS(8,8), C-H = 1.06 Å). Dotted lines denote states that were not followed throughout the entire region.

$C_2H_2^{2+}$ . Dynamics calculations in reduced dimensions, for the C-H stretching mode only, performed on the  $^3\Sigma_g^-$ - and  $^1\Delta_g$ -states, show that the vibrational frequency for the C-H stretching mode is around 13 fs. Since the C-H stretching mode is the fastest vibrational mode, this shows that vibrational dynamics in acetylene proceeds on timescales longer than the 4.5 fs duration of the laser pulse used in the experiment.

The next higher states, the  $^3\Pi_u$  and  $^1\Pi_u$  states have vertical excitation energies relative to the  $^3\Sigma_g^-$  state of 5.5 eV and 6.3 eV, respectively (see Tab. IV.3.1). These states are strongly dissociative along the C-H stretching mode, as can be seen in Fig. IV.3.3. From a Mulliken charge analysis, one can conclude that the  $\Pi_u$  states dissociate into  $C_2H^+ + H^+$ , and not into the  $C_2H_2^{2+} + H$  channel. (The latter channel corresponds to the dissociation limit of several of the higher excited states.)

Along the C-C stretching mode (Fig. IV.3.4), the  $^3\Pi_u$  and the  $^1\Pi_u$  state both show a potential barrier to dissociation. For a linear, symmetric geometry at C-H distances of 1.06 Å, the barrier height is approximately 2.5 eV for the  $^3\Pi_u$  state. For the singlet state, the barrier is even higher. Due to the high barrier, one might expect the  $\Pi_u$  states not to dissociate along the C-C bond. A more detailed investigation, however, shows that this is not true: For linear, symmetric geometries, the  $^3\Pi_u$  state has a symmetry allowed conical intersection (CI) with the  $^3\Pi_g$  state. At asymmetric or non-linear geometries, the

two states fall into the same symmetry group and the CI can open to an avoided crossing as shown in Fig. IV.3.5. This effectively reduces the barrier height for non-symmetric, or non-linear geometries.

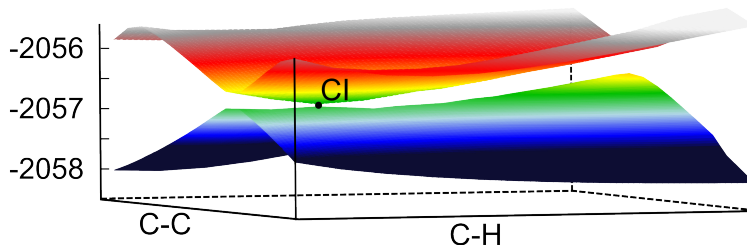


Figure IV.3.5.: Level crossing of the 1st and 2nd excited triplet states ( ${}^3\Pi_u$  and  ${}^3\Pi_g$ ) of  $C_2H_2^{2+}$ .

To confirm this argument, reduced dimensional quantum dynamics calculations were performed along the C-C stretching mode for linear, asymmetric geometries with C-H distances of 1.15 Å and 1.9 Å. The smaller bond distance thereby approximately corresponds to the equilibrium bond length of the dicationic groundstate [144]. The four lowest potential surfaces corresponding to states with  $B_1$  and  $B_2$  symmetry in  $C_{2v}$  ( $\Pi_u$  and  $\Pi_g$  in  $D_{\infty h}$ ) were calculated using the aug-cc-pVDZ basis, a CAS(8,8) with a state-average over the three lowest lying  $B_1$  and  $B_2$  states and a subsequent MRCI(8,9) for the four lowest  $B_1$  states. In the MRCI calculation, states of  $B_1$  and  $B_2$  symmetry were allowed as reference to account for the fact that the  $B_1$  and  $B_2$  states are degenerate for linear geometries. Additionally, the nonadiabatic couplings were calculated analytically using the COLUMBUS software package [84]. The states were diabaticized along the C-C stretching coordinate, using the diabaticization scheme described in Ref. [145].

Figure IV.3.6 shows the resulting adiabatic energies of the  $B_1$  states (lower panel) and their non-adiabatic couplings (upper panel) along the C-C stretching mode. The avoided crossing between the ground and first excited state is clearly visible and accompanied by a large nonadiabatic coupling. Fig. IV.3.7 shows the diabatic states<sup>1</sup>. In the diabatic picture, the groundstate (red line) crosses the excited states and is thus strongly bound.

To find out whether acetylene may dissociate along the C-C stretching mode in spite of the rather high barrier at linear, symmetric geometries, a field-free dynamics calculation was performed on the afore calculated diabatic potentials. Mimicking a Franck-Condon

<sup>1</sup>Unfortunately, it was not possible to calculate sufficiently many states to have only weak coupling to the next higher states. A strict diabaticization was thus not possible.

excitation to the dicationic  ${}^3\Pi_u$  state, a nuclear wavefunction corresponding approximately to the lowest vibrational state of the electronic ground-state of  $\text{C}_2\text{H}_2$ , was set to the lowest of the states ( ${}^3\Pi_u$ ) and propagated. Possible deviations from the Franck-Condon principle due to an  $R$ -dependent ionization potential, as observed in Ref. [146] for tunnel ionization from  $\text{H}_2$ , were not taken into account: in the case of acetylene, the potential surfaces of the neutral and the ion near the equilibrium geometry are similar (see Fig. IV.3.4 and Fig. IV.3.3) and the second ionization step may proceed via recollisional ionization. A Franck-Condon like ionization behaviour may thus be expected in this case.

The result of the propagation is shown in Fig. IV.3.8, for the lowest diabatic state  $V_1$  (left) and the excited diabatic state  $V_3$  shown in blue in Fig. IV.3.7 (right): At the beginning of the propagation, the nuclear wavefunction moves mainly on the ground state. Around  $t = 10$  fs the wavepacket reaches the classical turning point and a very small portion (barely visible in the left panel of Fig. IV.3.8) of the wavefunction leaves the potential barrier. Near the turning point (C-C  $\approx 1.7$  Å), the groundstate crosses the first excited state and population is transferred to the latter, unbound state, leading to a significant amount of fragmentation. The subsequent dynamics become very complicated due to the couplings to the other excited states. Overall, due to the significant amount of density dissociating from the  $V_3$  potential after the nonadiabatic transition, the  ${}^3\Pi_u$  state can be expected to allow fragmentation into  $\text{CH}^+ + \text{CH}^+$  as well as  $\text{C}_2\text{H}^+ + \text{H}^+$ . This fact will be used in the analysis of the experiment in the next section.

## IV.4. Discussion of possible fragmentation scenarios

Using the potential energy structure of acetylene presented in the last chapter, we can now discuss possible scenarios and physical processes that may lead to the strong CEP dependence of the yield of  $\text{CH}^+ + \text{CH}^+$  and  $\text{C}_2\text{H}^+ + \text{H}^+$  observed in the experiment.

As discussed in the last chapter, the dicationic  ${}^3\Sigma_g^-$  groundstate, the  ${}^1\Delta_g$  and the  ${}^1\Sigma_g^+$  state are metastable. Dissociation thus most probably occurs on a higher excited po-

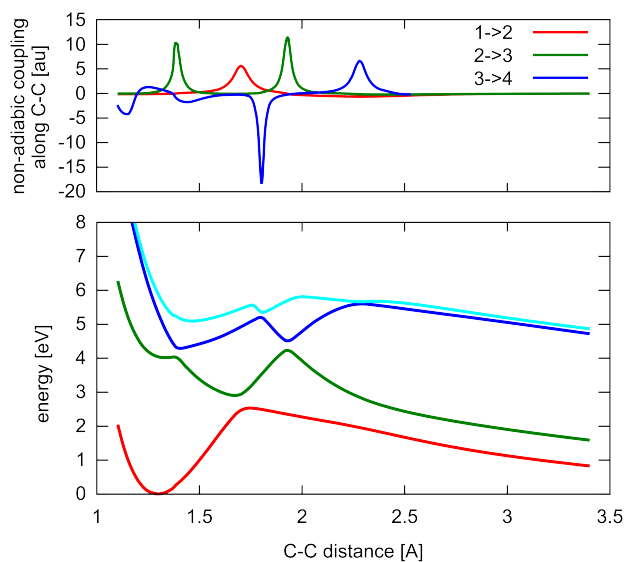


Figure IV.3.6.: Lower panel: four lowest adiabatic states with  $B_1$  symmetry for linear geometry and C-H distances of 1.15 Å and 1.9 Å; upper panel: non-adiabatic coupling elements for neighbouring states.

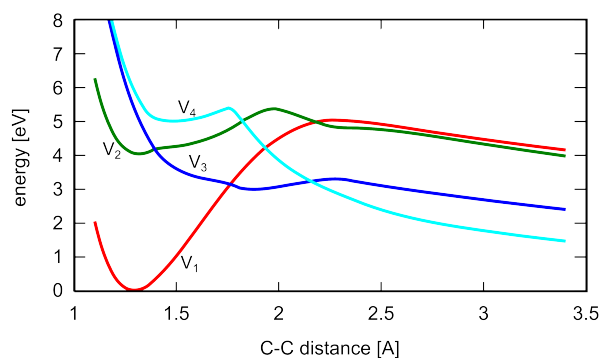


Figure IV.3.7.: Diagonal elements of the diabatic potential matrix resulting from the states and nonadiabatic couplings shown in Fig. IV.3.6

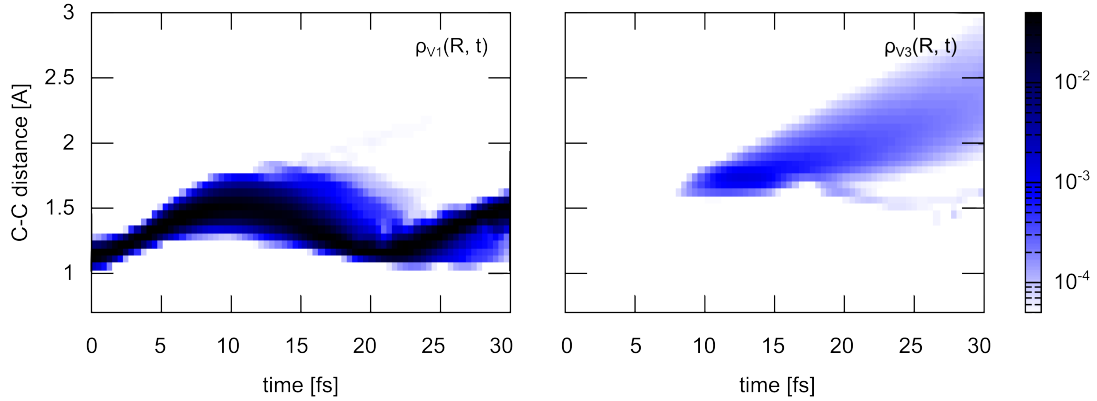


Figure IV.3.8.: Wavepacket dynamics: Left panel: density in the diabatic ground state  $V_1$ ; right panel: density in the diabatic excited state  $V_3$  shown in dark blue in Fig. IV.3.7.

tential energy surface, such as the  ${}^3\Pi_u$  state, that was shown in the last section to allow fragmentation into both, the  $\text{CH}^+ + \text{CH}^+$  and the  $\text{C}_2\text{H}^+ + \text{H}^+$  channel.

Figure IV.4.1 shows a sketch of the main interaction processes between the laser field and the molecule: ionization may occur via a sequential or via a non-sequential process. Excitation may be induced by the recollision of an electron, or by field excitation processes, i.e. dipole coupling of the electronic states.

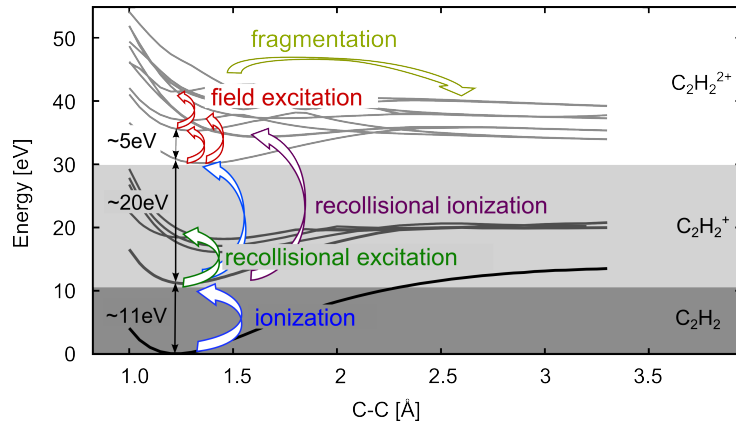


Figure IV.4.1.: Selected potential energy surfaces of  $\text{C}_2\text{H}_2$ ,  $\text{C}_2\text{H}_2^+$  and  $\text{C}_2\text{H}_2^{2+}$ ; vertical excitation energies; and relevant field driven processes.

In previous work on the CEP-control of dissociative ionization of  $\text{D}_2^+$  and  $\text{H}_2^+$  [35, 36, 48, 49], field driven population transfer via dipole coupling was shown to be a main process leading to the CEP control over molecular dynamics. Field excitation processes to the  ${}^3\Pi_u$  state will therefore be discussed in section IV.5.

Another process that may be CEP dependent, is the (double) ionization probability. According to the tunnelling picture (I.2.5), the ionization probability depends exponentially on the field strength. Since the temporal evolution of the laser field depends on the CEP, the probability for sequential ionization may be expected show a CEP dependence. However, as argued in the following, sequential ionization can be expected to play a minor role compared to recollision processes at the experimental parameters considered.

According to Ref. [147], for 50 fs-pulses, non-sequential ionization becomes important for laser intensities around and below  $3 \times 10^{14} \text{ W/cm}^2$ . The experimentally relevant intensities ( $I \approx 1.5 \times 10^{14} \text{ W/cm}^2$ ) are considerably smaller than this threshold. Additionally, recollisional ionization should scale approximately linearly with the pulse duration, whereas sequential double ionization should scale approximately with the pulse duration squared. This is due to the fact that for sequential ionization, the probability to release the first and the second electron both scale with the pulse length, whereas the recollision probability is relatively independent on the pulse length since the highest energetic electrons recollide after less than one laser cycle and later laser cycles are irrelevant. For the low intensities and very short pulses at which the experiment was performed, recollision induced, non-sequential ionization may thus be expected to be dominant. This is also backed up by the experimentally measured mean momentum of the ions and fragments in laser polarization direction shown in Fig. IV.4.2: the mean momentum as a function of CEP for the  $C_2H_2^{2+}$  ion, as well as the fragmentation channels show a strong oscillation, which is out of phase with the much weaker oscillation for the  $C_2H_2^+$  ion, suggesting a different ionization mechanism for the dications compared to the cation.

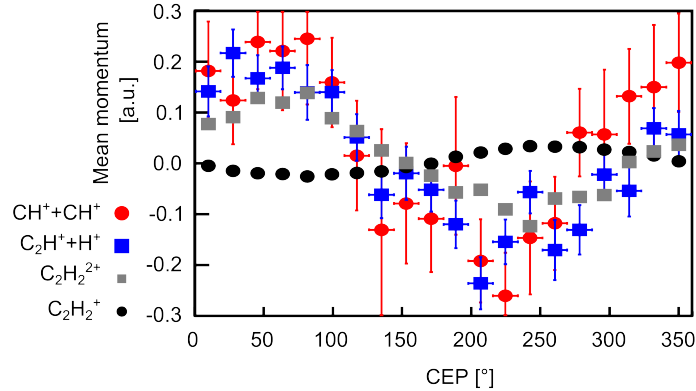


Figure IV.4.2.: Mean ion momentum for  $C_2H_2^+$  (black dots),  $C_2H_2^{2+}$  (gray squares) and the dicationic fragmentation channels (red dots and blue squares).

## IV.5. CEP dependence of field excitation processes

Although field excitation processes via dipole coupling of electronic states have been shown to be important for the CEP dependent charge localization in diatoms, several reasons suggest that in the case of acetylene, field excitation is not relevant: at equilibrium geometry, the dissociative excited states are separated from the ground state by several eV (see Figs. IV.3.4 and IV.3.3), significantly higher than the average photon energy of 1.5 eV. Field excitation can thus be expected to be very weak near the equilibrium geometry and to become relevant only when the molecule has rearranged to a geometry at which the level spacing is significantly reduced. Due to the difference in the fragment's reduced masses  $\mu$  ( $\frac{\mu_{\text{C-C}}}{\mu_{\text{C-H}}} \approx 6.8$ ), the molecular dynamics of the C-C and the C-H vibration take place on considerably different timescales. If field excitation plays the dominant role, one would therefore expect the CEP dependence of the yield to differ for the two fragmentation channels: Due to the faster vibration along the C-H stretching mode, a strong CEP dependence would be expected for the  $\text{C}_2\text{H}^+ + \text{H}^+$  channel, whereas a weak or no CEP dependence would be expected for the  $\text{CH}^+ + \text{CH}^+$  channel. Experimentally, however, a very similar behaviour is found for all fragmentation channels as a function of CEP.

As a further check for the relevance of field excitation, reduced dimensional quantum dynamics calculations were performed. Considering only the fastest modes (i.e. the two C-H stretching modes) and the four strongest dipole coupled triplet states ( $^3\Sigma_g^-$ ,  $^3\Pi_u$ ,  $^3\Pi_g$  and a  $^3\Sigma_u$  state), an initial wavepacket, corresponding to the nuclear wavepacket of the neutral groundstate, thus mimicking a Franck-Condon transition, was set to the  $^3\Sigma_g$  state and propagated in the field<sup>1</sup>. However, since the equilibrium C-H bond distance of the dication and the neutral are similar, mainly low vibrational states are populated and very little density reaches large internuclear distances where the energy spacing is small. As a result, the probability for field excitation remains very low, independently

---

<sup>1</sup>More details on the dynamics calculation are given in Chapter V.5



of the moment of ionization, the alignment and the carrier-envelope phase. The largest field excitation induced fragmentation probability was found for parallel alignment and a CEP of  $\phi_{\text{CEP}} = 90$  degree (sine pulse) with slightly above 0.3 %. Due to this very small excitation probability, it seems unlikely that field excitation can compete with the direct population of excited states via recollisional ionization.

## IV.6. CEP dependence of recollisional ionization

Depending on the energy of the recolliding electron, recollision may lead to impact excitation or ionization of the remaining ion. According to the strong field approximation, the maximum recollision energy in a continuous wave laser is given by Eq. (I.2.10):  $\varepsilon_{\text{rec.}}^{\text{max}} = 3.17U_P$ . For a peak intensity of  $I = 1.5 \times 10^{14}$  W/cm<sup>2</sup> and a wavelength of 800 nm, this corresponds to a recollision energy of  $\varepsilon = 28$  eV, considerably above the ionization potential from the ionic to the dicationic groundstate of about 20 eV (see Fig. IV.4.1, [143]). Recolliding electrons can therefore directly ionize the molecule.

Additionally, double ionization could be obtained by recollision and subsequent field ionization. Although the electron impact excitation cross-section at 30 eV is more than a factor 5 larger than the cross-section for electron impact ionization ( $p_{\text{rec. exc}} = 5p_{\text{rec. ioniz}}$ ) [148, 149], recollisional ionization can be expected to be more important for fragmentation from the dication: the probability for a subsequent ionization step after an excitation would have to be larger than  $\frac{1}{5}$  in order to dominate over recollisional ionization ( $p_{\text{rec. exc.}} \cdot p_{\text{field ioniz.}} \approx p_{\text{rec. ioniz.}}$ ). It is thus likely, that recollisional excitation with subsequent ionization cannot compete with recollisional ionization, as long as the recollision energy is sufficient to overcome the ionization potential.

To directly allow the fragmentation of the molecule via recollisional ionization, however, an excited state of the molecule has to be populated by the electron impact. With an ionization potential,  $I_P = E(^3\Sigma_u) - E(^2\Pi_u)$  around 25 eV (compare table IV.3.1, taking into account the ionization energy to the cation of 11.4 eV), the energy necessary to

reach the first dissociative state ( ${}^3\Pi_u$ ) is very close to the estimated maximum recollision energy of  $\varepsilon = 28$  eV.

In a short pulse, the exact value of the maximum recollision energy depends on the carrier-envelope phase as shown in Fig. IV.6.1. Therefore, if the ionization potential of

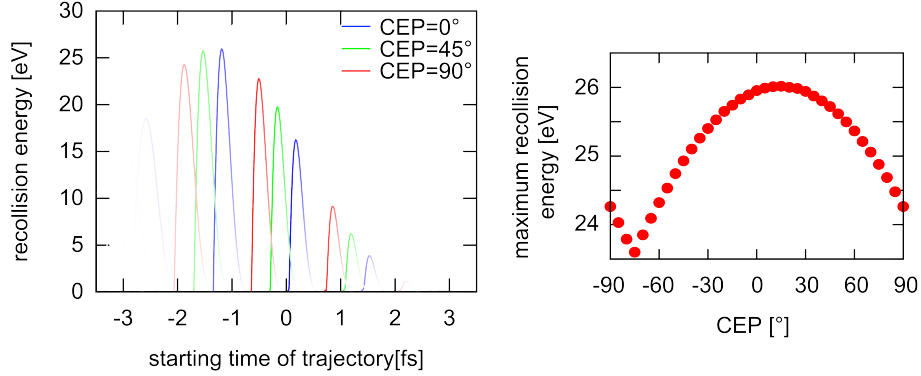


Figure IV.6.1.: Recollision energy in SFA approximation. Left panel: recollision energy as a function of release time  $t_0$  of the electron, the color intensity is scaled with the laser field strength at  $t_0$ ; right panel: maximum recollision energy as a function of CEP. Laser parameters:  $\sin^2$  envelope, full-width at half-maximum 4.5 fs, intensity  $1.5 \times 10^{14}$  W/cm<sup>2</sup>

a specific excited state is close to the threshold above which electron impact ionization is energetically forbidden, the population of this state will crucially depend on the exact recollision energy of the electron and hence on the carrier-envelope phase. To underpin this argument, the recollision process was modelled within a quasi-1D semi-classical approximation.

### IV.6.1. Description of the model

The model is based on the three-step model [21] and involves (1) the ionization from the neutral, (2) the classical propagation of the electron and (3) the probability to populate a dissociative state. The focus lies on possible CEP dependencies. The model was restricted to a single dimension parallel to the laser polarization direction.

The initial ionization step is described via the ADK-rate [56]

$$\Gamma(t) = f(n, l, m, I_P) \left( \frac{2(2I_P)^{\frac{3}{2}}}{|E(t)|} \right)^{2n-|m|-1} e^{-\frac{2(2I_P)^{\frac{3}{2}}}{|E(t)|}}, \quad (\text{IV.6.1})$$

where  $I_P$ , the ionization potential from the neutral to the ion, is set to 11.4 eV and the electric field  $\mathbf{E}(t) = -\frac{1}{c} \frac{\partial \mathbf{A}(t)}{\partial t}$  is defined via

$$A(t) = \begin{cases} A_0 \cdot \cos^2\left(\frac{\pi}{T}t\right) \sin(\omega t + \phi_{CE}) & -\frac{T}{2} < t < \frac{T}{2} \\ 0 & \text{else,} \end{cases} \quad (\text{IV.6.2})$$

where  $T$  is the total pulse length. The variable  $n$  is given by  $n = \frac{1}{\sqrt{2I_P}}$  and the angular momentum quantum numbers were set to  $l = m = 1$ , as suggested in Ref. [26] for the ionization from  $\pi$ -bonds. The function  $f$  depends only on  $n$ ,  $l$ ,  $m$ , and  $I_P$  and is therefore constant for all CE phases and was neglected. The ADK-rate only provides an approximation to the exact ionization rate, since it does not correctly account for the molecular structure and the fact that ionization at the parameters under investigation lies in the classical over-the barrier regime (assuming a single center potential, the classical over the barrier regime is reached for  $I_P = 2\sqrt{E} \approx 14$  eV for an intensity of  $1.5 \times 10^{14}$  W/cm<sup>2</sup>). Furthermore the Keldysh parameter  $\gamma \approx 1$ . However, since we are only interested in the relative changes of the ionization rate due to the change in CEP, in a first approximation, this should not greatly influence the results.

At the moment  $t = t_0$  of ionization, a classical electron trajectory is started at a distance of  $x_0 = I_P/E(t_0)$  from the molecular center. This corresponds to the approximate tunnel exit in a spherical potential. For the initial momentum, an average is taken over the initial velocity distribution  $w(p_{\parallel})$  parallel to the electric field

$$w(p_{\parallel}(t_0)) = e^{-\frac{p_{\parallel}^2 \omega^2 \sqrt{2I_P}^3}{3E(t_0)^3}}, \quad (\text{IV.6.3})$$

as given in Eq. (I.2.5). The frequency  $\omega = 0.057$  au describes 800 nm radiation. It was found, however, that neglecting the parallel velocity distribution does not change the results considerably.

The momentum distribution orthogonal to the laser polarization axis, leading to an effective wavepacket spread, was taken into account in the one-dimensional model by scaling the recollision probability with the inverse area  $A$  covered by the wavefunction at the time  $t$  of recollision. This area  $A(t, t_0)$  was assumed to be given by

$$A(t, t_0) = \pi \sigma_{p\perp}^2 (t - t_0)^2, \quad (\text{IV.6.4})$$

where  $t_0$  is the start time of the trajectory and  $\sigma_{p\perp}$ , the standard deviation of the electron momentum in direction perpendicular to the laser polarization direction, is

given in Eq. (I.2.5).

The electron is then propagated classically in the laser field and a soft core Coulomb potential  $V(x) = \frac{1}{\sqrt{1+x^2}}$ , by solving Newton's equations of motion. The electron is defined to recollide with the molecule at time  $t_{\text{rec}}$ , if it returns to its "birthplace"  $x_0$ , i.e. if  $x(t_{\text{rec}}) = x_0$ . As the probability for later recollisions is strongly overestimated in 1D models, only the first recollision event is taken into account.

Assuming that an electron trajectory starting at  $t = t_0$  recollides with the molecule at  $t = t_{\text{rec}}$ , the next step is to describe the probability for recollisional ionization and subsequent fragmentation. While experimental data for the electron impact ionization cross-section of acetylene can be found in the literature (e.g. [150, 148, 149, 151]), no state selective cross-sections are available and the energy resolution near the threshold is low. Therefore, the energy dependent electron impact ionization cross-section  $\sigma$  was described by the equation by Gryzinski [152, 153].

$$\sigma(E_e(t_{\text{rec}})) \propto \frac{I_P^{\text{ion.}}}{E_e} \left( \frac{E_e - I_P^{\text{ion.}}}{E_e + I_P^{\text{dissoc.}}} \right)^{\frac{3}{2}} \left[ 1 + \frac{2}{3} \left( 1 - \frac{I_P^{\text{ion.}}}{2E_e} \right) \ln \left( 2.7 + \sqrt{\frac{E_e}{I_P^{\text{ion.}}} - 1} \right) \right], \quad (\text{IV.6.5})$$

where  $E_e$  is the electron impact energy given  $E_e = \frac{p_{\parallel}(t_0, t_{\text{rec}})^2}{2}$ . The ionization potential  $I_P^{\text{ion}}$  denotes the energy gap between the ionic state and the dicationic state populated via recollisional ionization. Since we are interested in the fragmentation of the molecule,  $I_P^{\text{ion}}$  was set to 25 eV, corresponding approximately to the ionization potential to the  ${}^3\Pi_u$  state, which was identified as the lowest lying, strongly dissociative potential. If the recollision energy  $E_e$  is smaller than  $I_P^{\text{ion}}$ , ionization is energetically forbidden, and the cross-section  $\sigma$  is zero.

The probability  $P_{\text{dissoc.}}$  for dissociative ionization, i.e. to fragment, was then set to

$$P_{\text{dissoc.}} \propto \Gamma(t_0) \sigma(E_e(t_{\text{rec}})) / A(t_{\text{rec}}, t_0), \quad (\text{IV.6.6})$$

and a weighted average was taken for the initial momentum distribution parallel to the field. Arbitrary scaling factors were neglected since only relative changes are of interest.

## IV.6.2. Results and Discussion

Fig. IV.6.2 shows the resulting fragmentation probability as a function of laser intensity and CEP for a  $\sin^2$  pulse with a full-width at half maximum (of the intensity) of 4.5 fs

(see Eq. IV.6.2). A modulation of the fragmentation probability with CEP is clearly

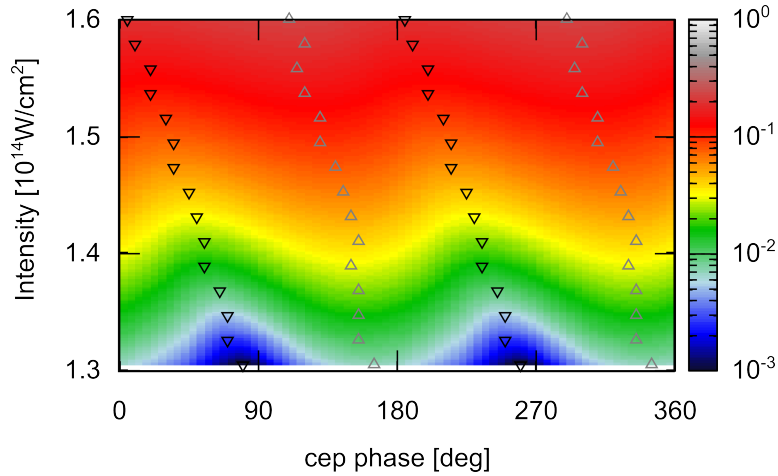


Figure IV.6.2.: Predicted fragmentation yield as a function of CEP and intensity for a  $\sin^2$  shaped laser pulse with a full-width at half maximum of 4.5 fs. Downward triangles: location of minima; upward triangles: location of maxima.

visible especially for low intensities. To guide the eye, down and up triangles show the position of the minima and maxima, which shift to smaller angles for increasing field intensities.

The overall probability for dissociative ionization strongly increases with increasing laser intensity. This is due to a.) the increasing probability for tunnel ionization, b.) the increasing probability to have electrons recolliding with sufficient energy to ionize and c.) the increasing electron impact ionization cross-section for energies up to 100 eV [149]. For even lower intensities (not shown), fragmentation is forbidden independently of CEP.

The ratio between the minima and the maxima is shown in Fig. IV.6.3 as a function of intensity. While the modulation depth is nearly 100% up to  $I = 1.28 \times 10^{14} \text{ W/cm}^2$ , the modulation depth quickly decreases with increasing intensity and reaches  $\sim 70\%$  around  $I \approx 1.35 \times 10^{14} \text{ W/cm}^2$ . At  $I = 2.5 \times 10^{14} \text{ W/cm}^2$ , the modulation depth is only around 4%.

The predicted CEP dependence of the fragmentation yield is shown for  $I = 1.35 \times 10^{14} \text{ W/cm}^2$  in Fig. IV.6.4 in comparison with the experimentally measured yield of  $C_2H^+ + H^+$  and  $CH^+ + CH^+$ . Up to a shift of approximately  $50^\circ$  in CEP, the model predictions reproduce the measured yields very well. The agreement is obtained directly from the model and not via a fit to the experimental data. The only parameters that entered the model are

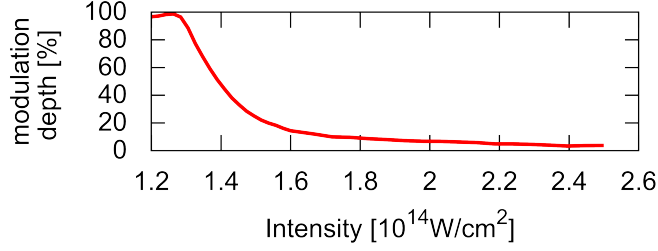


Figure IV.6.3.: Predicted modulation depth as a function of laser intensity for a 4.5 fs pulse.

the calculated ionization potentials, the field strength and pulse length. The slightly lower intensity ( $1.35 \times 10^{14} \text{ W/cm}^2$ ) used in the model compared to the experimentally determined intensity ( $1.5 \times 10^{14} \text{ W/cm}^2$ ) may be attributed to the difficulty to measure exact laser intensities in the experiment.

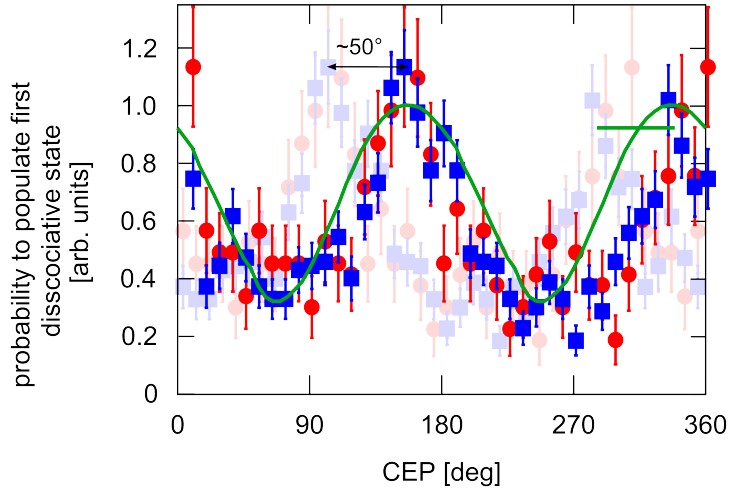


Figure IV.6.4.: Model predictions for the dissociation yield at  $I = 1.35 \times 10^{14} \text{ W/cm}^2$  and a full-width at half maximum of 4.5 fs. Green line: model prediction; blue and red dots: experimental results for  $\text{CH}^+ + \text{CH}^+$  and  $\text{C}_2\text{H}^+ + \text{H}^+$ .

The relative shift observed can be attributed to several issues: First, the location of the minima and maxima depends strongly on the exact pulse length, although the locations are relatively unaffected when changing the envelope of the vector potential  $\mathbf{A}(t)$  in Eq. IV.6.2 from “ $\cos^2$ ” to “ $\cos$ ”, while keeping the full-width at half maximum constant. Secondly, the position of the maxima depends sensitively on the interplay of the probability to ionize in the first step and the recollision energy for that starting time. It is,

however known, that the ADK rate does not correctly reproduce the time dependent ionization rate in molecules [122]. Therefore, the positions of the minima and maxima may be affected. Another possible reason for the shift is that a very simplified potential was used in the propagation of the electron: In the present calculations, an atomic 1D, soft-core potential was used instead of the correct 3D, non-spherically symmetric, multi-center potential of the molecule. The Coulomb field is, however, known to have an influence on the relationship between the CEP and recollision energy [154]. The shift may thus also be attributed to the simplified propagation of the electron. Finally, the role of the Coulomb field also directly influences the calibration of the absolute phase in the experiment. The phase shift may thus be due to both, a shift in the experimental data, and a shift in the simulation.

For higher intensities, independently of the exact parameters (pulse length, pulse shape) used in the model, the modulation strongly decreases. The residual modulation depth of 4% for high intensities and a full-width at half-maximum of 4.5 fs is in good agreement with the experimentally observed vanishing modulation at  $3 \times 10^{14} \text{ W/cm}^2$ .

At low intensities, for which recollisional ionization is forbidden, the present model suggests zero fragmentation probability. This is of course not correct. At lower intensities, recollisional excitation and recollisional excitation with subsequent ionization may become important.

To cross-check the results, the same model is applied to predict the yield of the non-dissociative  $C_2H_2^{2+}$  channel. To this end, a smaller  $I_P^{\text{ion}}$  of approximately 20 eV is used, corresponding to the vertical excitation energy from the ion to the metastable, dicationic groundstate. Using the same pulse length and intensity as in Fig. IV.6.4 ( $\tau = 4.5 \text{ fs}$ ,  $I = 1.35 \times 10^{14} \text{ W/cm}^2$ ), this results in a modulation depth of 12% , mainly due to a CEP dependence of the recollision step. This is clearly not fully in agreement with the experimental results, in which the normalized yield of  $C_2H_2^{2+}$ , with a modulation depth of approximately 5%, exactly follows the yield of  $C_2H_2^+$  (see Fig. IV.2.1), suggesting that even this small residual modulation is not due to the recollision step. A possible explanation for this discrepancy is that sequential ionization and not recollisional ionization is dominant for the population of the dicationic groundstate. This is, however, not likely due to the results shown in Fig. IV.4.2. Another possible explanation is the following: while changing the envelope of the vector potential  $\mathbf{A}(t)$  to “cos” instead of “ $\cos^2$ ” does not strongly influence the modulation depth calculated for the production of  $C_2H_2^+$ , shorter pulse lengths strongly increases the modulation depth and longer pulses

decrease the modulation depth slightly<sup>1</sup>. Slightly longer pulse lengths would thus be in better agreement with the experimental results.

## IV.7. Conclusion

In conclusion, the most likely mechanism responsible for the experimentally found CEP control of molecular fragmentation was identified by investigating the potential energy structure of acetylene, performing quantum dynamics calculations and modelling the recollision process: while field excitations via dipole transitions are found to be of minor importance, an energy threshold effect allows reproducing the experiments qualitatively. This effect is based on the fact that fragmentation may occur whenever an excited, dissociative state is populated. The lowest excited state supporting fragmentation into both  $\text{C}_2\text{H}^+ + \text{H}^+$  and  $\text{CH}^+ + \text{CH}^+$  is the  $^3\Pi_u$  state. This state can be populated by recollisional ionization of electrons from inner-valence molecular orbitals. If the recollision energy is tuned to the ionization potential of this transition, the dependence of the recollision energy on the CEP can be used as control tool to enhance or suppress fragmentation. This dependence could be modelled qualitatively using a simple, 1D recollision model. Slight discrepancies between the model and the experiment can be attributed to the simplified potential used in the model and possibly differences in the exact pulse length.

The mechanism identified strongly differs from mechanisms identified so far in CEP dependent processes [35, 37, 38, 40, 45] and can be expected to allow fragmentation control for a wide range of molecules, since the only prerequisite are energetically separated bound and dissociative states.

---

<sup>1</sup>The comparison of the modulation depth for different pulse lengths was performed using different intensities. The intensities were thereby chosen such that the modulation depth for the fragmentation channel fits the experiment. This is motivated by the fact that the measurement of the exact intensity is difficult in the experiment.



## Part V.

# Reaction control of $\text{C}_2\text{H}_2^{2+}$ via alignment

## V.1. Introduction

The alignment dependence of strong field processes has been studied extensively in the past. Examples are the alignment-sensitive yields of molecular strong-field ionization (e.g. [155, 156, 157]) and the alignment dependence of the high-harmonic generation (e.g. [28, 158, 159]), which has also been applied to the tomographic reconstruction of molecular orbitals [32].

In a recent experiment, our collaboration partners Dr. Xinhua Xie and Dr. Markus Kitzler from the Vienna University of Technology successfully exploited alignment dependence to selectively control the yield of different fragmentation channels of  $\text{C}_2\text{H}_2^{2+}$  [47]. This experiment was the first evidence that is not only possible to control the overall fragmentation yield of polyatomic molecules using ultrashort IR laser pulses, but that is also possible to tune the relative yields of different reaction channels.

After a brief overview over the experimental results, the focus of this chapter lies on the theoretical description, interpretation and analysis of these recent results. To this end, the alignment dependence of sequential and non-sequential double ionization and of field excitation of  $\text{C}_2\text{H}_2$  will be studied. This will allow making theoretical predictions that can be compared against the experimental results and thus inferring which processes are relevant. It will be shown that the experimental results can be interpreted as combined effect of the alignment dependence of sequential and recollisional ionization.

## V.2. Experimental results

In a recent experiment, X. Xie and M. Kitzler investigated the possibility of exploiting molecular alignment in order to control molecular reactions in ultrashort, strong fields. In their experiment, they were able to show that the relative probability for dissociation of  $\text{C}_2\text{H}_2^{2+}$  and  $\text{C}_2\text{H}_2^+$  into different fragmentation channels ( $\text{C}_2\text{H}^+\text{H}^+$ ,  $\text{CH}^+\text{CH}^+$ ,  $\text{CH}_2^+\text{C}^+$ ,  $\text{C}_2\text{H}^+\text{H}$ ) can be tuned efficiently using impulsive alignment as a control tool.

Details on the experimental setup can be found in Ref. [47] and only a short description will be given in the following. In an ultra-high vacuum chamber,  $\text{C}_2\text{H}_2$  molecules are impulsively aligned by a linearly polarized laser pulse with a time duration of approximately 50 fs and an intensity of  $I \approx 2 \times 10^{13} \text{ W/cm}^2$ . This alignment pulse creates a rotational wavepacket of molecules. During the half-revival of this wavepacket, the orientation of the molecular axis relative to the laser polarization axis changes from preferentially parallel at delay-times of  $\tau \approx 6.8 \text{ ps}$  to preferentially orthogonal at 7.2 ps. Scanning through this half-revival by changing the relative delay of the sub-5 fs probe pulse to the alignment pulse in the range of 6–8 ps, the collinearly polarized probe pulse, with intensities ranging from  $2 \times 10^{14} \text{ W/cm}^2$  to  $7 \times 10^{14} \text{ W/cm}^2$  is focused onto the molecular beam. This probe pulse is sufficiently strong to multiply ionize  $\text{C}_2\text{H}_2$  and initiate the molecular fragmentation. Detecting the resulting fragment ions in coincidence, individual fragmentation pathways can be identified and analysed.

As a measure of the alignment quality achieved in the experiment, the experimentally obtained values for the expectation value  $\langle \cos^2(\theta) \rangle$  around the half-revival are shown in Fig. V.2.1. These values were derived from four-body coincidence measurements of the ions created in the Coulomb explosion of  $\text{C}_2\text{H}_2^{4+}$ . Random alignment would correspond to  $\langle \cos^2(\theta) \rangle = \frac{1}{3}$ . The proton yield, also shown in Fig. V.2.1, can be used to trace the rotational wavepacket through the quarter ( $\tau \approx 3.5 \text{ ps}$ ), the half- and the three quarter-revival to the full revival at  $\tau \approx 14 \text{ ps}$ .

The yields of different fragmentation and ionic channels are shown in Fig. V.2.2 as

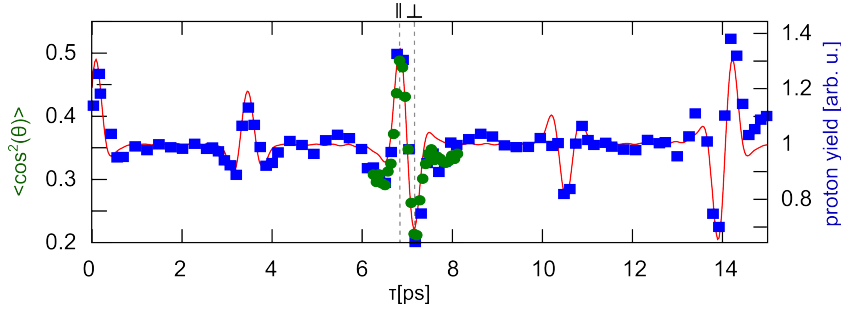


Figure V.2.1.: Measured expectation value of  $\cos^2(\theta)$  (green dots) derived from the Coulomb explosion data of  $C_2H_2^{4+}$  and the proton yield (blue dots, arbitrary units) as a function of delay time,  $\tau$ . Red line: simulation of  $\langle \cos^2(\theta) \rangle$  for a rotational wavepacket.

a function of the delay time  $\tau$ , i.e. the relative delay between the alignment and the probe pulse, near the half revival. As mentioned above, at  $\tau \approx 6.8$  ps the molecules are

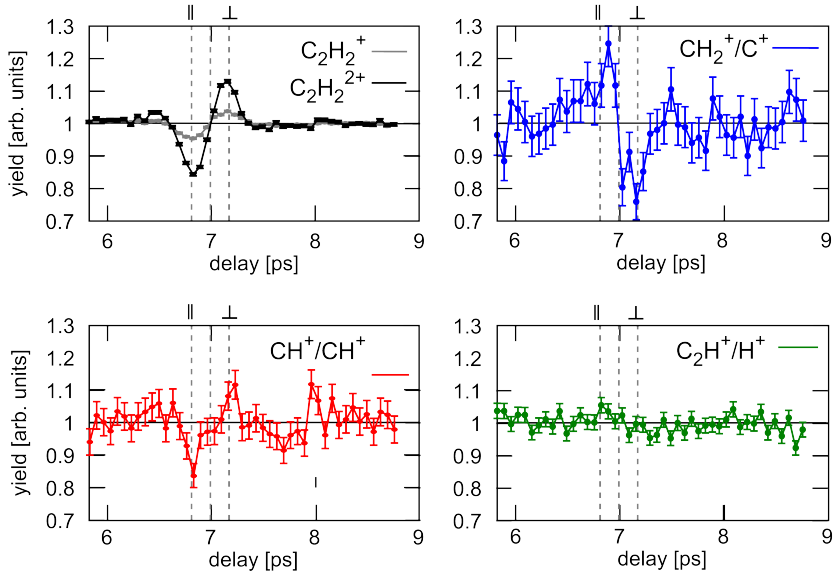


Figure V.2.2.: Measured yield of  $C_2H_2^+$  (a),  $C_2H_2^{2+}$  (a),  $CH_2^+ + C^+$  (b),  $CH^+ + CH^+$  (c),  $C_2H^+ + H^+$  (d) as a function of delay time for a pulse duration of the probe pulse of  $\tau = 4.5$  fs and an intensity of  $I = 4 \times 10^{14}$  W/cm<sup>2</sup>.

preferentially aligned parallel to the probe pulse (see Fig. V.2.1), whereas  $\tau \approx 7.2$  ps corresponds to preferentially orthogonal alignment. The yield of most channels is strongly modulated as a function of delay time  $\tau$ , suggesting a strong alignment dependence of the fragmentation yields. Moreover, the delay dependence differs for the individual fragmentation channels. The C-C bond breakage, for example, shows an enhanced yield at

## V.2. Experimental results

$\tau \approx 7.2$  ps, i.e. orthogonal alignment, and is suppressed at  $\tau \approx 6.8$  ps. The isomerization channel,  $\text{CH}_2^+ + \text{H}^+$ , on the other hand, features the opposite behaviour.

Only the  $\text{C}_2\text{H}^+ + \text{H}^+$  channel does not exhibit any apparent alignment dependence. However, as shown in Fig. V.2.3 the double peak structure of the kinetic energy release (KER) of this channel, with maxima around  $\text{KER} \approx 3.5$  eV and 5 eV, suggests that two or more reaction pathways contribute to this channel. Separating the events for low KER ( $\text{KER} < 4$  eV) and high KER ( $\text{KER} > 4.5$  eV), an alignment dependence can be reestablished (see Fig. V.2.3.b and c). The low and high KER contributions thereby show an opposite alignment behaviour. The weak alignment dependency of the KER-integrated  $\text{C}_2\text{H}^+ + \text{H}^+$  yield is thus a result of two or more rivalling reaction pathways with inverse alignment sensitivity.

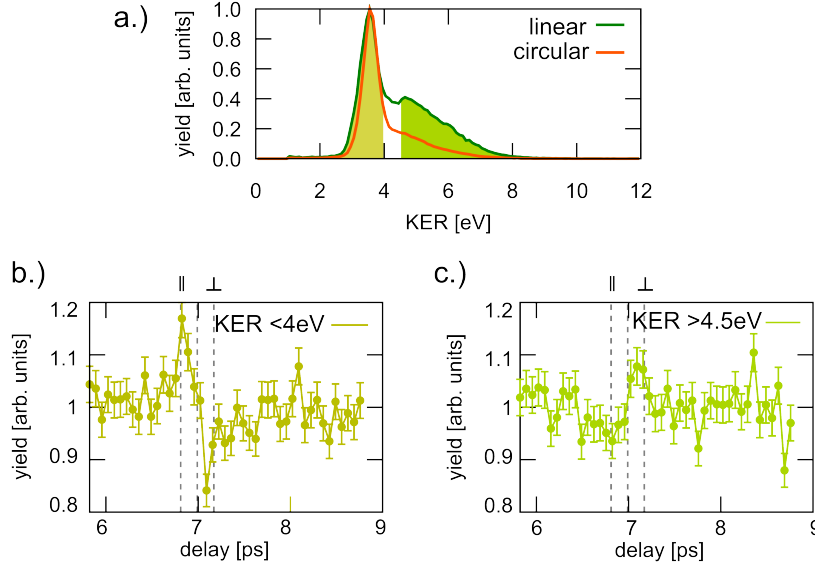


Figure V.2.3.: a.) Distribution of the kinetic energy release for the  $\text{C}_2\text{H}^+ + \text{H}^+$  channel for linear polarization (dark green line), a pulse duration of  $\tau = 4.5$  fs and an intensity of  $I = 4 \times 10^{14}$  W/cm<sup>2</sup> as well as for circular polarization (orange line),  $\tau = 4.5$  fs and  $I = 3 \times 10^{14}$  W/cm. The shaded regions mark the integration regimes used in panels b and c: b.) Delay dependent yield of  $\text{C}_2\text{H}^+ + \text{H}^+$  with  $\text{KER} < 4$  eV and c.) with  $\text{KER} > 4.5$  eV.

In circularly polarized light, the higher KER peak of the  $\text{C}_2\text{H}^+ + \text{H}^+$  channel can be efficiently suppressed (see Fig. V.2.3.a) and an alignment dependence with a maximum around  $\tau \approx 7.2$  fs is observed even in the KER-integrated case (not shown).

Overall, this experiment clearly shows that by controlling the molecular alignment via the delay time  $\tau$ , the relative yield of the individual channels can be controlled. This proves that even for probe pulses on the few-femtosecond time scale, alignment can be used as a control tool in molecular fragmentation reactions, which proceed on a multi-femtosecond time scale.

### V.3. Alignment dependence of sequential ionization

To analyse the above described results, it is important to identify all processes that may introduce an alignment dependence: strong-field ionization is known to be alignment sensitive (e.g. [155, 156, 157]). Furthermore, non-sequential double ionization may also be alignment dependent (e.g. [29, 160]) and finally, field excitation due to dipole transitions between different electronic states will be alignment sensitive due to the vector character of the dipole transition moments coupling the Born-Oppenheimer states.

The focus of this section is the study of the alignment dependence of sequential field ionization. At the intensities considered in the experiment described above, sequential ionization can be expected to give the main contribution to the  $C_2H_2^{2+}$  yield [147]. How and why the alignment dependence of sequential ionization may lead to a channel selective alignment dependence of molecular fragmentation in  $C_2H_2$  can be explained as follows: qualitatively, a bonding  $\pi$ -type orbital can be expected to have a higher ionization rate if the laser polarization is orthogonal to the molecular axis than when it is aligned parallel. For  $\sigma$ -type orbitals, the opposite can be expected. Figure V.3.1 shows the seven lowest molecular orbitals of acetylene, calculated near the equilibrium geometry of  $C_2H_2$  using a CAS(8,8) calculation and the cc-pVTZ basis set. The seven lowest natural orbitals of acetylene have near double occupancy. The two (degenerate) energetically highest strongly occupied orbitals have  $\pi_u$  symmetry. One may thus expect acetylene to ionize preferentially when aligned orthogonally to the laser polarization direction. However, it is known that lower lying orbitals may have a significant influence on strong field ionization [161, 162, 163, 164]. In the case of acetylene, the next lower

### V.3. Alignment dependence of sequential ionization

---

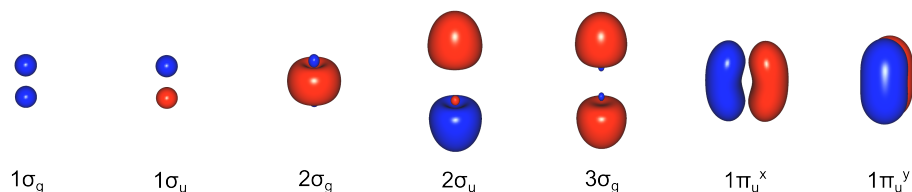


Figure V.3.1.: Molecular orbitals of  $C_2H_2$  with near double occupancy, calculated by CAS(8,8). (Isovalue 0.1)

lying orbital is the  $3\sigma_g$  orbital, for which the angle resolved ionization rate can be expected to be different from that of the  $\pi_u$  orbitals. Ionization from different orbitals will lead to the population of different final states. Since the potential energy surface of different states can strongly differ, different states may predominantly support different molecular reactions. Therefore a difference in the alignment dependent ionization rate from  $\pi$  and  $\sigma$  orbitals may lead to alignment dependent fragmentation yields.

To provide a quantitative analysis, allowing a comparison with the experiment, two different methods were applied to calculate the alignment dependent ionization rate of acetylene: the first approach is based on time-dependent density functional theory (TD-DFT) [165]; the second approach makes use of tunnelling theory and the concept of Dyson orbitals.

The Dyson orbital approach establishes a direct connection to the electronic states populated after ionization, which is important in the following analysis. However, it is applied here within a tunnelling picture. Due to over-the-barrier effects, this limits the analysis to the second ionization step or to field strengths considerably below the experimentally relevant ones, where in turn the applicability of tunnelling theory for 800 nm radiation becomes questionable. The TD-DFT approach, on the other hand, suffers from the known limitations of TD-DFT, such as problems describing non-linear response, the dependence on the exchange-correlation functional, space charge and self-interaction effects. Furthermore, the TD-DFT approach requires several assumptions, such as the similarity of Kohn-Sham orbitals and molecular orbitals. However, as shown in the following chapters, both approaches lead to very similar results, proving the methods to be comparatively robust against the approximations made.

### V.3.1. Time-dependent density functional theory approach (TD-DFT)

The time-dependent density functional theory calculations were performed on a grid with absorbing boundaries for both, the acetylene molecule,  $C_2H_2$ , and the singly charged ion,  $C_2H_2^+$ . The singly charged ion was thereby considered in two different initial states, one corresponding to the ionic ground state and one corresponding to the first excited ionic state, described by one electron missing from the  $3\sigma_g$  orbital. The obtained energy spacings between the neutral ground state and the ionic ground state and excited state were found to be 11.3 eV and 17.0 eV in close agreement to values given in literature (11.5 eV and 17.2 eV [166]). The Kohn-Sham orbitals resulting from the  $C_2H_2$  calculation are shown in Fig. V.3.2.

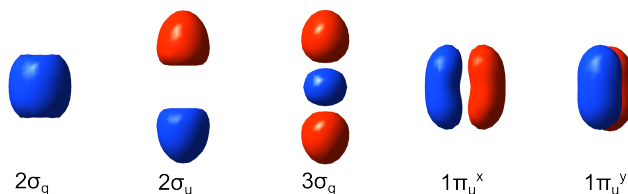


Figure V.3.2.: Kohn-Sham orbitals of  $C_2H_2$  calculated by DFT. (Isovalue 0.1).

In the time-dependent calculations, a strong and short laser pulse (4.5 fs FWHM with a sinusoidal envelope,  $I = 2.8 \times 10^{14} \text{ W/cm}^2$ ), polarized at an angle  $\theta$  relative to the molecular axis, was applied to the molecule<sup>1</sup>. The computational grid was chosen sufficiently large to allow the classical tunnel exit to lie well within the grid. The box size used in most of the calculations was  $64 \text{ au} \times 40 \text{ au} \times 37 \text{ au}$ , where the first dimension corresponds to the direction of the laser polarization direction, and defines, together with the second dimension the plane in which the molecular axis lies. Sin-shaped complex absorbing boundaries with a width of 4 au and a height of  $-1.5 \text{ au}$  were used. The resulting time evolution of the electronic density projected onto the polarization direction of the laser field is shown exemplary for  $C_2H_2$  at an alignment angle of  $\theta = 40^\circ$  in figure V.3.3. Near each field maximum, electronic density is drawn away from the vicinity of the molecule. The charge lost during the calculation via the absorbing boundaries is interpreted as the probability for single ionization. Fig. V.3.4 shows the time evolution of the charge  $n_i(t)$

<sup>1</sup>Due to the short duration of the laser pulse, it would be better to define the electric field via the vector potential. However, the Octopus software package allows only sinusoidal envelopes and no  $\cos^2$  envelope. Since the former would lead to a sudden onset of the electric field, and since the final momentum of the electrons is not of interest in the present calculations, the field was defined directly.

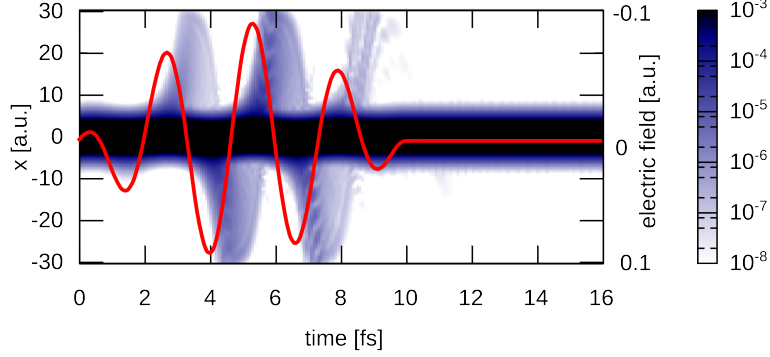


Figure V.3.3.: Time evolution of the electronic density of  $\text{C}_2\text{H}_2^+$  projected onto the laser polarization direction for an alignment angle of  $\theta = 40^\circ$ . Superimposed red line: electric field.

contained in each Kohn-Sham orbital, where

$$n_i(t) = N_i^o \langle \phi_i(t, \theta) | \phi_i(t, \theta) \rangle \quad (\text{V.3.1})$$

with the initial occupation number  $N_i^o$  of the  $i$ -th orbital. The calculation of the overlap  $\langle \phi_i(t, \theta) | \phi_i(t, \theta) \rangle$  is no standard feature of the Octopus code and was implemented as part of this thesis.

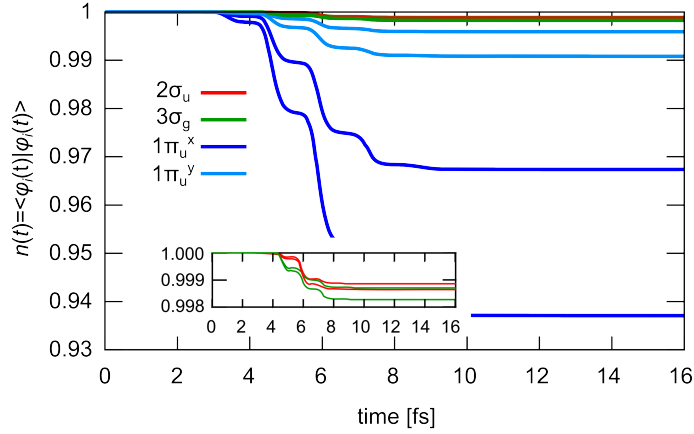


Figure V.3.4.: Time evolution of  $n_i(t)$  of the Kohn-Sham spin-orbitals of  $\text{C}_2\text{H}_2^+$  for an alignment angle of  $\theta = 40^\circ$ .

To limit the amount of double ionization and to minimize the influence of space charge



effects in the continuum, the strength of the pulse applied in the simulations was restricted to values slightly lower than in the experiment with  $E = 0.09$  au, corresponding to  $I = 2.8 \times 10^{14}$  W/cm<sup>2</sup>. At this intensity, the total amount of charge lost is lower than 0.6 au for  $C_2H_2$ , 0.1 au for  $C_2H_2^+$  in the ground state and 0.2 au in the excited state.

Double ionization is described as two subsequent processes:  $C_2H_2 \rightarrow C_2H_2^+$  followed by a second ionization step  $C_2H_2^+ \rightarrow C_2H_2^{2+}$  or  $C_2H_2^{+*} \rightarrow C_2H_2^{2+}$ , where the star denotes the excited state. This is necessary due to the fact that single and double ionization cannot be separated in TD-DFT calculations since they both only manifest themselves in a decrease of the norm.

In Eq. (V.3.1), the charge  $n_i(t)$  was defined per Kohn-Sham orbital. The concept of Kohn-Sham orbitals will be necessary to allow an interpretation of the experimental results. However, due to the presence of the field, different Kohn-Sham orbitals tend to mix during the presence of the pulse as shown in Fig. V.3.5.

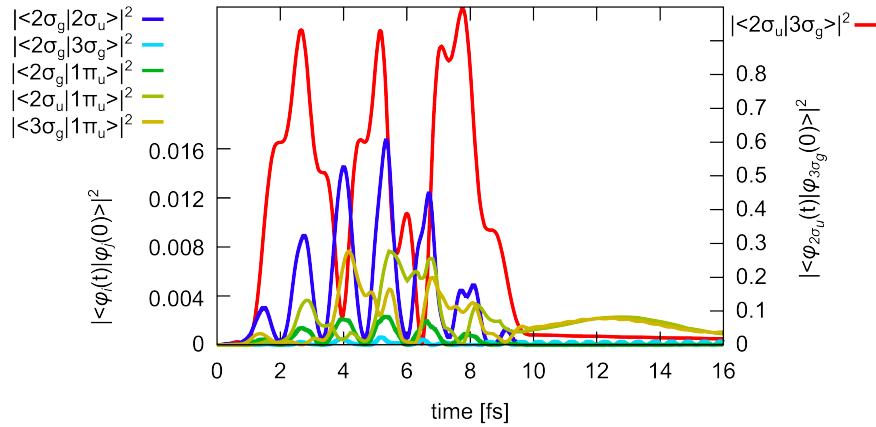


Figure V.3.5.: Time evolution of selected projections  $P_{i,j} = |\langle \phi_i^{KS}(t) | \phi_j^{KS}(0) \rangle|^2$  for an alignment angle of  $\theta = 40^\circ$ . Note the different scale for the projection  $P_{2\sigma_u, 3\sigma_g}$

For a general orientation of the molecular axis relative to the laser polarization, the symmetry of the molecule–field system reduces to the  $C_i$  point group. The orbitals having  $\pi_u$  symmetry in the  $D_{\infty h}$  point group corresponding to the equilibrium geometry of  $C_2H_2$ , have  $A_u$  symmetry in  $C_i$  and may thus couple to the  $\sigma_g$  orbitals, having  $A_g$  symmetry in  $C_i$  since the dipole operator has  $A_u$  symmetry in  $C_i$ . The  $\sigma_g$  orbitals, on their part, may couple to  $\pi_u$  and  $\sigma_u$  ( $A_u$  symmetry in  $C_i$ ) orbitals. In the special case of parallel alignment ( $\theta = 0^\circ$ ), only transitions from  $\sigma_g$  to  $\sigma_u$  are allowed, while transitions to  $\pi_u$  are symmetry forbidden. For orthogonal alignment ( $\theta = 90^\circ$ ), the

former transitions are symmetry forbidden and the latter are allowed. In the present calculation, the coupling between the  $3\sigma_g$  and the  $2\sigma_u$  orbital is observed to become very large, with the two orbitals effectively switching at some moments during the propagation (see Fig. V.3.5). Coupling with even lower lying  $\sigma$  states, on the other hand, is negligible and the coupling between the  $\pi_u$  and the  $\sigma$  states remains well below 1.5% even for  $\theta = 90^\circ$ , where the strongest coupling can be expected.

Due to the strong coupling of the  $2\sigma_u$  and the  $3\sigma_g$  orbital, norm lost from the orbital corresponding at  $t = 0$  fs to the  $2\sigma_u$  contains — to a certain extent — norm lost from an orbital having  $\sigma_g$  character. This prohibits distinguishing between these orbitals. Ionization from  $\sigma_g$  and  $\sigma_u$  orbitals was thus treated as a sum over all  $\sigma$  orbitals. Due to the weak coupling of the  $\pi$  states to the  $\sigma$  states, it is possible to separate the ionization from  $\sigma$ -type orbitals and  $\pi$ -type orbitals. With this in mind, the following ionization probabilities from  $\sigma$  and  $\pi$  orbitals were defined:

$$p_\sigma^{0/+}(\theta) = \sum_{\sigma \text{ orb.}} n_i^{0/+}(t=0, \theta) - n_i^{0/+}(t=t_f, \theta), \quad (\text{V.3.2})$$

$$p_\pi^{0/+}(\theta) = \sum_{\pi \text{ orb.}} n_i^{0/+}(t=0, \theta) - n_i^{0/+}(t=t_f, \theta), \quad (\text{V.3.3})$$

where  $\theta$  denotes the angle between the laser polarization direction and the molecular axis. The time  $t_f$  is chosen long enough after the end of the pulse such that the electronic density released during the pulse has left the grid. The superscripts “0” and “+” denote ionization from  $\text{C}_2\text{H}_2$  and  $\text{C}_2\text{H}_2^+$ , respectively.

Double ionization yields were defined as

$$p_{a,b}^{2+} = \int dt \left( \sum_a n_i^0(0) - n_i^0(t) \right) \cdot \left( \sum_b n_i^+(t) - n_i^+(t_f) \right), \quad (\text{V.3.4})$$

with  $p_{\pi,\sigma}$  denoting the probability to ionize from a  $\pi$ -type orbital in the first step and from a  $\sigma$ -type orbital in the second step, etc. If the first ionization step corresponds to ionization from a  $\sigma$ -type orbital, then the  $n_i^+$  should be taken from the calculations for the excited ion.

The resulting single and double ionization yields as a function of the alignment angle  $\theta$  are shown in Figs. V.3.6 and V.3.7. Note that possible influences of the carrier-envelope phase on the alignment dependent ionization yield [167] were not investigated since the experiment was not performed using CEP stable pulses. Accordingly, the ionization yield is assumed to conserve the molecule’s symmetry.

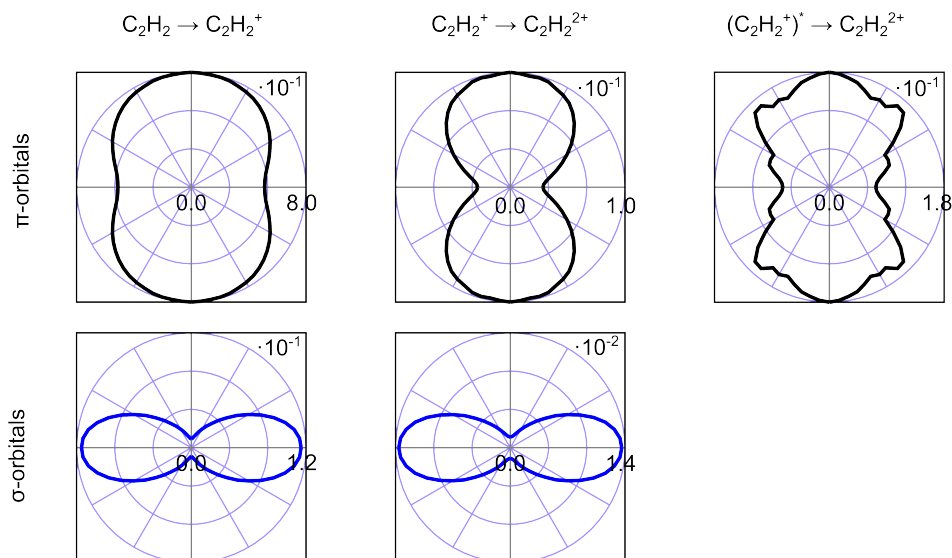


Figure V.3.6.: Angular plots of the alignment dependent ionization probabilities from specific orbitals. Black line: probability to ionize from a  $\pi$  orbital, blue line: probability to ionize from a  $\sigma$  orbital for a.)  $C_2H_2$ , b.)  $C_2H_2^+$ , c.)  $C_2H_2^{+*}$ .

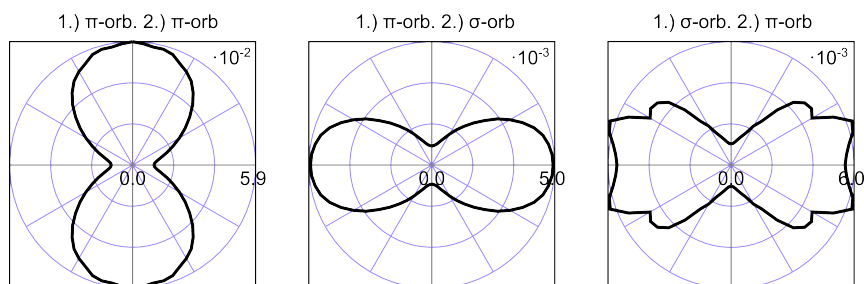


Figure V.3.7.: Angular plots of the alignment dependent probability for sequential ionization. left: ionization from a  $\pi$  orbital in the first and second ionization step; middle: ionization from a  $\pi$  orbital in the first and from a  $\sigma$  orbital in the second step; right: ionization from a  $\sigma$  orbital followed by ionization from a  $\pi$  orbital. (See text for details.)

### V.3. Alignment dependence of sequential ionization

As expected, the  $\pi$  orbitals ionize preferentially, when aligned orthogonally to the laser polarization axis, while the  $\sigma$  orbitals have a strongly enhanced ionization probability for parallel alignment. Ionization from  $\pi$  orbitals in  $\text{C}_2\text{H}_2$  (Fig. V.3.6.a) depends only rather weakly on the alignment. This may be explained by the fact that in the neutral, ionization from the  $\pi$  orbital is in the classical over-barrier regime (in a spherical potential at  $I = 4 \times 10^{14} \text{ W/cm}^2$ , the barrier maximum lies at  $-16 \text{ eV}$ , while the ionization potential from the  $\pi$  orbitals is  $I_p \approx 11.6 \text{ eV}$  [166] and therefore clearly above the barrier). Overall, the alignment dependence is more pronounced for the  $\sigma$ -type orbitals than for the  $\pi$ -type orbitals such that the combined probability for ionization from a  $\pi$ -type orbital followed by a  $\sigma$ -type orbital and vice versa is dominated by the angle dependence of the  $\sigma$  orbital, i.e. is preferred for small angles  $\theta$  (see Fig. V.3.7 b. and c.).

Now that the alignment dependence of ionization from different orbitals has been established, the next step is to relate these probabilities to the probability for the reaction to end in a specific reaction channel. First, the removal of electrons from specific orbitals is related to the population of specific dicationic states. To this end, table V.3.1 shows the occupation of orbitals in configuration state functions (CSFs) contributing with weights larger than 0.02 to the wavefunctions of the lowest lying electronic states of  $\text{C}_2\text{H}_2^{2+}$ . The groundstate configuration of  $\text{C}_2\text{H}_2$  is dominated by the following determinant:  $(1\sigma_g^2, 1\sigma_u^2, 2\sigma_g^2, 2\sigma_u^2, 3\sigma_g^2, 1\pi_u^2, 1\pi_u^2)$ . Obviously, the extraction of two electrons from the  $\pi$  orbital system of  $\text{C}_2\text{H}_2$  leads mainly to the population of the  $^3\Sigma_g^-$  groundstate, the  $^1\Delta_g$  or  $^1\Sigma_g^+$  state of  $\text{C}_2\text{H}_2^{2+}$  (see also Fig. V.3.8).

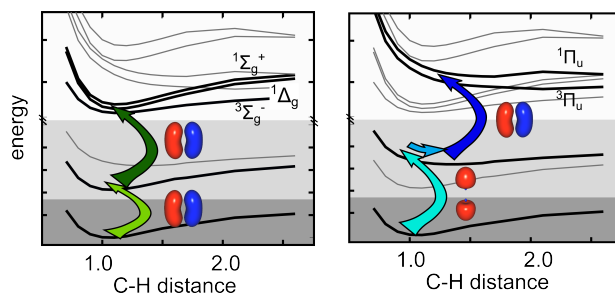


Figure V.3.8.: Schematic drawing of states populated after the extraction of two  $\pi_u$  electrons (left) and one  $\sigma_g$  and one  $\pi_u$  electron. Dark gray region: neutral, light gray region: cationic states, all other states: dicationic states.

If, on the other hand, one electron is removed from the  $3\sigma_g$  orbital and one from a  $\pi$  orbital, mainly the singlet and triplet  $\Pi_u$  states will be populated. The molecular orbitals of the CAS calculation are sufficiently similar to the Kohn-Sham orbitals to allow relating the two sets of orbitals with each other (compare Figs. V.3.1 and V.3.2).

state	CSF										weight
	$1\sigma_g$	$1\sigma_u$	$2\sigma_g$	$2\sigma_u$	$3\sigma_g$	$1\pi_u^x$	$1\pi_u^y$	$1\pi_g^x$	$1\pi_g^y$	$3\sigma_u$	
$^3\Sigma_g^-$											
$^1\Delta_g$ (state 1)	1↓	1↓	1↓	1↓	1↓	1	1				0.96
	1↓	1↓	1↓	1↓	1↓	1	↓				0.85
	1↓	1↓	1↓	1↓	1↓	1↓					0.05
$^1\Delta_g$ (state 2)	1↓	1↓	1↓	1↓	1↓		1↓				0.05
	1↓	1↓	1↓	1↓	1↓	1↓					0.43
	1↓	1↓	1↓	1↓	1↓		1↓				0.43
$^1\Sigma_g^+$											
	1↓	1↓	1↓	1↓	1↓	1↓					0.47
	1↓	1↓	1↓	1↓	1↓		1↓				0.47
$^3\Pi_u$ (state 1)											
	1↓	1↓	1↓	1↓	1	1↓	1				0.89
	1↓	1↓	1↓	1	1↓	1↓			1		0.03
$^3\Pi_u$ (state 2)											
	1↓	1↓	1↓	1↓	1	1	1↓				0.89
	1↓	1↓	1↓	1	1↓		1↓	1			0.03
$^1\Pi_u$ (state 1)											
	1↓	1↓	1↓	1↓	1	↓	1↓				0.91
	1↓	1↓	1↓	1	1↓	↓	1		↓		0.02
$^1\Pi_u$ (state 2)											
	1↓	1↓	1↓	1↓	1	1↓	↓				0.91

Table V.3.1.: Occupation of orbitals in configuration state functions (CSFs) contributing with weights larger than 0.02 to the wavefunctions of the lowest lying electronic states of  $C_2H_2^{2+}$ .

This correspondence is used to assign the alignment dependence of sequential ionization from two  $\pi$  orbitals to the alignment dependent population of the  ${}^3\Sigma_g^-$ ,  ${}^1\Delta_g$  and  ${}^1\Sigma_g^+$  states as well as to relate the alignment dependence of the population of the  $\Pi_u$  states with the alignment dependence of ionization from a  $\pi$  orbital, followed by ionization from a  $\sigma$  orbital or vice versa.

### V.3.2. Comparison of TDDFT with a Dyson orbital approach

To validate the above approach and before proceeding with the interpretation of the experimental results, the TDDFT based approach was compared with a second, conceptually different approach to calculate the alignment dependence for the population of specific dicationic states: In this second approximation, the population of a specific state via ionization is treated as tunnelling process from an effective one particle wavefunction, the Dyson wavefunction given by

$$\phi_D(\mathbf{r}) = \langle \Psi^{N-1}(\mathbf{r}_1 \dots \mathbf{r}_{N-1}) | \Psi^N(\mathbf{r}_1 \dots \mathbf{r}_{N-1}, \mathbf{r}) \rangle_{\mathbf{r}_1 \dots \mathbf{r}_{N-1}}. \quad (\text{V.3.5})$$

This corresponds to the overlap of an  $N$ -electron wavefunction  $\Psi^N$  of a specific electronic configuration of  $\text{C}_2\text{H}_2^+$  with an  $(N - 1)$ -electron wavefunction describing an electronic state of  $\text{C}_2\text{H}_2^{2+}$ . In the present approach, these many-particle wavefunctions were taken from CAS(8,8) calculations. Since the tunnelling theory requires a very good description of the wavefunction tails, an adjusted aug-cc-pV5Z basis was used, as suggested in Ref. [168]. To allow a decent description of the tails, two additional diffuse orbitals for each angular momentum were added. On the other hand, the orbitals with angular momentum quantum number  $l = 5$  (h-orbitals) were removed from the basis to limit the size of the basis set. The molecular geometry was kept at the ground state geometry of the neutral, i.e. linear with a CC bond distance of 1.2 Å and a CH bond distance of 1.0 Å, similarly to the TD-DFT calculations. This is justified by the fact that the ionization process occurs on a fast time scale below the 5 fs duration of the laser pulse. The nuclear configuration can thus not change significantly during this time. The overlap integral was calculated using the integration schemes described in appendix B.1. Table V.3.2 shows the resulting Dyson orbitals for transitions from the doubly degenerate  ${}^2\Pi_u$  groundstate of the cation to the  ${}^3\Sigma_g^-$ ,  ${}^1\Delta_g$ ,  ${}^1\Sigma_g^+$ ,  ${}^3\Pi_u$  and  ${}^1\Pi_u$  states of the dication together with their ionization potentials,  $I_P$ .



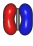

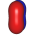

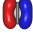

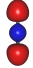


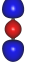



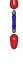
Nr	final state	Dyson orbital		$I_P$
1,2	$^3\Sigma_g^-$			21.1 eV
3,4	$^1\Delta_g$ (state 1)			33.6 eV
5,6	$^1\Delta_g$ (state 2)			33.6 eV
7,8	$^1\Sigma_g^+$			34.3 eV
9,10	$^3\Pi_u$ (state 1)			38.4 eV
11,12	$^3\Pi_u$ (state 2)			38.4 eV
13,14	$^1\Pi_u$ (state 1)			39.2 eV
15,16	$^1\Pi_u$ (state 2)			39.2 eV

Table V.3.2.: Dyson orbitals calculated from the degenerate  $^2\Pi_u$  state of  $C_2H_2^+$  to different dicationic states. The left and right figures correspond to the Dyson orbital from the first and second degenerate  $^2\Pi_g$  state. Note that the orientation of the  $\pi_x$  and  $\pi_y$  orbitals differs in the calculations for the cation and the dication.

The tunnelling ionization rate  $\Gamma$  is calculated according to Ref. [168] as

$$\Gamma \propto \int dp_x \int dp_y \sqrt{2I_P} e^{-2 \int_{z_0}^{z_{\text{ex}}} p_z(z') dz'} \left| \tilde{\phi}_D(p_x, p_y, z_0) \right|^2 e^{-p_\perp^2 \frac{\sqrt{2I_P}}{E}}, \quad (\text{V.3.6})$$

where the  $z$ -axis corresponds to the laser polarization axis,  $\tilde{\phi}_D(p_x, p_y, z_0)$  is the two-dimensional Fourier transform of the Dyson orbital in the plane orthogonal to the laser polarization  $\hat{\mathbf{z}}$ :  $\tilde{\phi}_D(p_x, p_y, z_0) = \mathcal{F} \{ \phi_D(x, y, z_0) \}_{x,y}$ , and  $p_\perp = \sqrt{p_x^2 + p_y^2}$ . The ionization potential  $I_P$  is calculated from the energy difference of the  $(N - 1)$ -particle state and the  $N$ -particle state. Eq. V.3.6 follows from the semiclassical propagation of the wavefunction through the barrier using the WKB-method [169]. The two exponential factors stem from the classical action

$$\Delta S = i \int_{z_0}^{z_e} \sqrt{p_z(z)^2 + p_\perp^2} dz \approx i \int_{z_0}^{z_e} p_z(z) dz + i \int_{z_0}^{z_e} \frac{1}{2} \frac{p_\perp^2}{p_z(z)} dz, \quad (\text{V.3.7})$$

assuming  $p_\perp$  to be small compared to  $p_z$  and approximating  $p_z$  by the SFA expression  $p_z = \sqrt{2I_P - 2Fz}$  in the term with  $p_\perp$ . For  $e^{-\int_{z_0}^{z_{\text{ex}}} p_z(z') dz'}$ , the eikonal approximation with a first order correction for a single center potential was used [169]

$$e^{-\int_{z_0}^{z_{\text{ex}}} p_z(z') dz'} \approx \left( \frac{4I_P}{Ez_0} \right)^{\frac{Q+1}{\sqrt{2I_P}}} e^{-\frac{\sqrt{2I_P}^3}{3E} + \sqrt{2I_P} z_0}, \quad (\text{V.3.8})$$

where  $Q$  is the charge of the molecule prior to ionization. The value of  $z_0$  should be chosen to lie within the potential barrier, in which case the results should be approximately independent of the exact value of  $z_0$  [168]. The exit of the barrier,  $z_{\text{ex}}$ , was calculated assuming a single center potential. The further  $z_{\text{ex}}$  lies from the center of the molecule, the better this approximation will be.

Note that other than in Ref. [168], no additional Taylor series for small  $\rho = \sqrt{x^2 + y^2}$  was applied, when evaluating Eq. V.3.6. Instead, Eq. V.3.6 was solved numerically.

Since the first ionization step with an ionization threshold of approximately 11.5 eV classically proceeds over the barrier for field intensities above approximately  $7 \times 10^{13}$  W/cm<sup>2</sup>, i.e. at intensities far below the experimentally relevant regime, tunnelling theory is not applicable to the first ionization step and only the second ionization step will be considered in the following analysis, assuming that the cationic groundstate was populated in the first step. The lowest ionization potential calculated for the transition from the cation to the dication was  $I_P \approx 21$  eV. At an intensity of  $4 \times 10^{14}$  W/cm<sup>2</sup>, as used in the experiment, and a charge  $Q = 2$  au even the second ionization step classically



lies above the barrier. In the present investigation, the intensity was thus decreased to  $I = 1.2 \times 10^{14} \text{ W/cm}^2$  corresponding to an electric field strength of  $E = 0.58 \text{ au}$ . At this intensity, for a single-center potential with charge  $Q = 2 \text{ au}$ , the entrance of the potential barrier for this  $I_P$  lies around  $z = 3 \text{ au}$  and the barrier exit around  $z = 11 \text{ au}$ . This allows a safe choice of  $z_0$  within the barrier even considering the molecular extent of approximately  $3 \text{ au}$  to either side of the molecular center. In the present study,  $z_0$  was typically set to  $6.5 \text{ au}$  and values ranging from  $6 \text{ au}$  to  $7 \text{ au}$  were compared for consistency. Larger values could not be considered due to the degrading quality of the Dyson wavefunction,  $\phi_D$  at large distances from the molecular center. Smaller values might cause  $z_0$  to lie outside the barrier.

To allow a comparison with the TD-DFT results discussed in the last section, the ionization rates for the  $\pi_u$ -type Dyson orbitals 1 to 8 (see Tab. V.3.2) corresponding to ionization rates to the  $^3\Sigma_g^-$ ,  $^1\Delta_g$  and  $^1\Sigma_g^+$  states were added, as were the rates for  $\sigma$ -type Dyson orbitals 9 to 14 for ionization to the  $^3\Pi_u$  and  $^1\Pi_u$  states. Fig. V.3.9 shows a comparison of the alignment-dependent ionization probability computed via TD-DFT with the ionization rate calculated using the Dyson-orbital approach. In spite of the

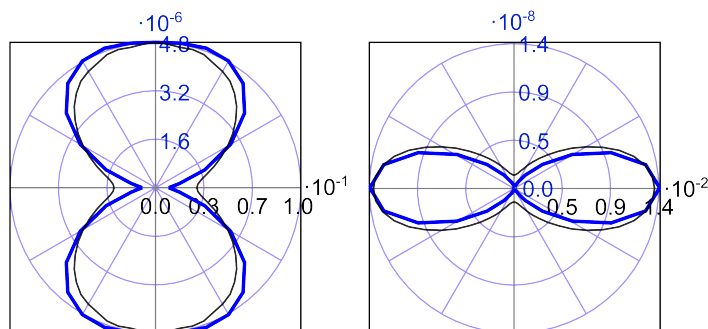


Figure V.3.9.: Comparison of the ionization probability from  $C_2H_2^+$  to  $C_2H_2^{2+}$  calculated via TD-DFT (black line, black scale) and the ionization rate calculated via the Dyson orbital approach (blue-line, blue scale). Left: for  $\pi$ -type orbitals, right: for  $\sigma$ -type orbitals. Arbitrary units are used in all cases.

large difference in intensity used in the TD-DFT calculations compared to the Dyson orbital approach, there is only a small difference in the resulting alignment dependence: the alignment dependence is slightly more pronounced in the Dyson orbital approach than in TD-DFT. It is likely that this is an effect of the higher intensity used in the TD-DFT approach. However, within the accessible intensity range from  $8.8 \times 10^{13}$ – $1.5 \times 10^{14} \text{ W/cm}^2$ , in which the value of  $z_0$  can safely be chosen to lie within the barrier, the alignment dependence does not change noticeably for the Dyson orbital approach

(see Fig. V.3.10). Another difference between the TD-DFT results and the Dyson or-

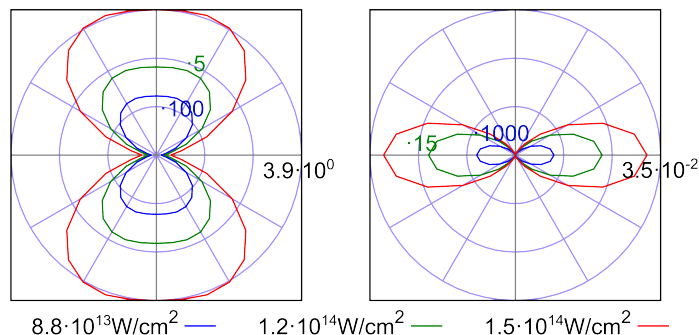


Figure V.3.10.: Comparison of the alignment dependence from  $\pi$ -type orbitals (left panel) and  $\sigma$  type orbitals (right panel) for different field intensities.

bital approach is the relative importance of the ionization from  $\sigma$  type orbitals, which is considerably smaller in the Dyson orbital approach. However, increasing the intensity in the Dyson orbital approach leads to a significant increase of the relative importance for ionization from the  $\sigma$  orbitals suggesting that this difference is mainly due to the different intensities used in the calculations (see Fig. V.3.10).

Overall, due to the small difference in the alignment dependence of the two approaches, the present calculations can be seen as confirmation of the TD-DFT results.

### V.3.3. Predicted yields assuming sequential ionization

In the previous sections, the alignment dependence of the population of two groups of states was investigated: a.)  ${}^3\Sigma_g^-$ ,  ${}^1\Delta_g$  and  ${}^1\Sigma_g^+$  and b.)  ${}^3\Pi_u$  and  ${}^1\Pi_u$ . Using the results from the TD-DFT calculations for the alignment dependency, the population of certain states will now be connected with the alignment dependent yields of the ionic channels,  $\text{C}_2\text{H}_2^+$  and  $\text{C}_2\text{H}_2^{2+}$  and the fragmentation channels  $\text{C}_2\text{H}^+ + \text{H}^+$ ,  $\text{CH}_2^+ + \text{C}^+$  and  $\text{CH}^+ + \text{CH}^+$ .

As established in part IV.3, the dicationic groundstate,  ${}^3\Sigma_g$ , of  $\text{C}_2\text{H}_2^{2+}$  is metastable. The first excited singlet states, the  ${}^1\Delta_g$  and the  ${}^1\Sigma_g^+$  state, also show a barrier to dissociation. A population of these states can thus be expected to lead to the detection of  $\text{C}_2\text{H}_2^{2+}$ . Therefore, the alignment dependent yield of  $\text{C}_2\text{H}_2^{2+}$  should be determined by the probability to remove two electrons from  $\pi_u$  orbitals (see also Fig. V.3.8).

To allow the comparison of this prediction with the experimental data, the alignment dependent ionization yield is convolved with the time-dependent angle distribution  $f(\theta, t)$  of a molecular rotational wavepacket [170]. The dynamics of the rotational wavepacket was thereby simulated assuming a polarizability orthogonal to the molecular axis of  $2.7 \text{ \AA}^3$ , an anisotropy of  $1.8 \text{ \AA}^3$  [171] and a rotational constant of  $B = 1.18 \text{ cm}^{-1}$  [172]. The initial rotational temperature was set to 100 K, equal to the value estimated from the experiment [47]. The intensity of the alignment pulse was set to  $2.4 \times 10^{13} \text{ W/cm}^2$  and the full-width at half maximum of the field to 50 fs similarly to the values from the experiment. With these parameters, the results for  $\langle \cos^2 \theta \rangle$  are very similar to those measured in the experiment (see Fig. V.2.1).

Using Eq.(V.3.4), the resulting normalized prediction  $Y_{\pi,\pi}(t)$

$$Y_{\pi,\pi}(t) = \frac{\int d\theta f(\theta, t) p_{\pi,\pi}^{2+}(\theta)}{\int dt \int d\theta f(\theta, t) p_{\pi,\pi}^{2+}(\theta)} \quad (\text{V.3.9})$$

for the delay-dependent yield of  $C_2H_2^{2+}$  is shown in Fig. V.3.11 together with the experimental results. As can be seen from Fig. V.3.11.a, very good qualitative and quantitative

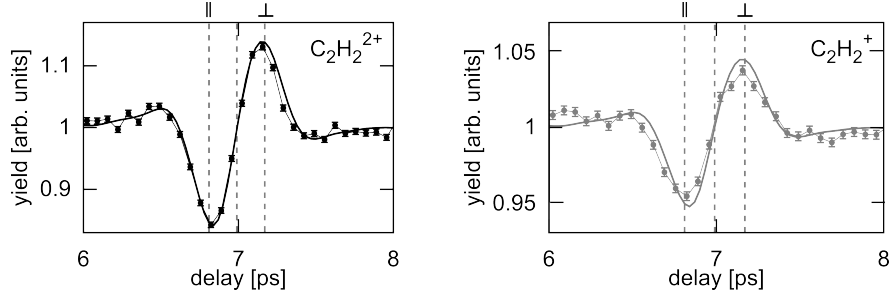


Figure V.3.11.: Comparison of the theoretically predicted delay dependence of the yield with experimental results. Left: For  $C_2H_2^{2+}$  assuming sequential double ionization from two  $\pi$  orbitals; right: for  $C_2H_2^+$  assuming single ionization from one  $\pi$  orbital.

agreement between the model predictions and the experimental results for the delay dependent yield of  $C_2H_2^{2+}$  is found. Similarly good agreement is also found for the yield of  $C_2H_2^+$  (see Fig. V.3.11.b), when assuming that the cation is produced by single ionization from a  $\pi$  orbital from acetylene. Note that no fitting parameters were used in this procedure: the bold lines in Fig. V.3.11 are the direct result of the model presented.

The second group of states analysed in the last section, the  $^3\Pi_u$  and  $^1\Pi_u$  states, have been shown in section IV.3 to be strongly dissociative along the CH stretching mode (see also Fig. V.3.8). Population of the  $\Pi_u$  states may thus be expected to lead to the

detection of  $C_2H^+ + H^+$ . Defining

$$Y_{\pi,\sigma}(t) = \frac{\int d\theta f(\theta, t) p_{\pi,\sigma}^{2+}(\theta)}{\int dt \int d\theta f(\theta, t) p_{\pi,\sigma}^{2+}(\theta)} \quad (V.3.10)$$

$$Y_{\sigma,\pi}(t) = \frac{\int d\theta f(\theta, t) p_{\sigma,\pi}^{2+}(\theta)}{\int dt \int d\theta f(\theta, t) p_{\sigma,\pi}^{2+}(\theta)} \quad (V.3.11)$$

with the  $p_{a,b}$  given by Eq. (V.3.4), allows the comparison of the model predictions with the experimentally measured fragmentation yields. However, as shown in Fig. V.3.12, the yields  $Y_{\pi,\sigma}$  or  $Y_{\sigma,\pi}$  do not correctly reproduce the experimental results for the KER integrated yield of  $C_2H^+ + H^+$  and  $CH^+ + CH^+$ . On the other hand, the  $CH_2^+ + C^+$  chan-

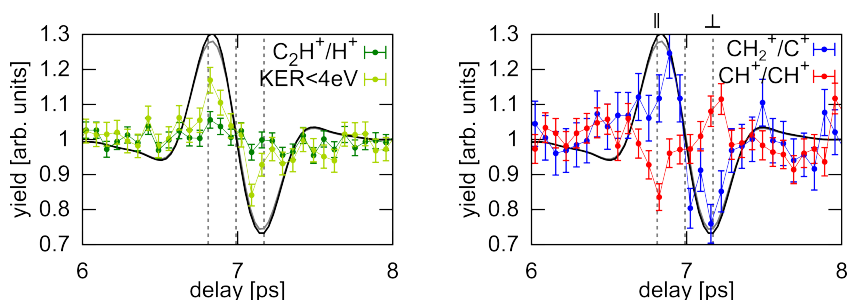


Figure V.3.12.: Comparison of the model results for sequential ionization from a  $\pi$  orbital followed by ionization from a  $\sigma$  orbital (black line) and vice versa (gray line) with experimental results of fragmentation yields.

nel shows good agreement with the model predictions. Considering the fact that the  $^3\Pi_u$  state is known to have a pathway to isomerization with energetically low lying transition states [173], this agreement does not come unexpectedly.

The disagreement of the yield of  $C_2H^+ + H^+$  with the model is less astonishing taking into account that the two distinct KER peaks observed for this channel (see Fig. V.2.3) and the opposite alignment behaviour of fragments with high and low KER suggest that at least two different reaction pathways participate in the reaction. In the following, only the low KER components will be associated to sequential ionization. This is motivated by the fact that the high KER components are strongly suppressed compared to the low KER part in circularly polarized light (see Fig. V.2.3), suggesting the influence of recollision to those events. Attributing only the low KER components of the  $C_2H^+ + H^+$  reaction to the population of the  $\Pi_u$  states via sequential ionization, a qualitative agreement between the experiment and the model is re-established. The overestimation of the modulation depth (compare the black and gray lines representing the model prediction with the green dots in Fig. V.3.12 for  $C_2H^+ + H^+$  with low KER) can be attributed to

the contribution of the second, recollision induced reaction channel to fragmentation products with low KER.

A similar interpretation can be invoked to account for the discrepancy observed between the model predictions and the  $CH^+ + CH^+$  yield (see right panel of Fig. V.3.12). Although the  $\Pi_u$  state can be expected to allow fragmentation into  $CH^+ + CH^+$ , the measured yield is clearly higher for preferentially orthogonal alignment, while, according to the model, sequential ionization to the  $\Pi_u$  states is favoured for parallel alignment. However, when using circularly polarized light, the experimentally measured delay dependent yield of  $CH^+ + CH^+$  is inverted, suggesting the influence of recollisional ionization in the case of linearly polarized light. For circularly polarized light, the experimental observations are correctly reproduced by the model as shown in the following.

To account for circularly polarized light, the present model is extended. The yield in circularly polarized light  $Y^{\text{circ.}}$  is calculated as

$$Y_{\pi,\sigma}^{\text{circ.}}(t) = \frac{\langle \int d\theta f(\theta, t) p_{\pi,\sigma}^{2+}(\alpha(\theta)) \rangle}{\int dt \langle \int d\theta f(\theta, t) p_{\pi,\sigma}^{2+}(\alpha(\theta)) \rangle}, \quad (\text{V.3.12})$$

where

$$\cos(\alpha(\theta)) = \cos(\beta) \sin(\gamma) \sin(\theta) + \sin(\beta) \cos(\theta). \quad (\text{V.3.13})$$

The average, denoted by the pointed brackets is taken over the angles  $\beta$  and  $\gamma$ . The angle  $\beta$  thereby describes the instantaneous polarization of  $\mathbf{E}(t)$  and  $\gamma$  is the azimuthal angle of the molecular axis relative to the polarization plane of the laser.

Using this equation, the measured delay-dependent yield of both the  $C_2H^+ + H^+$  and the  $CH^+ + CH^+$  fragmentation channel in circularly polarized light are reproduced qualitatively and quantitatively (see Fig. V.3.13). This excellent agreement corroborates the above interpretation. It can thus be concluded that a certain portion of the  $CH^+ + CH^+$  as well as the  $C_2H^+ + H^+$  fragments with  $KER \approx 3.5$  eV correspond to fragmentation from the  $^3\Pi_u$  or  $^1\Pi_u$  states after sequential ionization. This contradicts previous publications on experimental studies of electron impact and single photon ionization of  $C_2H_2$ , where  $C_2H^+ + H^+$  fragments with low KER of about 3.5 eV were attributed to dissociation from the  $^3\Sigma_g^-$  state [144, 174].

Since for both, the  $CH^+ + CH^+$  and the  $C_2H^+ + H^+$  fragmentation, recollisional ionization seems to play a major role at the experimentally relevant laser intensities, the alignment dependency of recollision induced fragmentation as well as the possible influence of field excitation is discussed in the following sections.

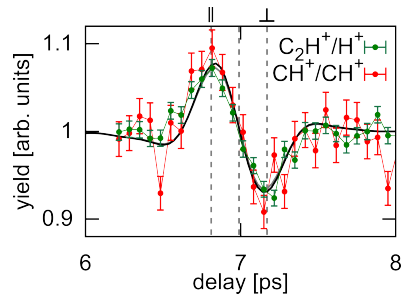


Figure V.3.13.: Comparison of the model results for sequential ionization from a  $\pi$  orbital followed by ionization from a  $\sigma$  orbital (black line) and vice versa (gray line) in circularly polarized light with experimental results of fragmentation yields.

## V.4. Alignment dependence of recollision events

The possibility that recollision induced molecular fragmentation may be alignment dependent was first proposed in Ref. [175], when studying the ellipticity dependence of non-sequential double ionization. The authors argued that the presence of a nodal plane in the wavefunction suppresses the probability for electrons to leave the molecule with zero transverse velocity. Within the strong-field approximation, only electrons with zero transverse velocity can return to the parent ion. Thus, recollisional ionization and subsequent fragmentation will be suppressed if the nodal plane lies in the laser polarization direction. Later, publications studying the alignment dependency of recollision in general, followed this line of argument, at the same time putting it onto more solid ground, using theoretical predictions for the momentum distribution of the primary electron after ionization based on tunnelling theory [29, 160, 176, 177].

Since the exact numerical treatment of recollisional ionization is highly challenging even for two electron systems due to the electron-electron interaction and the extensive grid sizes needed in the simulation, it is desirable to describe the process within simplified models. Invoking the three-step model [21], the alignment dependence of recollisional

ionization can be attributed to the alignment dependence of three processes: 1.) the probability to release a primary electron, 2.) the probability for this electron to return to the core and 3.) the probability for the recolliding electron to induce ionization upon impact.

While most publications studying the alignment dependence of recollisional ionization focus on the first and second step, the focus of this chapter lies on the third step, the alignment dependence of the recollision-induced ionization. The goal is thereby not to model the effect quantitatively; the intention of this analysis is rather to fathom whether one may expect an alignment dependency to arise due to this last step.

While not strictly speaking equivalent, the last step in recollisional ionization is closely related to electron impact ionization. At  $4 \times 10^{14}$  W/cm<sup>2</sup>, within the strong-field approximation, the maximum recollision energy  $\varepsilon = 3.17U_P$  for a classical electron (see Eq. I.2.10) is approximately 2.8 au = 75 eV. In terms of typical impact energies used in electron impact ionization experiments ((e,2e)-experiments), this is a very low energy. Only few studies have investigated the alignment dependence of electron impact ionization of molecules at low impact energies and most of the work done in this field has focused on H<sub>2</sub> [178, 179, 180, 181, 182, 183, 184, 185]. Most theoretical studies on the electron impact ionization of larger molecules (e.g. N<sub>2</sub>, H<sub>2</sub>O, NH<sub>3</sub>, CH<sub>4</sub>, pyrimidine) use orientation averaging when computing the cross-section, thereby reducing the numerical effort (e.g. [186, 187, 188, 189]). Furthermore, these studies focus in general on the triply-differential (i.e. momentum resolved) cross-section for arbitrary alignment and not the alignment dependent cross-section integrated over all momenta of the outgoing electrons relevant in the present case. In Ref. [180], the alignment dependence of the triply differential impact ionization cross-section of H<sub>2</sub> was studied, revealing a significant alignment dependence. Therefore, it remains an interesting question to investigate whether an alignment dependence is also present in the case of C<sub>2</sub>H<sub>2</sub> and whether it is present for electron impact ionization cross-sections integrated over all outgoing electron momenta.

This question will be analysed in the following section albeit without a claim for quantitative results. The aim is to assess whether this third step in recollisional ionization which is usually neglected when studying the alignment dependence of recollisional ionization can be rightly neglected or whether it may play a significant role.

### V.4.1. Alignment dependence of electron impact ionization

In order to assess whether electron impact ionization may be alignment dependent, to understand what may cause the alignment dependency and to gauge on which parameters it may be expected to depend, the simplest possible model will serve as first step:

In this model, it is assumed that the nuclear wavefunction is not affected during the impact, i.e. that the nuclei do not move, i.e. no vibrations are excited in the recollision. This can be expected to be a reasonable approximation since the ionization process occurs on timescales significantly smaller than the timescale of molecular vibration. Furthermore, the process is described as an effective two electron process, where the active electrons are the incoming electron and an electron situated in a Dyson orbital

$$\phi_D = \langle \psi^{N-2} | \psi^{N-1} \rangle, \quad (\text{V.4.1})$$

where  $\psi^{N-1}$  is the  $(N - 1)$ -particle electronic wavefunction of the ion corresponding to the molecular state prior to impact ionization and  $\psi^{N-2}$  is the  $(N - 2)$ -particle electronic wavefunction of the dication after impact ionization.

The outgoing electrons are assumed not to interact. Although the interaction of the two outgoing electrons in the continuum is known to be important for the correct description of the threefold differential cross-section [190], in the present application, the simplification is assumed to be valid, since the exact position of the binary and recoil peak are not important. The incident electron wave is represented as plane wave. Under these assumptions and neglecting exchange, the transition matrix element  $T$ , defining the triply-differential cross-section  $\frac{d^3\sigma}{d\Omega_1 d\Omega_2 dE_1} \propto \frac{k_s k_e}{k_i} |T_{if}|^2 \delta(E_f - E_i)$ , is given by

$$T_{if} = \langle \psi_{\mathbf{k}_e}^-(\mathbf{r}_1) \psi_{\mathbf{k}_s}^-(\mathbf{r}_2) | V_i(\mathbf{r}_1, \mathbf{r}_2) | \phi_D(\mathbf{r}_1) e^{i\mathbf{k}_i \mathbf{r}_2} \rangle, \quad (\text{V.4.2})$$

where the  $\psi^-$  are scattering solutions with outgoing boundary condition for the effective potential  $V_i$

$$V_i(\mathbf{r}_1, \mathbf{r}_2) \approx V_{\text{ion}}(r_2) + \frac{1}{|\mathbf{r}_1 - \mathbf{r}_2|}. \quad (\text{V.4.3})$$

The effective ion potential  $V_{\text{ion}}$  is dropped from  $V_i$  in the expression of the transition matrix element, since a single particle potential cannot induce a two particle transition.

Even with the above simplifications, the description of the  $\psi^-$  remains a challenge: While the incoming electron has an energy around 2.5 au, the outgoing electrons are considerably slower due to the ionization potential around 1 au. Especially the slower



of the two outgoing electrons can be expected to have a very low velocity, since the transition matrix element is larger for low energy transfers [95]. The emitted electron will hence not be well described within the first Born approximation. To allow a first appraisal, the scattered wave, i.e. the faster electron, will be described by a plane wave, while the emitted wave, i.e. the slower electron, will be described by a Coulomb scattering wave function  $\chi_C^-$ . Asymptotically, at large distances from the ion, the Coulomb potential has the same form as  $V_{\text{ion}}$ , but the simple approximation does not account for the multi-center nature of the molecular potential and will overestimate the influence of the potential near the center since the inner electrons shield the nuclear charges in the molecule.

Since exchange plays a minor role for unequal energy sharing [95], it will be neglected in the first step. Under these assumptions, the approximate triply differential scattering cross-section is defined via the following transition matrix element  $T_{if}$

$$T_{if} \propto \frac{4\pi}{|\mathbf{k}_i - \mathbf{k}_s|^2} \langle \chi_C^-(\mathbf{k}_e, \mathbf{r}_1) | e^{i(\mathbf{k}_i - \mathbf{k}_s)\mathbf{r}_1} | \phi_D(\mathbf{r}_1) \rangle, \quad (\text{V.4.4})$$

where  $\mathbf{k}_i$ ,  $\mathbf{k}_s$  and  $\mathbf{k}_e$  are the momenta of the incoming, the scattered and the emitted electron respectively. The wavefunction  $\chi_C^-$ , the Coulomb scattering wave with outgoing boundary conditions, is given by [95]

$$\chi_C^-(\mathbf{k}_e, \mathbf{r}) = \frac{1}{(2\pi)^{-\frac{3}{2}}} e^{-\frac{1}{2}\pi\eta} \Gamma(1 - i\eta) e^{i\mathbf{k}\mathbf{r}} {}_1F_1[i\eta, 1, -i(kr - \mathbf{k}\mathbf{r})], \quad (\text{V.4.5})$$

where  $\Gamma$  is the Gamma function for complex arguments,  ${}_1F_1[a, b, c]$  is the confluent hypergeometric function and  $\eta = -Z/k$ . Since the molecule is doubly charged after the recollisional ionization  $Z = 2$ .

The expression in Eq. (V.4.4) is equivalent to the Fourier transform of  $\langle \phi_C^-(\mathbf{k}_e, \mathbf{r}) | \phi_D(\mathbf{r}) \rangle$  evaluated at the q-vector  $\mathbf{q} = \mathbf{k}_i - \mathbf{k}_s$  and weighted by the inverse q-vector squared. The only information on the molecular properties enters via the Dyson orbital  $\phi_D$ . To analyse how the properties of  $\phi_D$  influence the resulting electron impact cross-section, Figs. V.4.1 and V.4.2 show the Fourier transform of the matrix element  $\langle \phi_C^-(\mathbf{k}_e, \mathbf{r}) | \phi_D(\mathbf{r}) \rangle$  for two Dyson orbitals with different symmetry: the  $\pi_u$ -type Dyson orbital corresponding to ionization to the dicationic  ${}^2\Sigma_g^-$  groundstate and the  $\sigma_g$ -type Dyson orbital corresponding to ionization to the dissociative  ${}^3\Pi_u$  state (see Tab. V.3.2). The energy of the outgoing electron was set to  $E_e = 0.2\text{ eV}$ ; the cases in panels a.) to c.) correspond to different angles of the outgoing electron relative to the molecular axis. The orbital shape is clearly

reflected in the Fourier transforms; the product with the outgoing wave manifests in the shift in  $k$ -space and a distortion compared to the Fourier transform of the orbital itself (compare panels a. to c. with panel e.).

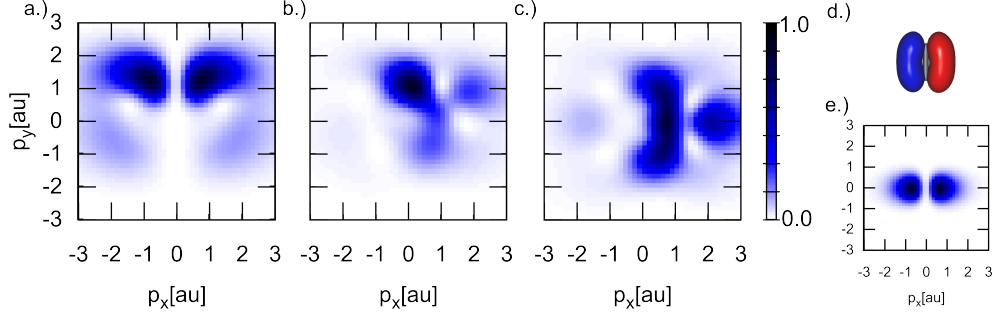


Figure V.4.1.: Absolute square value of the Fourier transform of  $\langle \phi_C^-(\mathbf{k}_e, \mathbf{r}) | \phi_D(\mathbf{r}) \rangle$  for the  $\pi_u$ -type Dyson orbital (shown in panel d.) for different angles of  $\mathbf{k}_e$ : a.) parallel to the molecular axis, b.)  $45^\circ$ , c.) orthogonal ( $E_e = 0.2$  au), e.) Fourier transform of the Dyson orbital itself. The molecular axis lies along the  $y$ -direction. Different points on the plots correspond to different values of  $\mathbf{q} = \mathbf{k}_i - \mathbf{k}_s$ . The absolute square of  $\mathcal{F}(\langle \phi_C^-(\mathbf{k}_e, \mathbf{r}) | \phi_D(\mathbf{r}) \rangle) |_{\mathbf{k}_i - \mathbf{k}_s}$  is proportional to the triply differential cross-section.

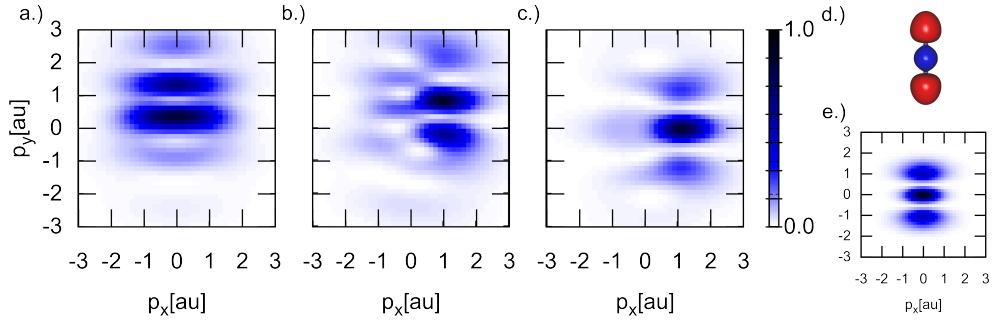


Figure V.4.2.: As Fig. V.4.1 for the  $\sigma_g$ -type Dyson orbital.

To study the resulting alignment dependence of the triply differential, alignment dependent cross-section, let us assume that the momentum of the incident electron, impinging on the  $\pi_u$ -type orbital, is parallel to the momentum of both outgoing electrons, with  $q = 1$  au. For electron impact parallel to the molecular axis, the triply differential cross-section is then proportional to the value at  $(0, 1)$  in Fig. V.4.1a), while the value at  $(1, 0)$  in Fig. V.4.1c) corresponds to perpendicular alignment. These two values are clearly different, reflecting the alignment sensitivity of the triply differential cross-section.

If only the alignment dependent ionization yield is of interest and not the direction

of the outgoing electrons after impact ionization, an average has to be taken over the momentum direction of both outgoing electrons ( $\Omega_s$  and  $\Omega_e$ ) and over the energy sharing of the two electrons. It is not a priori clear whether the alignment dependence of the triply-differential cross-section will wash out due to averaging or not.

First, the averaging over  $\Omega_s$  and  $\Omega_e$  will be considered. To this end the energy of the incoming electron is set to  $2.5 \text{ au} \approx 65 \text{ eV}$ , which is slightly lower than the maximum recollision energy expected at an intensity of  $4 \times 10^{14} \text{ W/cm}^2$ . The energy  $E_e$  of the slower electron, i.e. the electron emitted from the ion if exchange is neglected, is set to  $0.2 \text{ au} \approx 5.4 \text{ eV}$ . Energy conservation is taken into account by setting  $E_i = E_e + E_s + I_P$ <sup>1</sup>, where  $E_i$ ,  $E_e$  and  $E_s$  are the energies of the incident, emitted and scattered electron respectively and  $I_P$  is the ionization potential. The resulting alignment dependence of the singly-differential cross-section  $\frac{d\sigma}{dE_e}(\theta)$  is shown in Fig. V.4.3 as a function of the relative alignment angle  $\theta$  between the molecular axis and the electron impact direction. These graphs show a pronounced alignment dependence in the case of the  $\sigma_g$  orbital, while the alignment dependence of the singly-differential cross-section for the  $\pi_u$  orbital is negligible.

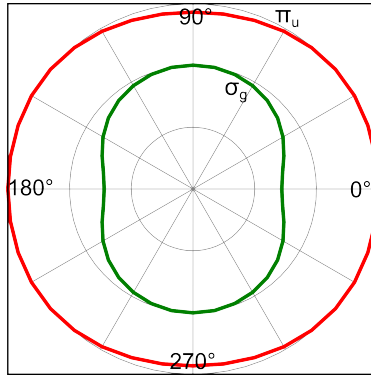


Figure V.4.3.: Singly-differential cross-section  $\frac{d\sigma}{dE_e}(\theta)$  [arb. u.] for electron impact ionization from the  $\pi_u$  Dyson orbital (red line) and the  $\sigma_g$  Dyson orbital (green line) as function of the relative alignment angle  $\theta$  between the direction of the incident electrons and the molecular axis ( $0^\circ$ : parallel to the molecular axis,  $90^\circ$ : perpendicular). In the case of the  $\pi_u$  orbital, the plane of incidence is equal to the orbital plane. ( $E_i = 2.5 \text{ au}$ ,  $E_e = 0.2 \text{ au}$ ).

In the next step, the dependence on the energy sharing will be investigated. Fig. V.4.4 shows the singly-differential cross-section for the  $\pi_u$  and  $\sigma_g$  Dyson orbitals for different

<sup>1</sup>In this expression, the momentum transfer to the nucleus, which is necessary due to momentum conservation is neglected.

values of  $E_e$ . As expected, the singly-differential cross-section is larger for small values of  $E_e$ , but while the magnitude of the singly-differential cross-section is energy dependent, the qualitative alignment dependence seems to be unaffected over a comparatively wide range of different energy sharing. One of the reasons for this insensitivity to  $E_e = \frac{k_e^2}{2m}$  may be the comparative insensitivity of the Coulomb scattering wave on the asymptotic momentum  $\mathbf{k}_e$  near the vicinity of the core. Overall, the stability of the alignment dependence with  $E_e$  suggests that the the cross-section will show a significant alignment dependence in the case of the  $\sigma_g$ -type Dyson orbital even if integrated over  $E_e$ .

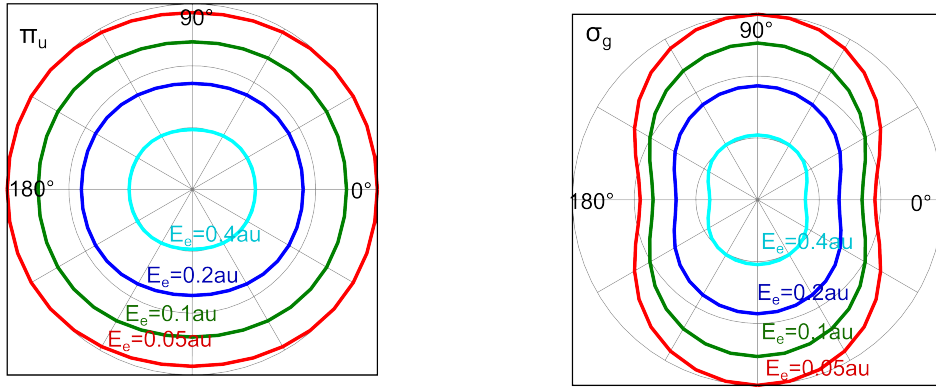


Figure V.4.4.: Dependence of the singly-differential cross-section [arb. u.] for ionization from the  $\pi_u$ -type Dyson orbital (left panel) and the  $\sigma_g$ -typen Dyson orbital (right panel) on the energy sharing. ( $E_i = 2.5$  au)

So far, the molecular nature only entered the problem via the Dyson orbital; an influence of the molecular structure on the scattering wave has been so far neglected. If the molecular structure is taken into account, may this diminish the observed alignment dependence — may it enhance it? To tackle this question, a simple model for a multi-center scattering wave was devised. In this model, the outgoing wavefunction of the emitted electron, which was so far described by a Coulomb wavefunction, is replaced by

$$\chi_{2C}^-(\mathbf{k}, \mathbf{r}) = -e^{i\mathbf{k}\mathbf{r}} + e^{i\mathbf{k}\mathbf{\Delta}} \chi_{C,\mathbf{k}}^-(\mathbf{r} - \mathbf{\Delta}) + e^{-i\mathbf{k}\mathbf{\Delta}} \chi_{C,\mathbf{k}}^-(\mathbf{r} + \mathbf{\Delta}). \quad (\text{V.4.6})$$

This expression follows in first order from the Lippmann-Schwinger equation for a two center potential  $V(\mathbf{r}) = V_l(\mathbf{r}) + V_r(\mathbf{r}) = -\frac{1}{|\mathbf{r}-\mathbf{\Delta}|} - \frac{1}{|\mathbf{r}+\mathbf{\Delta}|}$ , where  $2\mathbf{\Delta}$  is the distance between the two cores. The derivation is given in Appendix C. However, since the terms depending on both  $V_l$  and  $V_r$  are neglected in the derivation, Eq. V.4.6 does not converge to the correct solution for  $\mathbf{\Delta} \rightarrow 0$  and will only be a good approximation for

large enough internuclear separations. In the following,  $2\Delta$  is set to  $1.2 \text{ \AA}$ , corresponding approximately to the C-C distance in the neutral acetylene groundstate. Fig. V.4.5 shows the resulting singly-differential cross-section for the  $\pi_u$  and the  $\pi_g$  Dyson orbital at  $E_e = 0.2 \text{ au}$ . Especially in the case of the  $\sigma_g$ -type Dyson orbital, at  $E_e = 0.2 \text{ au}$ , the two-center wavefunction leads to a significant change of the alignment dependence compared to the results for a single-center Coulomb wave (albeit with a considerable dependence on  $E_e$  in the case of the  $\sigma_g$ -type orbital)

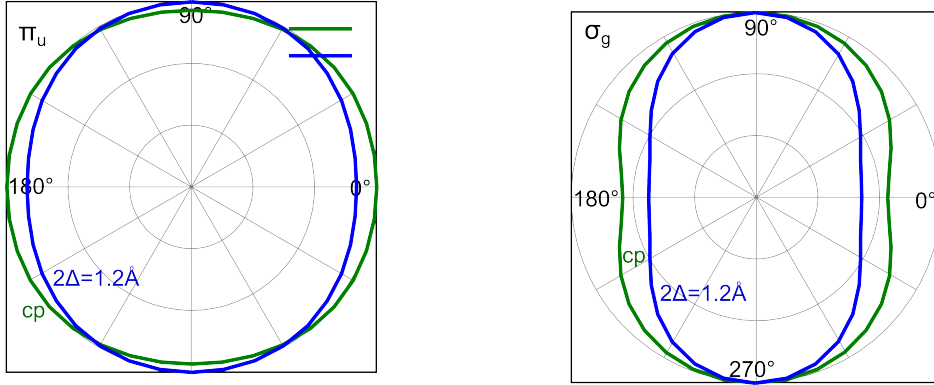


Figure V.4.5.: Dependence of the singly-differential cross-section [arb. u.] on the form of the emitted electron wave for the  $\pi_u$ -type Dyson orbital (left panel) and the  $\sigma_g$ -type Dyson orbital (right panel). Green line: single center coulomb wave (cp); blue line: multi-center wave for an internuclear distance of  $2\Delta = 1.2 \text{ \AA}$ . The cross-sections are independently scaled to their maximum. ( $E_i = 2.5 \text{ au}$ ,  $E_e = 0.2 \text{ au}$ )

Although neither the single-center, nor the multi-center Coulomb wave correspond to the exact scattering wave function, the results presented allow establishing three facts: 1.) the alignment dependence will depend on the initial and final state, i.e. on the Dyson orbital, 2.) the ionization cross-section may well be alignment dependent, in spite of the averaging over the direction of the outgoing electrons and the energy sharing and 3) the alignment dependence depends sensitively on the correct description of the (slower) outgoing wave.

Describing the faster outgoing wave and the incoming wave as plane waves, is numerically advantageous, since it allows performing the integral in the transition matrix over the coordinates of one of the electrons analytically. However, as established before, the alignment dependence of the impact-cross section will depend strongly on the description of the slower outgoing wave. In spite of the fact that the incident and scattered electron will be faster than the emitted electron, the correct description of these two waves may well be of importance. To asses the possible influence, two more models were applied:

In the first model (denoted by *cc* in the following), the transition matrix element is approximated as

$$T_{if} \propto \langle \chi_C^-(\mathbf{k}_e, \mathbf{r}_2) \chi_C^-(\mathbf{k}_s, \mathbf{r}_1) | V_{\text{int}} | \phi_D(\mathbf{r}_1) e^{i\mathbf{k}_i \cdot \mathbf{r}_2} \rangle \quad (\text{V.4.7})$$

This corresponds to assuming that both scattered waves can be represented approximately as single-center Coulomb waves. Although the fact that the multi-center nature of the emitted wave has an influence on the cross-section was established before, the present calculations aim solely at inferring whether the exact description of the faster scattering wave also has an influence, the multi-center nature of the wave function is therefore neglected for simplicity.

Eq. V.4.7 contains the integrals over the coordinates  $\mathbf{r}_1$  and  $\mathbf{r}_2$ . Performing these integrals on a grid would be numerically prohibitive. Therefore, an expansion in spherical harmonics  $Y_{l,m}$  was used. This leads to the following expression for the singly-differential cross-section (for a derivation see Appendix D)

$$\begin{aligned} \frac{d\sigma}{dE_e} \propto \frac{1}{k_i k_e k_s} \sum_{l_e, m_e, l_s, m_s} \left| \sum_{\alpha, l, l_i} \frac{1}{2l+1} i^{(l_i)} Y_{l, -m_i}(\hat{\mathbf{k}}_i) \right. \\ \left[ G_{-m_s, m, m_i}^{l_s, l, l_i} G_{-m_e, -m, m_\alpha}^{l_e, l, l_\alpha} \int \int \frac{r_{<}^{l+1}}{r_{>}^l} f_\alpha(r') j_{l_i}(k_i r) F_{l_e}^*(\eta_e, k_e r') F_{l_s}^*(\eta_s, k_s r) dr dr' \right. \\ \left. \mp G_{-m_s, \tilde{m}, m_i}^{l_s, l, l_i} G_{-m_e, -\tilde{m}, m_\alpha}^{l_e, l, l_\alpha} \int \int \frac{r_{<}^{l+1}}{r_{>}^l} f_\alpha(r') j_{l_i}(k_i r) F_{l_s}^*(\eta_s, k_s r') F_{l_e}^*(\eta_e, k_e r) dr dr' \right] \Big|^2, \end{aligned} \quad (\text{V.4.8})$$

where the plus sign corresponds to an anti-symmetric spin function, whereas the minus sign should be chosen if the spin function is symmetric. Neglecting the second term entirely, is equivalent to neglecting exchange. The variables  $m_i$ ,  $m$  and  $\tilde{m}$  are given by  $m_i = (m_s - m_e - m_\alpha)$ ,  $m = (m_\alpha - m_e)$  and  $\tilde{m} = (m_\alpha - m_s)$  and  $r_{< / >}$  denote the smaller/larger of  $r$  and  $r'$ . The  $G$  denote Gaunt coefficients are given by

$$G_{m_1, m_2, m_3}^{l_1, l_2, l_3} = \sqrt{\frac{(2l_1+1)(2l_2+1)(2l_3+1)}{4\pi}} \begin{pmatrix} l_1 & l_2 & l_3 \\ 0 & 0 & 0 \end{pmatrix} \begin{pmatrix} l_1 & l_2 & l_3 \\ m_1 & m_2 & m_3 \end{pmatrix}, \quad (\text{V.4.9})$$

where the expressions in brackets are the Wigner-3j symbols. The function  $f_\alpha(r)$  describes the radial part of the Dyson orbital and is defined via

$$f_\alpha(r) = \int d\Omega \phi_D^*(\mathbf{r}) Y_{l_\alpha, m_\alpha}(\hat{\mathbf{r}}) \quad (\text{V.4.10})$$

The regular Coulomb functions  $F_l(\eta, \rho)$  are the radial functions of the Coulomb scattering wave [191].

The second method, denoted by *ccc* in the following, results from the distorted Born approximation, when assuming that  $V_{\text{ion}}$  is given by  $-\frac{2}{r}$ . Under this approximation (for a derivation see Appendix E), all outgoing and the incoming wave are represented as Coulomb waves and the singly differential cross section is given by

$$\frac{d\sigma}{dE_e} \propto \frac{1}{k_i k_e k_s} \sum_{l_e, m_e, l_s, m_s} \left| \sum_{\alpha, l, l_i} \frac{1}{2l+1} i^{(l_i)} Y_{l_i, -m_i}(\hat{\mathbf{k}}_i) \left[ G_{-m_s, m, m_i}^{l_s, l, l_i} G_{-m_e, -m, m_\alpha}^{l_e, l, l_\alpha} \cdot \int \int \frac{r'^{l+1}}{r'^l} f_\alpha(r') F_{l_i}(\eta_i, k_i r) \frac{e^{i\sigma_l(\eta_i)}}{k_i r} F_{l_e}^*(\eta_e, k_e r') F_{l_s}^*(\eta_s, k_s r) dr dr' \right] \right|^2, \quad (\text{V.4.11})$$

when exchange is neglected.

The resulting singly-differential cross-sections  $\frac{d\sigma}{dE_e}(\theta)$  are shown in Fig. V.4.6 for  $E_e = 0.2$  au and  $E_i = 2.5$  au in comparison with the previous results, describing the scattered wave as plane wave (*pc*) for the  $\pi_u$ -type Dyson orbital (left panel) and the  $\sigma_g$ -type Dyson orbital (right panel).

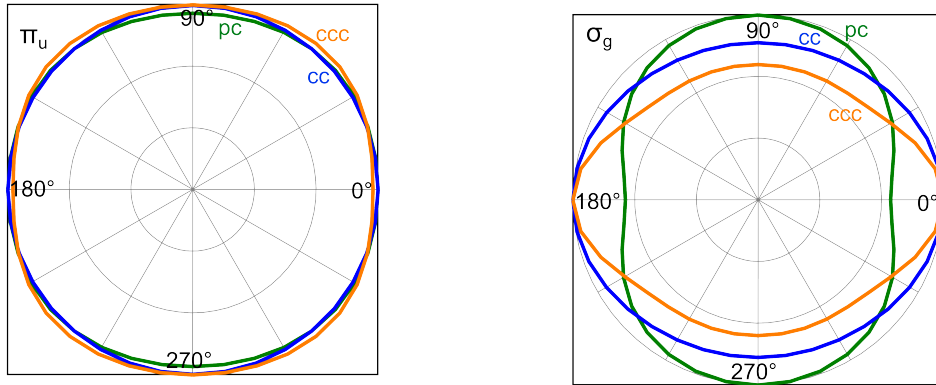


Figure V.4.6.: Comparison of the singly-differential cross-section  $\frac{d\sigma}{dE_e}(\theta)$  using different models (*pc*, *cc* and *ccc* — for details refer to the text) for the  $\pi_u$ -type Dyson orbital (left panel) and the  $\sigma_g$ -type Dyson orbital (right panel). The cross-sections are independently scaled to their maximum. ( $E_i = 2.5$  au,  $E_e = 0.2$  au).

While, for the  $\pi_u$ -type Dyson orbital, the cross-section shows only a weak alignment dependence which does not depend strongly on the model, the alignment dependence of the singly-differential cross-section for the  $\sigma_g$  Dyson orbital changes drastically with the exact description of the wave. For both orbitals and the three methods compared in

Fig. V.4.6, the alignment dependence of the singly-differential cross-section  $\frac{d\sigma}{dE_e}(\theta)$  does not change strongly with the energy sharing (not shown) and can thus serve as estimate for the cross-section  $\sigma(\theta)$  integrated over energy sharing.

The strong dependence of the results on the exact model used shows clearly that for typical impact energies present in recollisional ionization, a correct description, not only of the slower, emitted wave would be needed, but also for faster, scattered wave. Moreover, although the influence of exchange diminishes for smaller  $E_e$ , it influences the resulting singly-differential cross-section strongly even at comparatively low energy transfers of  $E_e = 0.2$  au as shown in Fig. V.4.7.

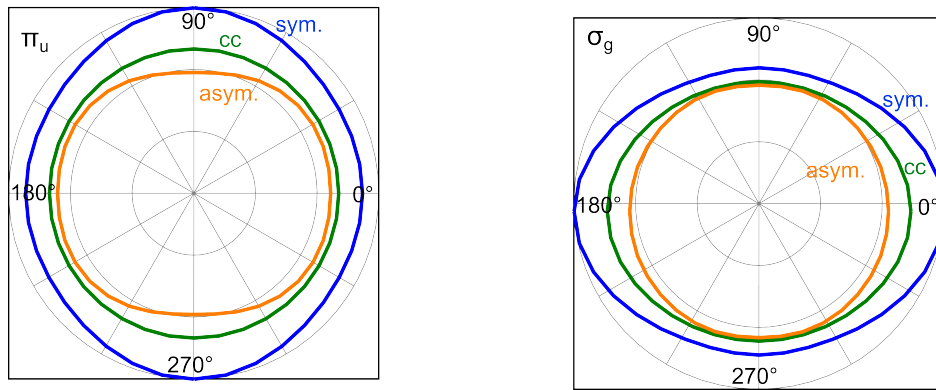


Figure V.4.7.: Comparison of the singly-differential cross-section using the *cc* model (for details refer to the text) when neglecting exchange (green line), when using an antisymmetric spacial wavefunction (orange line) and when using a symmetric spacial wave function (blue line) for the  $\pi_u$ -type Dyson orbital (left panel) and the  $\sigma_g$ -type Dyson orbital (right panel). ( $E_i = 2.5$  au,  $E_e = 0.2$  au).

## V.4.2. Conclusion

In conclusion, it has been shown that electron impact ionization of acetylene may be strongly alignment dependent. The Coulomb waves, used to represent the scattering waves in the present model, are only an approximation to the true scattering waves, which depend on a spherically non-symmetric, multi-center potential and the models used cannot give an quantitatively accurate description of the rescattering process. Never the less, the results do suggest that orbital symmetry induces an alignment sensitivity in the recollision induced impact ionization cross-section  $\sigma(\theta)$ : while the alignment dependence of the ionization cross-section from the  $\pi_u$  type Dyson orbital seems to be small, the



impact ionization cross-section from the  $\sigma_g$ -type Dyson orbital shows a strong alignment dependence in spite of the averaging over the direction of the outgoing electron momenta and the energy sharing.

In a complete description of the rescattering process, the alignment dependence of 1.) the initial ionization, 2.) the probability for the primary electron to return to the core and 3.) the probability for impact ionization should therefore be included. However, a correct description of the cross-section will remain a challenge: on the one hand, this is due to the fact that (e,2e) cross-sections are not totally equivalent to the recollision step since in (e,2e) processes no field is present and the incoming electron wave is not shaped by the previous ionization step and field-propagation. On the other hand, it could be shown that the exact form of the outgoing and incoming scattering waves are very important for a correct description of the alignment dependence. It is, however, so far numerically prohibitive to calculate the exact scattering wave function in an arbitrary 3D potential. The cross-section can thus not even be calculated exactly within a two-active-electron approximation. It will remain a challenge to identify those approximations that reflect the physical process best.

## V.5. Field Excitation

So far, only cases were considered, where ionization directly determines the final electronic state populated in the dication. However, field excitations, i.e. dipole transitions between different electronic states, may also have an influence on the process. Field excitation may occur in the neutral before ionization, in the cation after the first ionization step or in the dication. Due to the alignment dependence of the transition moments, the population of excited states via field excitation can be expected to show a strong alignment dependence.

The energy gap to the first excited dipole coupled state in the Franck-Condon region is similar in the neutral, the cation and the dication. It is therefore likely that the average probability for field excitation is similar in all three cases. In the following, an analysis of the field excitation process in the dication is presented. To this end, the molecular dynamics on the four strongest dipole coupled triplet states of the dication are considered

in reduced dimensions. The states considered are the  $^3\Sigma_g^-$  groundstate ( $V_1$  in Fig. V.5.1), the first and the second excited states, which are the  $^3\Pi_u$  and  $^3\Pi_g$  states ( $V_2$  and  $V_3$  in Fig. V.5.1), and one higher excited state, the first  $^3\Sigma_u^-$  state ( $V_4$  in Fig. V.5.1). Since the potential energy surfaces of the singlet states behave qualitatively similarly to the singlet states, the calculations were not repeated for the singlet states. The nuclear degrees of freedom used in the calculation are the two C-H stretching modes, which correspond to the fastest vibrational modes of acetylene. The C-C stretching mode is not taken into account due to the much slower molecular motion along this coordinate compared to the C-H stretching mode.

The electronic states and the transition dipole moments shown in Fig. V.5.1 were calculated in the  $C_{2v}$  point group using a state averaged CAS(8,8) and a subsequent MRCI calculation. Only the strongest dipole couplings, shown in Fig. V.5.1, were taken into account.

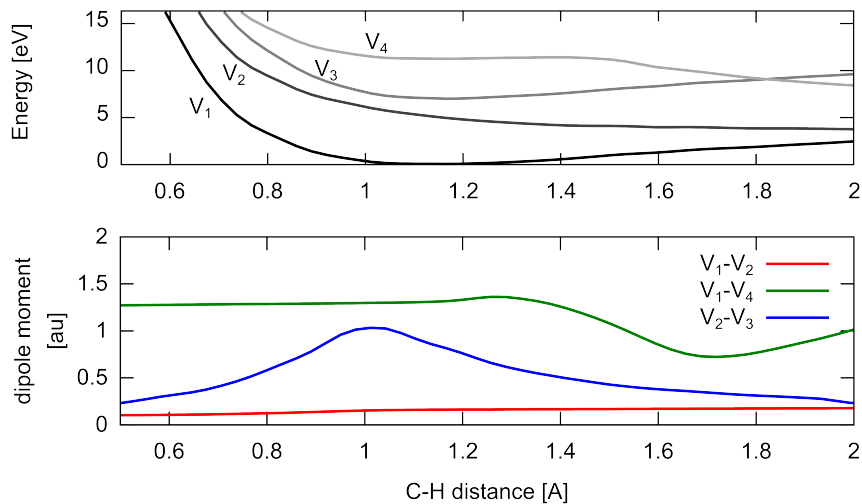


Figure V.5.1.: Cut through the potential surface and the dipole couplings considered in the dynamics calculations along one of the C-H stretching modes (the other C-H distance is kept fixed at 1 Å).

Mimicking a Franck-Condon like ionization behaviour, the nuclear wavepacket of the neutral groundstate is used as initial wavepacket on the dicationic groundstate. Since the molecule has to be doubly ionized prior to the field excitation in the dication, the propagation was started at different moments during the temporal extent of the laser pulse and the lowest lying light induced potential was considered as groundstate. The probe pulse was set to an intensity of  $I = 4 \times 10^{14} \text{ W/cm}^2$  and a duration of 4.5 fs,

similar to the values used in the experiment.

Figures V.5.2 to V.5.4 show the resulting fragmentation probability as a function of the moment of ionization for different values of the carrier-envelope phase (CEP) and different alignment angle  $\theta$  of the molecule relative to the laser polarization axis.

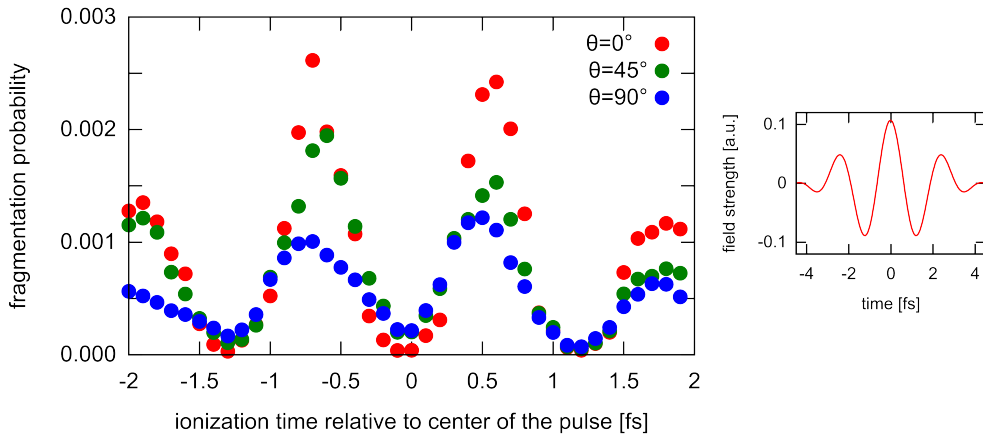


Figure V.5.2.: Fragmentation probability as a function of the moment of double ionization, with  $t = 0$  fs corresponding to the center of the pulse for a pulse with CEP =  $0^\circ$ .

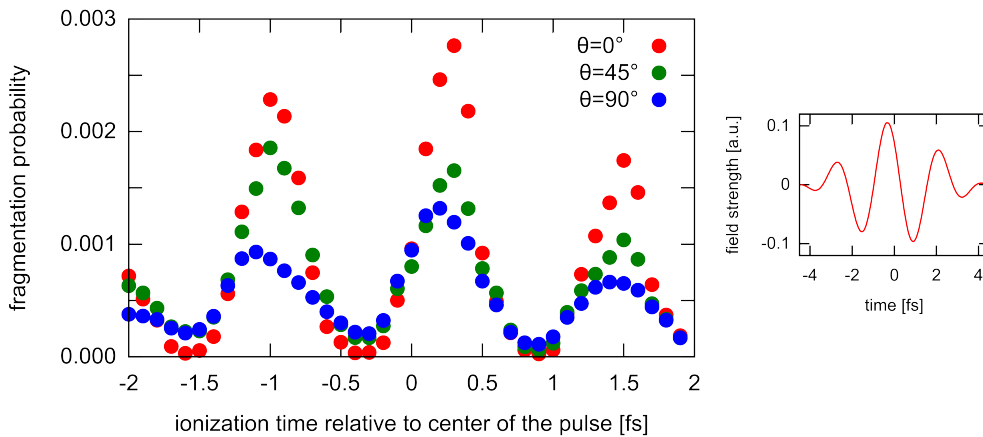


Figure V.5.3.: As Fig. V.5.2 for CEP =  $45^\circ$ .

Independently of the CEP, the fragmentation probability strongly depends on the molecular alignment. The relative fragmentation probability thereby also depends on the moment of ionization: considering Fig. V.5.2, field excitation induced fragmentation is larger for parallel alignment than for perpendicular alignment, if ionization happens at  $t \approx 0.6$  fs, corresponding to a zero electric field, where the probability for recollisional

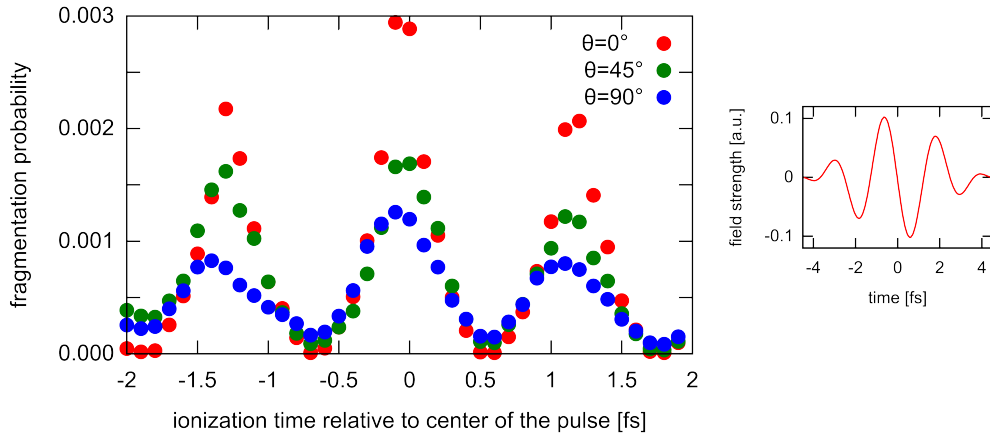


Figure V.5.4.: As Fig. V.5.2 for CEP = 90°.

ionization is high. At the field maximum ( $t = 0$  fs), when the probability for sequential ionization is highest, the fragmentation probability is higher for perpendicular alignment. However, as can be seen in Figs. V.5.2 to V.5.4, the overall probability for fragmentation due to field excitation in the dication is below 0.3%. Yet, in the experiment the ratio of the yield of the  $C_2H^+ + H^+$  channel to the yield of  $C_2H_2^{2+}$  is larger than 6%. The present calculations for a field excitation process would therefore underestimate the actual fragmentation probability by a factor of more than 20. Since the energy gap to the lowest dipole coupled states is similarly high in the neutral and the cation as in the case of the dication discussed here, it can be expected that the probability for field excitation in the neutral and the cation will be similarly low. This strongly suggests that field excitation cannot be the dominant process leading to the alignment sensitivity of the fragmentation process. It can therefore be concluded that, while the field excitation process is strongly alignment dependent, the alignment dependence of the measured yields are dominated by the alignment dependence of sequential and recollisional ionization.

## V.6. Conclusion

In this chapter, the mechanisms allowing to control the channel dependent yield of fragmentation reactions of  $C_2H_2^{2+}$  were studied. First, the alignment dependence of sequential ionization was studied using a TD-DFT and an effective single-active electron tunnel-ionization model. The comparison of the two methods showed consistent results, thereby backing up the TD-DFT results which were used to model the alignment dependent yield of the different fragmentation channels. Within the model for sequential ionization, the yield of the  $C_2H_2^+$ ,  $C_2H_2^{2+}$  and the  $CH_2^+ + C^+$  channel could be reproduced both, qualitatively and quantitatively. For the  $C_2H^+ + H^+$  and the  $CH^+ + CH^+$  channel, the influence of recollisional ionization to the total fragmentation yield is important and the experimental observations could only be reproduced for circularly polarized light, due to the fact that the alignment dependency of recollisional ionization can — so far — not be modelled.

In the second part the problem of recollisional ionization was addressed. It was thereby not the goal to investigate the process quantitatively, it was rather the goal to investigate whether the impact ionization, which is generally neglected when studying the alignment dependence of recollisional ionization, introduces an additional alignment dependence. While the alignment dependence of the electron impact ionization cross-section in  $C_2H_2^+$ , was found to be small in the case of ionization from a  $\pi_u$  Dyson orbital, for  $\sigma_g$  type orbitals, the calculations suggest a significant alignment dependence. Thus, the alignment dependence of electron-impact ionization should be taken into account when studying recollisional ionization.

The third part addressed the alignment dependence of field driven dipole excitations. While the field excitation shows a strong alignment dependence, its overall importance is negligible due to the small field excitation probability.



## Part VI.

# Summary and Conclusion

In this work, the complex molecular dynamics driven by strong, few-cycle infra-red laser pulses with intensities around  $10^{14}$  W/cm<sup>2</sup> and pulse lengths below 5 fs have been analysed. With the help of theoretical investigations and numerical modelling insight could be provided to the physical mechanisms governing the strong-field dynamics of electrons and nuclei and the interplay between inter-particle and laser-particle interaction. The complexity of the systems studied ranged from the simplest of molecules, H<sub>2</sub><sup>+</sup>, up to acetylene, C<sub>2</sub>H<sub>2</sub>, a small hydrocarbon.

In the first part of this work, the photoelectron spectrum of H<sub>2</sub><sup>+</sup> subject to intense circularly polarized infra-red fields was investigated. Experimentally, it has been observed in the group of P. Corkum [Spanner et al. J. Phys. B, 194011, (2012)] that the photoelectron momentum distribution is rotated in circularly polarized fields relatively to the expectations from the strong-field approximation. This rotation is comparatively stable against an increase of the laser intensity — a counterintuitive fact, since one would expect the results from the strong-field approximation to be recovered for high intensities. Although the numerical solution of the time-dependent Schrödinger equation may be possible for H<sub>2</sub><sup>+</sup> and simulations have been performed in reduced dimensions, quantum mechanical models have so far not been able to provide a concluding explanation for the angular shifts. To advance the debate whether it is rather the interaction of the free electron with the Coulomb field or rather the non-ADK like ionization behaviour, i.e. the electron dynamics prior to ionization in molecules that leads to the observed shift, a semi-classical model has been applied in this work: the classical trajectory calculations provide a simple approach to testing the influence of the anisotropic Coulomb potential on the final momentum distribution of the photoelectrons, by including or neglecting the Coulomb forces in the propagation. The possible influence of electronic dynamics prior to ionization has been modelled via a modified ionization rate and modified initial momentum values. Within the model, the experimentally observed rotation and its dependence on the final electron momentum and the internuclear distance could

---

be reproduced qualitatively assuming an ADK-like ionization behaviour only, when including the anisotropic Coulomb field of the ion. The counterintuitive stability of the rotation with respect to increasing intensity could be explained as interplay of two rivaling effects: the classical tunnel exit moving closer to the ion, where the influence of the Coulomb field is stronger, and the stronger electric field rivaling the increased Coulomb field at the tunnel exit. Modifying the ADK-like ionization behaviour to mimic the multiple ionization bursts per laser cycle observed in  $\text{H}_2^+$  leads to a broadening of the momentum distribution, but not to a rotation. This suggests that it is rather the Coulomb potential which leads to the observed shift. In further investigations, it would be interesting to study the influence of different wavelengths and elliptical polarization.

The second and third part of the thesis dealt with larger molecules, in particular acetylene ( $\text{C}_2\text{H}_2$ ) and the possibility to gain reaction control over the fragmentation dynamics in polyatomic molecular systems. Together with our experimental collaboration partners Dr. Markus Kitzler and Dr. Xinhua Xie from the Photonics Institute at the Vienna University of Technology, it has been shown for the first time that reaction control in polyatomic molecules can be gained using either the carrier-envelope phase (CEP) of ultrashort laser pulses or the molecular alignment relative to the laser polarization direction as control tool. To analyse field-driven dynamics in such large systems, a multi-scale approach was needed: various different methods such as quantum chemistry to molecular dynamics, semi-classical models and quantum collision theory were therefore applied in the present work.

More specifically, the second part dealt with the fragmentation control of  $\text{C}_2\text{H}_2^{2+}$  by tuning the carrier-envelope phase: for infra-red laser pulses with an intensity around  $1 \times 10^{14} \text{ W/cm}^2$ , a strong modulation of the fragmentation yield with the CEP has been observed experimentally. The yield of the non-fragmented cation and dication, on the other hand, exhibit no or only a very weak dependence on the CEP for the same laser parameters. At higher laser intensities, the CEP dependence of the fragmentation yield decreases and vanishes. In this work, it has been shown that the CEP control over the fragmentation yield relies on the carrier-envelope phase dependent population of the first excited dicationic state, which is dissociative. Several different scenarios for the population of this state have been modelled and compared against each other, including sequential ionization, field driven dipole excitation, recollisional excitation and non-sequential ionization. An energy threshold effect in recollisional ionization was thereby identified as the mechanism responsible for the CEP control: if the recollision energy is tuned to the ionization potential of the transition to the first strongly dissociative



state by choosing an appropriate laser intensity, the dependence of the recollision energy on the CEP can be used as control tool to enhance or suppress fragmentation. Within a semi-classical, one-dimensional model, good agreement between the experiment and the model could be obtained. A difference between experiment and model is a shift in the CEP, which could be attributed to both, simplifications in the model and the determination of the absolute value of CEP in the experiment. The experimentally observed trend for higher intensities is correctly reproduced within the semi-classical model.

The third part of this thesis dealt with the reaction control of acetylene via the relative alignment of the molecular axis and the laser polarization direction. The corresponding experiments were performed at a slightly higher laser intensity around  $4 \times 10^{14}$  W/cm<sup>2</sup>. At these laser parameters, controlling the molecular alignment allows tuning the relative probability for the fragmentation reaction to end in a specific channel ( $\text{C}_2\text{H}_2^{2+}$ ,  $\text{C}_2\text{H}^+ + \text{H}^+$ ,  $\text{CH}_2^+ + \text{C}^+$ ,  $\text{CH}^+ + \text{CH}^+$ ). The alignment control thus allows the channel selective manipulation of the fragmentation reaction. From a theoretical point of view, dealing with alignment-dependent effects is challenging. The alignment sensitivity may arise from several different causes: ionization, excitation and recollision all depend on the relative alignment of the molecular axis to the laser polarization direction. In the present work, the alignment dependence of sequential ionization and subsequent fragmentation of acetylene has been studied using two different models: first, a TD-DFT approach and secondly, a tunnelling approach based on a single particle picture using the Dyson orbital. Although the two models rely on very different approximations, they lead to consistent results and the alignment dependence of several fragmentation channels has been reproduced both qualitatively and quantitatively. For the  $\text{C}_2\text{H}^+ + \text{H}^+$  and the  $\text{CH}^+ + \text{CH}^+$  fragmentation channels, it could be shown that recollisional ionization plays an important role. In this context, it has been shown that the impact ionization, which is generally neglected when studying the alignment dependence of recollisional ionization can be expected to show a considerable alignment dependence at recollisional energies typical in strong-field experiments. This is especially true for ionization from the lower lying  $\sigma_g$  orbital which leads to the population of excited states. The influence of field excitation processes, on the other hand, has been studied but was found to be of minor importance at the experimentally relevant intensities.

Overall, the present work has allowed the interpretation of several experimentally discovered effects and has provided theoretical models for the complex strong-field electronic and nuclear dynamics in molecules. The simplified models devised in this thesis have

---

allowed identifying the underlying physical processes governing the dynamics and have offered many intuitive explanations.

The interaction of strong laser fields with molecules is an exciting and challenging topic. The size of the systems, the presence of the non-spherically symmetric Coulomb potential, the wide range of timescales that have to be considered and many other effects make theoretical research in this field highly demanding. A wide range of scientific contributions has already greatly advanced our understanding of strong-field processes, but to thoroughly understand and to be able to fully exploit the strong-field control over molecular reactions will require further research on the theoretical as well as on the experimental side.

## A. Atomic units [au]

Atomic units form a system of natural units derived from properties of the electron in an hydrogen atom. They are therefore especially suited and often used in atomic and molecular physics. Tables A.1 and A.2 give an overview over several often used conversions and factors.

quantity	physical property	symbol	au	SI	other units
charge	electron charge	$e$	1	$1.602 \times 10^{-19}$ C	
mass	electron mass	$m_e$	1	$9.109 \times 10^{-31}$ kg	$5.486 \times 10^{-4}$ amu
length	Bohr radius	$a_0 = \frac{4\pi\epsilon_0\hbar^2}{m_e e^2}$	1	$5.292 \times 10^{-10}$ m	0.5292 Å
	red. Planck's const.	$\hbar$	1	$1.055 \times 10^{-34}$ Js	
	vacuum permittivity	$4\pi\epsilon_0$	1	$1.113$ C <sup>2</sup> J <sup>-1</sup> m	
energy	Bohr energy (Hartree)	$2E_0 = \frac{\hbar^2}{m_e a_0^2}$	1	$4.360 \times 10^{-18}$ J	27.211 eV
velocity	av. velocity of e in H	$v = \sqrt{\frac{2E_0}{m}}$	1	$c\alpha = \frac{c}{137.036}$ $= 2.187 \times 10^6$ m/s	
time	cycling time in H	$\frac{\tau_0}{2\pi} = \frac{\hbar}{E_0}$	1	2.419 s	24.189 as
E-field	electric field strength	$E$	1	$5.142 \times 10^{11}$ V m <sup>-1</sup>	
	Bohr magnetron	$\mu_B = \frac{e\hbar}{2m_e}$	0.5	$9.274 \times 10^{-24}$ J /T	

Table A.1.: Numerical values for commonly used conversions (four significant digits). ( $c$ ...speed of light,  $\alpha$ ...fine structure constant)

quantity	relation
wavelength	$\omega / [\text{au}] = \frac{45.56}{\lambda[\text{nm}]}$
intensity	$E [\text{au}] = \sqrt{2.849 \times 10^{-17} I [\text{W}/\text{cm}^2]}$ $I [\text{W}/\text{cm}^2] = 3.509 \times 10^{16} E [\text{au}]^2$

Table A.2.: Other useful relations.



## B. Integration schemes

Numerically, integration can be implemented using Riemann sums. However, for precise results, it is desirable to perform integrals analytically if possible or to use numerical quadrature. The following sections summarize some of the integration schemes used in the present work.

### B.1 Overlap integrals of Gaussians type orbitals

Gaussian type orbitals are often used as basis functions in electronic structure calculations. A cartesian Gaussian centered at  $\mathbf{A}$  can thereby be written as [74]

$$G_{ijk}(\mathbf{r}, a, \mathbf{A}) = x_A^i y_A^j z_A^k e^{-a(x_A^2 + y_A^2 + z_A^2)} \quad (\text{B.1})$$

$$= G_i(x, a, A_x) G_j(y, a, A_y) G_z(z, a, A_z) \quad (\text{B.2})$$

where  $x_A$  is given by  $x_A = x - A_x$ , the variable  $a$  is the exponential decay factor and  $G_i(x, a, A_x) = x_A^i e^{-ax_A^2}$ .

The overlap of two different Cartesian Gaussians is thus given by

$$\begin{aligned} \langle G_{ikm}(\mathbf{r}, a, \mathbf{A}) | G_{jln}(\mathbf{r}, b, \mathbf{B}) \rangle = & \\ & \underbrace{\int_{-\infty}^{\infty} G_i(x, a, A_x) G_j(x, b, B_x) dx}_{S_{ij}} \\ & \cdot \int_{-\infty}^{\infty} G_i(y, a, A_y) G_j(y, b, B_y) dy \\ & \cdot \int_{-\infty}^{\infty} G_i(z, a, A_z) G_j(z, b, B_z) dz, \quad (\text{B.3}) \end{aligned}$$

where  $S_{ij}$  denotes the overlap in Cartesian  $x$  direction. These overlaps can be calculated via the Obara-Saika recurrence relations [74] from the analytically known result for the

overlap of two spherical Gaussians

$$S_{00} = \sqrt{\frac{\pi}{p}} e^{-\mu X_{AB}^2}, \quad (\text{B.4})$$

$$S_{i+1,j} = X_{PA} S_{ij} + \frac{1}{2p} (i S_{i-1,j} + j S_{i,j-1}), \quad (\text{B.5})$$

$$S_{i,j+1} = X_{PB} S_{ij} + \frac{1}{2p} (i S_{i-1,j} + j S_{i,j-1}), \quad (\text{B.6})$$

where  $\mathbf{P} = \frac{a\mathbf{A}+b\mathbf{B}}{p}$ ,  $\mu = \frac{ab}{a+b}$ ,  $p = a + b$  and  $X_{AB} = A_x - B_x$ . (The overlaps in the other Cartesian coordinates follow equivalently by replacing  $x$  by  $y$  and  $z$ .)

Another variant of Gaussian type orbitals often used in electronic structure calculations are spherical-harmonic Gaussian type orbitals, which are defined as [74]

$$G_{lm}(\mathbf{r}, a, \mathbf{A}) = S_{lm}(x_A, y_A, z_A) e^{-a(x_A^2 + y_A^2 + z_A^2)}, \quad (\text{B.7})$$

where  $S_{lm}$  are real solid harmonics defined as

$$\begin{pmatrix} S_{lm} \\ S_{l,-m} \end{pmatrix} = \frac{1}{\sqrt{2}} \begin{pmatrix} (-1)^m & 1 \\ -(-1)^m i & i \end{pmatrix} \sqrt{\frac{4\pi}{2l+1}} r^l \begin{pmatrix} Y_{lm}(\theta, \phi) \\ Y_{l,-m}(\theta, \phi) \end{pmatrix}, \quad (\text{B.8})$$

and  $Y_{lm}$  are normalized spherical harmonics in the phase convention of Condon and Shortly, i.e.  $Y_{00} = \frac{1}{2\sqrt{\pi}}$ ,  $Y_{1,-1} = \frac{1}{2}\sqrt{\frac{3}{2\pi}} \sin(\theta)e^{-i\phi}$ ,  $Y_{1,1} = -\frac{1}{2}\sqrt{\frac{3}{2\pi}} \sin(\theta)e^{i\phi}, \dots$

The spherical-harmonic Gaussian type orbitals can be related to the Cartesian Gaussian type orbitals [74], which leads to the following transformation matrices for the s to f orbitals ( $l = 0$  to  $l = 3$ )

$$G_{00} = G_{000} \quad (\text{B.9})$$

$$\begin{pmatrix} G_{1,-1} \\ G_{1,0} \\ G_{1,1} \end{pmatrix} = \begin{pmatrix} 0 & 1 & 0 \\ 0 & 0 & 1 \\ 1 & 0 & 0 \end{pmatrix} \begin{pmatrix} G_{1,0,0} \\ G_{0,1,0} \\ G_{0,0,1} \end{pmatrix} \quad (\text{B.10})$$

$$\begin{pmatrix} G_{2,-2} \\ G_{2,-1} \\ G_{2,0} \\ G_{2,1} \\ G_{2,2} \end{pmatrix} = \begin{pmatrix} 0 & 0 & 0 & 0 & \sqrt{3} & 0 \\ 0 & \sqrt{3} & 0 & 0 & 0 & 0 \\ 1 & 0 & -\frac{1}{2} & 0 & 0 & -\frac{1}{1} \\ 0 & 0 & 0 & \sqrt{3} & 0 & 0 \\ 0 & 0 & -\frac{\sqrt{3}}{2} & 0 & 0 & \frac{\sqrt{3}}{2} \end{pmatrix} \begin{pmatrix} G_{0,0,2} \\ G_{0,1,1} \\ G_{0,2,0} \\ G_{1,0,1} \\ G_{1,1,0} \\ G_{2,0,0} \end{pmatrix} \quad (\text{B.11})$$

$$\begin{pmatrix} G_{3,-3} \\ G_{3,-2} \\ G_{3,-1} \\ G_{3,0} \\ G_{3,1} \\ G_{3,2} \\ G_{3,3} \end{pmatrix} = \begin{pmatrix} 0 & \frac{3}{2}\sqrt{\frac{5}{2}} & 0 & -\frac{1}{2}\sqrt{\frac{5}{2}} & 0 & 0 & 0 & 0 & 0 & 0 \\ 0 & 0 & 0 & 0 & 0 & \sqrt{15} & 0 & 0 & 0 & 0 \\ 0 & -\frac{1}{2}\sqrt{\frac{3}{2}} & 0 & -\frac{1}{2}\sqrt{\frac{3}{2}} & 0 & 0 & 0 & 0 & 2\sqrt{\frac{3}{2}} & 0 \\ 0 & 0 & 0 & 0 & -\frac{3}{2} & 0 & -\frac{3}{2} & 0 & 0 & 1 \\ -\frac{1}{2}\sqrt{\frac{3}{2}} & 0 & -\frac{1}{2}\sqrt{\frac{3}{2}} & 0 & 0 & 0 & 0 & 2\sqrt{\frac{3}{2}} & 0 & 0 \\ 0 & 0 & 0 & 0 & \frac{\sqrt{15}}{2} & 0 & -\frac{\sqrt{15}}{2} & 0 & 0 & 0 \\ \frac{1}{2}\sqrt{\frac{5}{2}} & 0 & -\frac{3}{2}\sqrt{\frac{5}{2}} & 0 & 0 & 0 & 0 & 0 & 0 & 0 \end{pmatrix} \begin{pmatrix} G_{0,0,3} \\ G_{0,1,2} \\ G_{0,2,1} \\ G_{0,3,0} \\ G_{1,0,2} \\ G_{1,1,1} \\ G_{1,2,0} \\ G_{2,0,1} \\ G_{2,1,0} \\ G_{3,0,0} \end{pmatrix} \quad (\text{B.12})$$

## B.2 Integrals of spherical harmonics

Spherical harmonics are used often as basis for an expansion in the azimuthal and polar angles,  $\theta$  and  $\phi$ . Overlaps of two and three spherical harmonics can be calculated analytically

$$\int_0^{2\pi} \int_0^\pi \sin\theta Y_{lm}^*(\theta, \phi) Y_{l'm'}(\theta, \phi) d\theta d\phi = \delta_{l,l'} \delta_{m,m'}, \quad (\text{B.13})$$

$$\int_0^{2\pi} \int_0^\pi \sin\theta Y_{l_1 m_1}(\theta, \phi) Y_{l_2 m_2}(\theta, \phi) Y_{l_3 m_3}(\theta, \phi) d\theta d\phi = \sqrt{\frac{\hat{l}_1 \hat{l}_2 \hat{l}_3}{4\pi}} \begin{pmatrix} l_1 & l_2 & l_3 \\ 0 & 0 & 0 \end{pmatrix} \begin{pmatrix} l_1 & l_2 & l_3 \\ m_1 & m_2 & m_3 \end{pmatrix}, \quad (\text{B.14})$$

where  $\hat{l} = 2l + 1$  and  $\begin{pmatrix} l_1 & l_2 & l_3 \\ m_1 & m_2 & m_3 \end{pmatrix}$  denotes the Wigner 3-j symbol.

## B.3 Integration on the sphere

If integrals in  $\theta$  and  $\phi$  have to be performed numerically, a better option than gridding  $\theta$  and  $\phi$  equidistantly and summing over the weighted function  $f(\theta_i, \phi_i) \sin\theta_i$ , is to use the spherical Lebedev quadrature. Using a Lebedev grid of order  $L$  with  $n \sim (L+1)^2/3$  points, it is possible to exactly perform the integral over any spherical harmonic  $Y_{lm}$  with  $l \leq L$

$$\int_0^{2\pi} \int_0^\pi \sin(\theta) Y_{lm}(\theta, \phi) d\theta d\phi = \sum_{i=1}^n Y_{lm}(\theta_i, \phi_i) w_i, \quad (\text{B.15})$$

where  $(\theta_i, \phi_i)$  are the Lebedev points and  $w_i$  the Lebedev weights. Fortran routines generating the Lebedev points and weights for a certain quadrature order have been written by J. Burkardt and can be found in Reference [192].





## C. Derivation of Eq. V.4.6

To derive Eq. V.4.6, we start from the Lippmann-Schwinger equation for a two center potential  $V(\mathbf{r}) = V_l(\mathbf{r}) + V_r(\mathbf{r}) = -\frac{1}{|\mathbf{r}-\mathbf{\Delta}|} - \frac{1}{|\mathbf{r}+\mathbf{\Delta}|}$ , where  $2\Delta$  is the distance between the two cores.

$$\begin{aligned}\chi_{2C}^- &= u_0 + \sum_{n=1}^{\infty} (G^- V)^n u_0 \\ &= u_0 + \sum_{n=1}^{\infty} (G^- V_l)^n u_0 + \sum_{n=1}^{\infty} (G^- V_r)^n u_0 + \underbrace{G^- V_l G^- V_r u_0 + G^- V_r G^- V_l u_0 + \dots}_{\text{mixed terms}}\end{aligned}$$

where  $G^-$  is the Green's function for incoming wave boundary conditions  $G^-(\mathbf{r}, \mathbf{r}') = \frac{1}{4\pi} \frac{e^{ik|\mathbf{r}-\mathbf{r}'|}}{|\mathbf{r}-\mathbf{r}'|}$ . The unperturbed wavefunction  $u_0$  is given by

$$u_0(\mathbf{r}) = e^{i\mathbf{k}\mathbf{r}}. \quad (\text{C.1})$$

The short hand notation  $(G^- V)u_0$  denotes the following integral expression

$$(G^- V)u_0 = \int d\mathbf{r}' G^-(\mathbf{r}, \mathbf{r}') V(\mathbf{r}') u_0(\mathbf{r}'). \quad (\text{C.2})$$

In the following step, the mixed terms containing both,  $V_l$  and  $V_r$  are neglected. Hence, while the interaction with one core only is kept to all orders, the interaction with both cores is only kept to first order.

$$\begin{aligned}\chi_{2C}^- &= u_0 + \sum_{n=1}^{\infty} (G^- V_l)^n u_0 + \sum_{n=1}^{\infty} (G^- V_r)^n u_0 + \underbrace{G^- V_l G^- V_r u_0 + G^- V_r G^- V_l u_0 + \dots}_{\text{mixed terms}} \\ &\approx u_0 + \sum_{n=1}^{\infty} (G^- V_l)^n u_0 + \sum_{n=1}^{\infty} (G^- V_r)^n u_0,\end{aligned}$$

Since the single center Coulomb wave for a potential  $V_0 = \frac{1}{r}$  is given by

$$\chi_C^-(\mathbf{k}, \mathbf{r}) = u_0(\mathbf{r}) + \sum_{n=1}^{\infty} (G^- V_0)^n u_0 = u_0(\mathbf{r}) + u_1(\mathbf{r}) + \dots,$$

using the translation properties of the Green's function, one finds that

$$\begin{aligned} (G^- V_l)^n u_0(\mathbf{k}, \mathbf{r}) &= e^{i\mathbf{k}\Delta} u_n(\mathbf{k}, \mathbf{r} - \Delta) \\ (G^- V_r)^n u_0(\mathbf{k}, \mathbf{r}) &= e^{-i\mathbf{k}\Delta} u_n(\mathbf{k}, \mathbf{r} + \Delta) \end{aligned}$$

and hence

$$\begin{aligned} \chi_{2C}^-(\mathbf{k}, \mathbf{r}) &= u_0(\mathbf{k}, \mathbf{r}) + e^{i\mathbf{k}\Delta} \sum_{n=1}^{\infty} u_n(\mathbf{k}, \mathbf{r} - \Delta) + e^{-i\mathbf{k}\Delta} \sum_{n=1}^{\infty} u_n(\mathbf{k}, \mathbf{r} + \Delta) \\ &= u_0(\mathbf{k}, \mathbf{r}) + e^{i\mathbf{k}\Delta} \left( \chi_C^-(\mathbf{k}, \mathbf{r} - \Delta) - u_0(\mathbf{k}, \mathbf{r} - \Delta) \right) \\ &\quad + e^{-i\mathbf{k}\Delta} \left( \chi_C^-(\mathbf{k}, \mathbf{r} + \Delta) - u_0(\mathbf{k}, \mathbf{r} + \Delta) \right) \\ &= -u_0(\mathbf{k}, \mathbf{r}) + e^{i\mathbf{k}\Delta} \chi_C^-(\mathbf{k}, \mathbf{r} - \Delta) + e^{-i\mathbf{k}\Delta} \chi_C^-(\mathbf{k}, \mathbf{r} + \Delta). \end{aligned}$$

## D. Derivation of Eq. (V.4.8)

To derive Eq. (V.4.8), we start from Eq. (I.5.1). Integrating over  $d\Omega_s$  and  $d\Omega_e$  (where the index  $s$  was used instead of index 1 in Eq. (I.5.1) and  $e$  instead of 2) leads to

$$\frac{d\sigma}{dE_1} \propto \frac{k_s k_e}{k_i} \int d\Omega_s \int d\Omega_e |T_{fi}|^2 \delta(E_f - E_i). \quad (\text{D.1})$$

In the following derivation, the exchange term will be neglected for simplicity. Inserting Eq. V.4.7 leads to

$$\begin{aligned} \frac{d\sigma}{dE_e} &\propto \frac{k_s k_e}{k_i} \int d\Omega_1 \int d\Omega_2 \left| \int dr r^2 \int d\Omega \int dr' r'^2 \int d\Omega' \right. \\ &\cdot \frac{1}{(2\pi)^{\frac{3}{2}}} \sum_{l_e, m_e} Y_{l_e, m_e}(\hat{\mathbf{k}}_e) Y_{l_e, m_e}^*(\hat{\mathbf{r}}'_e) (-i)^{l_e} e^{i\sigma_{l_e}^{k_e}} \frac{1}{k_e r'} F_{l_e}^*(\eta_e, k_e r') \cdot \\ &\cdot \frac{1}{(2\pi)^{\frac{3}{2}}} \sum_{l_s, m_s} Y_{l_s, m_s}(\hat{\mathbf{k}}_s) Y_{l_s, m_s}^*(\hat{\mathbf{r}}_e) (-i)^{l_s} e^{i\sigma_{l_s}^{k_s}} \frac{1}{k_s r} F_{l_s}^*(\eta_s, k_s r) \\ &\cdot \sum_l \frac{4\pi}{2l+1} \begin{pmatrix} r^l < \\ r^{l+1} > \end{pmatrix} \sum_m Y_{l, m}^*(\hat{\mathbf{r}}') Y_{l, m}(\hat{\mathbf{r}}) \\ &\cdot \sum_{\alpha} f_{\alpha}(r') Y_{l_{\alpha}, m_{\alpha}}(r') \\ &\cdot \left. \frac{1}{(2\pi)^{\frac{3}{2}}} \sum_{l_i} 4\pi i^{l_i} j_{l_i}(k_i r) \sum_{m_i} Y_{l_i, m_i}^*(\hat{\mathbf{k}}_i) Y_{l_i, m_i}(\hat{\mathbf{r}}_i) \right|^2, \end{aligned}$$

where the expressions from Eq. (V.4.10) was used. The expansion of  $\frac{1}{|\mathbf{r}-\mathbf{r}'|}$  in spherical harmonics was used in the fourth line of the equation, where  $r_<$  and  $r_>$  denote the smaller and larger value of  $r$  and  $r'$  respectively.

D. Derivation of Eq. (V.4.8)

---

Rearranging the sums, this leads to

$$\begin{aligned} \frac{d\sigma}{dE_e} \propto & \frac{k_s k_e}{k_i} \int d\Omega_1 \int d\Omega_2 \left| \int dr \int dr' \cdot \frac{(4\pi)^3}{(2\pi)^{\frac{9}{2}}} \frac{1}{k_e k_s} \right. \\ & \cdot \sum_{\alpha} \sum_{l,m} \sum_{l_e, m_e} \sum_{l_s, m_s} \sum_{l_i, m_i} f_{\alpha}(r') \frac{4\pi}{2l+1} \left( \frac{r'_{\leq}}{r'_{>}} \right)^{l_i} (-i)^{l_e+l_s} e^{i(\sigma_{l_e}^{k_e} + \sigma_{l_s}^{k_s})} \\ & \cdot Y_{l_e, m_e}(\hat{\mathbf{k}}_e) Y_{l_s, m_s}(\hat{\mathbf{k}}_s) Y_{l_i, m_i}^*(\hat{\mathbf{k}}_i) F_{l_e}^*(\eta_e, k_e r') F_{l_s}^*(\eta_s, k_s r) j_{l_i}(k_i r) \\ & \cdot \left. \underbrace{\int d\Omega Y_{l_s, m_s}^*(\hat{\mathbf{r}}_e) Y_{l, m}(\hat{\mathbf{r}}) Y_{l_i, m_i}(\hat{\mathbf{r}}_i)}_{G_{-m_s, m, m_i}^{l_s, l, l_i} (-1)^{m_s}} \underbrace{\int d\Omega' Y_{l_e, m_e}^*(\hat{\mathbf{r}}'_e) Y_{l, m}(\hat{\mathbf{r}}') Y_{l_{\alpha}, m_{\alpha}}(r')}_{G_{-m_e, -m, m_{\alpha}}^{l_e, l, l_{\alpha}} (-1)^{m_e+m}} \right|^2, \end{aligned}$$

where the Gaunt coefficients,  $G$  are defined in Eq. (V.4.9) and the following relations were used

$$\begin{aligned} Y_{l, m}^*(\hat{\mathbf{r}}) &= (-1)^m Y_{l, -m}(\hat{\mathbf{r}}) \\ \int d\Omega Y_{l_1, m_1}(\hat{\mathbf{r}}_e) Y_{l_2, m_2}(\hat{\mathbf{r}}) Y_{l_3, m_3}(\hat{\mathbf{r}}) &= G_{m_1, m_2, m_3}^{l_1, l_2, l_3}. \end{aligned}$$

The absolute value squared can be expanded as

$$\begin{aligned} \left| \sum_{\alpha, l, \dots} A_{\alpha, l, \dots} Y_{l_e, m_e} Y_{l_s, m_s} \right|^2 &= \sum_{\alpha, l, \dots} A_{\alpha, l, \dots} Y_{l_e, m_e} Y_{l_s, m_s} \cdot \sum_{\alpha', l', \dots} A_{\alpha', l', \dots}^* Y_{l_e, m_e}^* Y_{l_s, m_s}^* \\ &= \sum_{k, l, \dots, k', l', \dots} A_{\alpha, l, \dots} A_{\alpha', l', \dots}^* Y_{l_e, m_e} Y_{l_e, m_e}^* Y_{l_s, m_s} Y_{l_s, m_s}^*. \end{aligned}$$

This allows performing the integrals over  $d\Omega_s$  and  $d\Omega_e$  analytically using

$$\int d\Omega Y_{l, m}(\hat{\mathbf{k}}_s) Y_{l', m'}^*(\hat{\mathbf{k}}_s) = \delta_{l, l'} \delta_{m, m'},$$

which, after collecting the remaining sums back to an absolute value squared, leads to

$$\begin{aligned} \frac{d\sigma}{dE_e} \propto & \frac{k_s k_e}{k_i} \left( \frac{1}{k_e k_s} \right)^2 \frac{(4\pi)^8}{(2\pi)^9} \sum_{l_e, m_e} \sum_{l_s, m_s} \\ & \cdot \left| \sum_{\alpha} \sum_{l, m} \sum_{l_i, m_i} \frac{1}{2l+1} (i)^{l_i} Y_{l_i, m_i}^*(\hat{\mathbf{k}}_i) (-1)^m \right. \\ & \cdot \left. \int dr \int dr' \frac{r'_{\leq}}{r'_{>}} f_{\alpha}(r') j_{l_i}(k_i r) F_{l_e}^*(\eta_e, k_e r') F_{l_s}^*(\eta_s, k_s r) G_{-m_s, m, m_i}^{l_s, l, l_i} G_{-m_e, -m, m_{\alpha}}^{l_e, l, l_{\alpha}} \right|^2 \end{aligned}$$

Taking into account that the  $G_{m_1, m_2, m_3}^{l_1, l_2, l_3}$  are zero, unless  $m_1 + m_2 + m_3 = 0$ , this expression is equivalent to Eq. (V.4.8) without exchange. The derivation including the symmetrization or antisymmetrization of the wavefunction proceeds analogously.



## E. Derivation of Eq. V.4.11

Assuming that the initial state wavefunction  $\Psi_i(\mathbf{r}_1, \mathbf{r}_2) \equiv \phi_D(\mathbf{r}_1)e^{i\mathbf{k}_i\mathbf{r}_2}$  satisfies the following effective two particle Schrödinger equation

$$\left(E - T - V_{\text{ion}}(\mathbf{r}_1)\right)\phi_D(\mathbf{r}_1)e^{i\mathbf{k}_i\mathbf{r}_2} = 0,$$

where  $T$  denotes the kinetic energy operator and setting

$$\left(E - T - V_{\text{ion}}(\mathbf{r}_1) - U(\mathbf{r}_2)\right)\phi_D(\mathbf{r}_1)\chi^+(\mathbf{k}_i, \mathbf{r}_2) = 0,$$

allows writing

$$\phi_D(\mathbf{r}_1)\chi^+(\mathbf{k}_i, \mathbf{r}_2) = \phi_D(\mathbf{r}_1)e^{i\mathbf{k}_i\mathbf{r}_2} + \frac{1}{E - T - V(\mathbf{r}_1) + i\epsilon}U(\mathbf{r}_2)\phi_D(\mathbf{r}_1)\chi^+(\mathbf{k}_i, \mathbf{r}_2). \quad (\text{E.1})$$

For the final channel,  $\Psi^-(\mathbf{r}_1, \mathbf{r}_2)$ , we write the following effective two particle equations

$$\left(E - T - V_{\text{ion}}(\mathbf{r}_1) - V_{\text{ion}}(\mathbf{r}_2) - \frac{1}{|\mathbf{r}_1 - \mathbf{r}_2|}\right)\Psi^-(\mathbf{r}_1, \mathbf{r}_2) = 0$$

and

$$\left(E - T - V_{\text{ion}}(\mathbf{r}_1)\right)\chi^-(k_e, \mathbf{r}_1)e^{-i\mathbf{k}_s\mathbf{r}_2} = 0,$$

which leads to

$$\Psi^-(\mathbf{r}_1, \mathbf{r}_2) = \chi^-(k_e, \mathbf{r}_1)e^{-i\mathbf{k}_s\mathbf{r}_2} + \frac{1}{E - T - V_{\text{ion}}(\mathbf{r}_1)}\left(V_{\text{ion}}(\mathbf{r}_2) + \frac{1}{|\mathbf{r}_1 - \mathbf{r}_2|}\right)\Psi^-(\mathbf{r}_1, \mathbf{r}_2). \quad (\text{E.2})$$

Inserting Eqs. (E.1) and (E.2) into the expression for the transition matrix element, Eq. (I.5.2), leads to the following two potential expression

$$T = \langle\Psi^-|V_{\text{ion}}(\mathbf{r}_2) - U(\mathbf{r}_1) + \frac{1}{|\mathbf{r}_1 - \mathbf{r}_2|}|\phi_D\chi^+\rangle.$$

Since the final channel wavefunction  $\Psi^-(\mathbf{r}_1, \mathbf{r}_2)$  can be written as

$$\Psi^-(\mathbf{r}_1, \mathbf{r}_2) = \chi^-(k_e, \mathbf{r}_1)\chi^-(k_s, \mathbf{r}_2) + \frac{1}{E - T - V_{\text{ion}}(\mathbf{r}_1) - V_{\text{ion}}(\mathbf{r}_2) - \frac{1}{|\mathbf{r}_1 - \mathbf{r}_2|} - i\varepsilon} \left( V_{\text{ion}}(\mathbf{r}_1) - U(\mathbf{r}_1) + V_{\text{ion}}(\mathbf{r}_2) - U(\mathbf{r}_2) + \frac{1}{|\mathbf{r}_1 - \mathbf{r}_2|} \right) \chi^-(k_e, \mathbf{r}_1)\chi^-(k_s, \mathbf{r}_2),$$

if  $U$  is a good approximation to  $V$  and the influence of  $\frac{1}{|\mathbf{r}_1 - \mathbf{r}_2|}$  is small, then the final channel wavefunction can be approximated as  $\Psi^-(\mathbf{r}_1, \mathbf{r}_2) \approx \chi^-(k_e, \mathbf{r}_1)\chi^-(k_s, \mathbf{r}_2)$ , which leads to

$$T \approx \langle \chi^-(\mathbf{k}_e)\chi^-(\mathbf{k}_s) | V_{\text{ion}}(\mathbf{r}_2) - U(\mathbf{r}_2) + \frac{1}{|\mathbf{r}_1 - \mathbf{r}_2|} | \phi_D \chi^+(\mathbf{k}_i) \rangle. \quad (\text{E.3})$$

Setting  $U = -\frac{2}{r}$  and assuming that  $V_{\text{ion}} - U = 0$  leads to

$$T \approx \langle \chi_C^-(\mathbf{k}_e)\chi_C^-(\mathbf{k}_s) | \frac{1}{|\mathbf{r}_1 - \mathbf{r}_2|} | \phi_D \chi_C^+(\mathbf{k}_i) \rangle, \quad (\text{E.4})$$

where the  $\chi_C^{+/-}$  are Coulomb scattering wave functions for incoming and outgoing boundary conditions.

The following derivation of Eq. (V.4.11) from this expression proceeds analogously to the derivation of Eq. (V.4.8) given in Appendix D.



## F. A note on special functions

In the course of this work, the use of special functions, such as associated Legendre polynomials, spherical Bessel functions, etc. was necessary. Some of these functions are difficult to implement accurately and in general, such calculations were based on or used existing routines. The following table gives an overview over the routines used.

function	author	reference
Legendre functions	J. Burkardt	[193]
spherical Bessel function	A. R. Barnett	[194, 195]
Coulomb functions	A. R. Barnett	[195]
complex Gamma function	T. Oura	[196]
Wigner 3-j function	J. Burkardt	[197]
Runge-Kutta-Fehlberg method	J. Burkardt	[108]



# Bibliography

- [1] P. R. Moulton, *J. Opt. Soc. Am. B* **3**, 125 (1986).
- [2] D. E. Spence, P. N. Kean, and W. Sibbett, *Opt. Lett.* **16**, 42 (1991).
- [3] R. Szipöcs and K. Ferencz, *Opt. Lett.* **19**, 201 (1994).
- [4] D. Strickland and G. Mourou, *Optics Comm.* **56**, 219 (1985).
- [5] T. Brabec and F. Krausz, *Rev. Mod. Phys.* **72**, 545 (2000).
- [6] A. Baltuška, T. Udem, M. Uiberacker, M. Hentschel, E. Gouliemakis, C. Gohle, R. Holzwarth, V. S. Yakovlev, A. Scrinzi, T. W. Hänsch, and F. Krausz, *Nature* **421**, 611 (2003).
- [7] T. Wittmann, B. Horvath, W. Helml, M. G. Schätzel, X. Gu, A. L. Cavalieri, G. G. Paulus, and R. Kienberger, *Nature Phys.* **5**, 357 (2009).
- [8] P. Agostini, F. Fabre, G. Mainfray, G. Petite, and N. K. Rahman, *Phys. Rev. Lett.* **42**, 1127 (1979).
- [9] G. G. Paulus, W. Nicklich, H. Xu, P. Lambropoulos, and H. Walther, *Phys. Rev. Lett.* **72**, 2851 (1994).
- [10] L. Keldysh, *Sov. Phys. JETP* **20**, 1307 (1965).
- [11] A. L'Huillier, L. A. Lompre, G. Mainfray, and C. Manus, *Phys. Rev. Lett.* **48**, 1814 (1982).
- [12] A. McPherson, G. Gibson, H. Jara, U. Johann, T. S. Luk, I. A. McIntyre, K. Boyer, and C. K. Rhodes, *J. Opt. Soc. Am. B* **4**, 595 (1987).
- [13] P. Antoine, A. L'Huillier, and M. Lewenstein, *Phys. Rev. Lett.* **77**, 1234 (1996).
- [14] H. R. Reiss, *Prog. Quant. Electr.* **16**, 1 (1992).

- [15] M. Protopapas, C. H. Keitel, and P. L. Knight, *Rep. Prog. Phys.* **60**, 389 (1997).
- [16] C. J. Joachain, M. Dörr, and N. Kylstra, *Adv. At. Molec. Opt. Phys.* **42**, 225 (2000).
- [17] W. Becker, F. Grasbon, R. Kopold, D. B. Milošević, G. G. Paulus, and H. Walther, *Adv. At. Molec. Opt. Phys.* **48**, 35 (2002).
- [18] A. Scrinzi, M. Y. Ivanov, R. Kienberger, and D. M. Villeneuve, *J. Phys. B: At. Mol. Phys.* **39**, R1 (2006).
- [19] F. Krausz and M. Y. Ivanov, *Rev. Mod. Phys.* **81**, 163 (2009).
- [20] H. R. Reiss, *Phys. Rev. A* **22**, 1786 (1980).
- [21] P. B. Corkum, *Phys. Rev. Lett.* **71**, 1994 (1993).
- [22] M. Lewenstein, P. Balcou, M. Y. Ivanov, A. L’Huillier, and P. B. Corkum, *Phys. Rev. A* **49**, 2117 (1994).
- [23] A. M. Perelomov, V. S. Popov, and M. V. Terent’ev, *Sov. Phys.–JETP* **23**, 924 (1966).
- [24] S. Zherebtsov, T. Fennel, J. Plenge, E. Antonsson, I. Znakovskaya, A. Wirth, O. Herrwerth, F. Süßmann, C. Peltz, I. Ahmad, S. A. Trushin, V. Pervak, S. Karsch, M. J. J. Vrakking, and B. Langer, *Nature Phys.* **7**, 656 (2011).
- [25] M. Krüger, M. Schenk, and P. Hommelhoff, *Nature* **475**, 78 (2011).
- [26] X. M. Tong, Z. X. Zhao, and C. D. Lin, *Phys. Rev. A* **66**, 033402 (2002).
- [27] T. Zuo and A. D. Bandrauk, *Phys. Rev. A* **52**, R2511 (1995).
- [28] R. de Nalda, E. Heesel, M. Lein, N. Hay, R. Velotta, E. Springate, M. Castillejo, and J. P. Marangos, *Phys. Rev. A* **69**, 031804 (2004).
- [29] M. Oppermann, S. J. Weber, L. J. Frasinski, M. Y. Ivanov, and J. P. Marangos, *Phys. Rev. A* **88**, 043432 (2013).
- [30] M. Meckel, A. Staudte, S. Patchkovskii, D. M. Villeneuve, P. B. Corkum, R. Dörner, and M. Spanner, *Nature Phys.* **10**, 594 (2014).
- [31] P. W. Dooley, I. V. Litvinyuk, K. F. Lee, D. M. Rayner, M. Spanner, D. M. Villeneuve, and P. B. Corkum, *Phys. Rev. A* **68**, 023406 (2003).

- 
- [32] J. Itatani, J. Levesque, D. Zeidler, H. Niikura, H. Pepin, J. C. Kieffer, P. B. Corkum, and D. M. Villeneuve, *Nature* **432**, 867 (2004).
- [33] R. Torres, N. Kajumba, J. G. Underwood, J. S. Robinson, S. Baker, J. W. G. Tisch, R. de Nalda, W. A. Bryan, R. Velotta, C. Altucci, I. C. E. Turcu, and J. P. Marangos, *Phys. Rev. Lett.* **98**, 203007 (2007).
- [34] S. Baker *et al.*, *Science* **312**, 424 (2006).
- [35] M. F. Kling, C. Siedschlag, A. J. Verhoef, J. I. Khan, M. Schultze, T. Uphues, Y. Ni, M. Uiberacker, M. Drescher, F. Krausz, and M. J. J. Vrakking, *Science* **312**, 246 (2006).
- [36] S. Gräfe and M. Y. Ivanov, *Phys. Rev. Lett.* **99**, 163603 (2007).
- [37] M. Kremer, B. Fischer, B. Feuerstein, V. L. B. de Jesus, V. Sharma, C. Hofrichter, A. Rudenko, U. Thumm, C. D. Schröter, R. Moshhammer, and J. Ullrich, *Phys. Rev. Lett.* **103**, 213003 (2009).
- [38] I. Znakovskaya, P. von den Hoff, S. Zherebtsov, A. Wirth, O. Herrwerth, M. Vrakking, R. de Vivie-Riedle, and M. Kling, *Phys. Rev. Lett.* **103**, 103002 (2009).
- [39] B. Fischer, M. Kremer, T. Pfeifer, B. Feuerstein, V. Sharma, U. Thumm, C. Schröter, R. Moshhammer, and J. Ullrich, *Phys. Rev. Lett.* **105**, 223001 (2010).
- [40] I. Znakovskaya, P. von den Hoff, N. Schirmel, G. Urbasch, S. Zherebtsov, B. Bergues, R. de Vivie-Riedle, K.-M. Weitzel, and M. F. Kling, *Phys. Chem. Chem. Phys.* **13**, 8653 (2011).
- [41] T. Baumert, M. Grosser, R. Thalweiser, and G. Gerber, *Phys. Rev. Lett.* **67**, 3753 (1991).
- [42] E. D. Potter, J. L. Herek, S. Pedersen, Q. Liu, and A. H. Zewail, *Nature* **355**, 66 (1992).
- [43] G. G. Paulus, F. Grasbon, H. Walter, P. Villoresi, M. Nisoli, S. Stagira, E. Priori, and S. D. Silvestri, *Nature* **414**, 182 (2001).
- [44] M. Nisoli, G. Sansone, S. Stagira, S. De Silvestri, C. Vozzi, M. Pascolini, L. Poletto, P. Villoresi, and G. Tondello, *Phys. Rev. Lett.* **91**, 213905 (2003).
- [45] Y. Liu, X. Liu, Y. Deng, C. Wu, H. Jiang, and Q. Gong, *Phys. Rev. Lett.* **106**, 073004 (2011).

- [46] X. Xie, K. Doblhoff-Dier, S. Roither, M. S. Schöffler, D. Kartashov, H. Xu, T. Rathje, G. G. Paulus, A. Baltuška, S. Gräfe, and M. Kitzler, *Phys. Rev. Lett.* **109**, 243001 (2012).
- [47] X. Xie, K. Doblhoff-Dier, H. Xu, S. Roither, M. S. Schöffler, D. Kartashov, S. Erattupuzha, T. Rathje, G. G. Paulus, K. Yamanouchi, A. Baltuška, S. Gräfe, and M. Kitzler, *Phys. Rev. Lett.* **112**, 163003 (2014).
- [48] M. Kling, C. Siedschlag, I. Znakovskaya, A. Verhoef, S. Zherebtsov, F. Krausz, M. Lezius, and M. Vrakking, *Mol. Phys.* **106**, 455 (2008).
- [49] I. Znakovskaya, P. von den Hoff, G. Marcus, S. Zherebtsov, B. Bergues, X. Gu, Y. Deng, M. Vrakking, R. Kienberger, F. Krausz, R. de Vivie-Riedle, and M. Kling, *Phys. Rev. Lett.* **108**, 063002 (2012).
- [50] A. S. Alnaser, M. Kübel, R. Siemering, B. Bergues, N. G. Kling, K. J. Betsch, Y. Deng, J. Schmidt, Z. A. Alahmed, A. M. Azzeer, J. Ullrich, I. Ben-Itzhak, R. Moshhammer, U. Kleineberg, F. Krausz, R. de Vivie-Riedle, and M. F. Kling, *Nature Communications* **5**, 3800 (2013).
- [51] R. R. Freeman, P. H. Bucksbaum, H. Milchberg, S. Darack, D. Schumacher, and M. E. Geusic, *Phys. Rev. Lett.* **59**, 1092 (1987).
- [52] R. M. Potvliege, E. Mese, and S. Vučić, *Phys. Rev. A* **81**, 053402 (2010).
- [53] N. B. Delone and V. P. Kraїnov, *Physics-Uspekhi* **41**, 469 (1998).
- [54] M. Y. Ivanov, M. Spanner, and O. Smirnova, *J. Mod. Opt.* **52**, 165 (2005).
- [55] A. Messiah, *Quantum Mechanics* (Dover Publications, 1999).
- [56] M. V. Ammosov, N. Delone, and V. Kraїnov, *Sov. Phys. JETP* **64**, 1191 (1986).
- [57] V. P. Krainov, *J. Opt. Soc. Am. B* **14**, 425 (1997).
- [58] G. Yudin and M. Y. Ivanov, *Phys. Rev. A* **64**, 013409 (2001).
- [59] N. B. Delone and V. P. Krainov, *J. Opt. Soc. Am. B* **8**, 1207 (1991).
- [60] V. S. Popov, *Physics-Uspekhi* **47**, 855 (2004).
- [61] F. H. M. Faisal, *J. Phys. B: At. Mol. Phys.* **6**, L89 (1973).

- 
- [62] B. Piraux and K. Rzazewski, eds., *Super-Intense Laser-Atom Physics* (Klower Academic Publishers, 2001).
- [63] T. Brabec, M. Y. Ivanov, and P. B. Corkum, *Phys. Rev. A* **54**, R2551 (1996).
- [64] A. Rudenko, K. Zrost, T. Ergler, A. B. Voitkiv, B. Najjari, V. L. B. de Jesus, B. Feuerstein, C. D. Schröter, R. Moshhammer, and J. Ullrich, *J. Phys. B: At. Mol. Phys.* **38**, L191 (2005).
- [65] S. P. Goreslavski, G. G. Paulus, S. V. Popruzhenko, and N. I. Shvetsov-Shilovski, *Phys. Rev. Lett.* **93**, 233002 (2004).
- [66] B. H. Bransden and C. J. Joachain, *Physics of Atoms and Molecules* (Pearson Education Limited, 1983).
- [67] A. D. Bandrauk, F. Fillion-Gourdeau, and E. Lorin, *J. Phys. B: At. Mol. Phys.* **46**, 153001 (13).
- [68] C. C. Chirilă, N. J. Kylstra, R. M. Potvliege, and C. J. Joachain, *Phys. Rev. A* **66**, 063411 (2002).
- [69] H. R. Reiss, *Phys. Rev. Lett.* **101**, 043002 (2008).
- [70] H. R. Reiss, *Phys. Rev. Lett.* **101**, 159901(E) (2008).
- [71] D. J. Tannor, *Introduction to quantum mechanics: a time-dependent perspective* (University Science Books, 2007).
- [72] M. Baer, *Chem. Phys. Lett.* **35**, 112 (1975).
- [73] F. Jensen, *Computational Chemistry* (John Wiley & Sons Ltd, 1999).
- [74] T. Helgaker, P. Jørgensen, and J. Olsen, *Molecular Electronic-Structure Theory* (John Wiley and Sons, Ltd., 2012).
- [75] C. Møller and M. S. Plesset, *Phys. Rev.* **46**, 618 (1934).
- [76] K. Andersson, P. Å. Malmqvist, B. O. Roos, A. J. Sadlej, and K. Wolinski, *J. Phys. Chem.* **94**, 5483 (1990).
- [77] J. Finley, P. Malmqvist, B. O. Roos, and L. Serrano-Andrés, *Chem. Phys. Lett.* **288**, 299 (1998).
- [78] G. Czycholl, *Theoretische Festkörperphysik* (Springer, 2007).

- [79] W. Kohna and L. J. Sham, Phys. Rev. **140**, A1133 (1965).
- [80] U. von Barth and L. Hedin, J. Phys. C: Sol. State Phys. **5**, 1629 (1972).
- [81] J. P. Perdew and A. Zunger, J. Phys. B: At. Mol. Phys. **23**, 5048 (1981).
- [82] J. P. Perdew and Y. Wang, Phys. Rev. B **45**, 13244 (1992).
- [83] M. A. L. Marques and E. K. U. Gross, Ann. Rev. Phys. Chem. **55**, 427 (2004).
- [84] H. Lischka, R. Shepard, F. B. Brown, and I. Shavitt, Int. J. Quant. Chem. **20**, 91 (1981).
- [85] R. Shepard, I. Shavitt, R. M. Pitzer, D. C. Comeau, M. Pepper, H. Lischka, P. G. Szalay, R. Ahlrich, F. B. Brown, and J. Zhao, Int. J. Quant. Chem. **34**, 149 (1988).
- [86] H. Lischka, R. Shepard, R. M. Pitzer, I. Shavitt, M. Dallos, T. Müller, P. G. Szalay, M. Setz, G. S. Kedziora, S. Yabushita, and Z. Zhang, Phys. Chem. Chem. Phys. **3**, 664 (2001).
- [87] H. Lischka, T. Müller, P. G. Szalay, I. Shavitt, R. M. Pitzer, and R. Shepard, WIREs **1**, 191 (2001).
- [88] H. Lischka, R. Shepard, I. Shavitt, R. M. Pitzer, M. Dallos, T. Müller, P. G. Szalay, F. B. Brown, R. Ahlrichs, H. J. Böhm, A. Chang, D. C. Comeau, R. Gdanitz, H. Dachsel, C. Ehrhardt, M. Ernzerhof, P. Höchtl, S. Irle, G. Kedziora, T. Kovar, V. Parasuk, M. J. M. Pepper, P. Scharf, H. Schiffer, M. Schindler, M. Schüler, M. Seth, E. A. Stahlberg, J.-G. Zhao, S. Yabushita, Z. Zhang, M. Barbatti, S. Matsika, M. Schuurmann, D. R. Yarkony, S. R. Brozell, E. V. Beck, J.-P. Blaudeau, M. Ruckebauer, B. Sellner, F. Plasser, and J. J. Szymczak, *COLUMBUS, an ab initio electronic structure program, release 7.0* (2012).
- [89] “Molcas webpage,” (2014), available at <http://www.molcas.org>.
- [90] X. Andrade, J. Alberdi-Rodriguez, D. A. Strubbe, M. J. T. Oliveira, F. Nogueira, A. Castro, J. Muguerza, A. Arruabarrena, S. G. Louie, a. Aspuru-Guzik, A. Rubio, and M. A. L. Marques, J. Phys.: Cond. Matt. (2012).
- [91] A. Casto, H. Appel, M. Oliveira, C. A. Rozzi, X. Andrade, F. Lorenzen, M. A. L. Marques, E. K. U. Gross, and A. Rubio, Phys. Stat. Sol. B (2006).
- [92] M. A. L. Marques, A. Castro, G. F. Bertscha, and A. Rubio, Comput. Phys. Commun. (2003).



- 
- [93] H. Ehrhardt, K. Jung, G. Knoth, and P. Schlemmer, *Z. Phys. D-Atoms, Molecules and Clusters* **1**, 3 (1986).
- [94] M. Gell-Mann and M. L. Goldberger, *Phys. Rev.* **91**, 398 (1953).
- [95] C. J. Joachain, *Quantum Collision Theory*, Vol. 1 and 2 (North-Holland publishing company, 1975).
- [96] H.-D. Meyer, U. Manthe, and L. S. Cederbaum, *Chem. Phys. Lett.* **165**, 73 (1990).
- [97] R. Car and M. Parrinello, *Phys. Rev. Lett.* **55**, 2471 (1985).
- [98] J. C. Tully, *J. Chem. Phys.* **93**, 1061 (1990).
- [99] C. Leforestier, R. H. Bisseling, C. Cerjan, M. D. Feit, R. Friesner, A. Guldberg, A. Hammerich, G. Jolicard, W. Karrlein, H.-D. Meyer, N. Lipkin, O. Roncero, and R. Kosloff, *J. Chem. Phys.* **94**, 59 (1991).
- [100] M. D. Feit, J. J. A. Fleck, and A. Steiger, *J. Chem. Phys.* **47**, 412 (1982).
- [101] M. Kreuzer, “Quantum theory,” (2009).
- [102] R. Kosloff and H. Tal-Ezer, *Chem. Phys. Lett.* **127**, 223 (1986).
- [103] D. Neuhauser, *J. Chem. Phys.* **90**, 2611 (1990).
- [104] J. G. Muga, J. P. Palao, B. Navarro, and I. L. Egusquiza, *Phys. Rep.* (2004).
- [105] A. Scrinzi, *Phys. Rev. A* **81**, 053845 (2010).
- [106] E. Fehlberg, *Low-order classical Runge-Kutta formulas with stepsize control and their application to some heat transfer problems*, Tech. Rep. R-315 (National Aeronautics and Space Administration, 1969).
- [107] E. Fehlberg, *Computing* , 61 (1970).
- [108] J. Burkardt, “Runge-Kutta-Fehlberg routine,” (2004), available at [http://people.sc.fsu.edu/~jburkardt/f\\_src/rkf45/rkf45.f90](http://people.sc.fsu.edu/~jburkardt/f_src/rkf45/rkf45.f90), access: 2014-05-08.
- [109] J. E. Gentle, *Random Number Generation and Monte Carlo Methods* (Springer-Verlag New York, Inc., 2003).
- [110] D. Comtois, D. Zeidler, H. Pépin, J. C. Kieffer, D. M. Villeneuve, and P. B. Colkum, *J. Phys. B: At. Mol. Phys.* **38**, 1923 (2005).

- [111] M. Abu-samha, D. Dimitrovski, and L. B. Madsen, *J. Phys. B: At. Mol. Phys.* **41**, 245601 (2008).
- [112] Z. Walters and O. Smirnova, *J. Phys. B: At. Mol. Phys.* **43** (2010).
- [113] S. Gräfe, J. Doose, and J. Burgdörfer, *J. Phys. B: At. Mol. Phys.* **45**, 055002 (2012).
- [114] A. Staudte, S. Patchkovskii, D. Pavičić, H. Akagi, O. Smirnova, D. Zeidler, M. Meckel, D. M. Villeneuve, R. Dörner, M. Y. Ivanov, and P. B. Corkum, *Phys. Rev. Lett.* **102**, 033004 (2009).
- [115] M. Busuladžić, A. Gazibegović-Busuladžić, and D. B. Milošević, *Phys. Rev. A* **80**, 013420 (2009).
- [116] M. Odenweller, N. Takemoto, A. Vredenburg, K. Cole, K. Pahl, J. Titze, L. P. H. Schmidt, T. Jahnke, R. Dörner, and A. Becker, *Phys. Rev. Lett.* **107**, 143004 (2011).
- [117] K.-J. Yuan and A. D. Bandrauk, *Phys. Rev. A* **83**, 063422 (2011).
- [118] J. Wu, M. Meckel, S. Voss, H. Sann, M. Kunitski, L. P. H. Schmidt, A. Czasch, H. Kim, T. Jahnke, and R. Dörner, *Phys. Rev. Lett.* **108**, 043002 (2012).
- [119] M. Spanner, S. Gräfe, S. Chelkowski, D. Pavičić, M. Meckel, D. Zeidler, A. B. Bardon, B. Ulrich, A. D. Bandrauk, D. M. Villeneuve, R. Dörner, P. B. Corkum, and A. Staudte, *J. Phys. B: At. Mol. Phys.* **45**, 194011 (2012).
- [120] K. J. Yuan and A. D. Bandrauk, *J. Phys. B: At. Mol. Phys.* **45**, 105301 (2012).
- [121] S. Zou, A. Kondorskiy, G. Mil'nikov, and H. Nakamura, *J. Chem. Phys.* **122**, 084112 (2005).
- [122] N. Takemoto and A. Becker, *Phys. Rev. Lett.* **105**, 203004 (2010).
- [123] A. Santana, J. M. G. Llorente, and V. Delgado, *J. Phys. B: At. Mol. Phys.* **34**, 2371 (2001).
- [124] N. Takemoto and A. Becker, *Phys. Rev. A* **84**, 023401 (2011).
- [125] M. Bashkansky, P. H. Bucksbaum, and D. W. Schumacher, *Phys. Rev. Lett.* **60**, 2458 (1988).
- [126] N. I. Shvetsov-Shilovski, D. Dimitrovski, and L. B. Madsen, *Phys. Rev. A* **85**, 023428 (2012).

- 
- [127] A. N. Pfeiffer, C. Cirelli, A. S. Landsman, M. Smolarski, D. Dimitrovski, L. B. Madsen, and U. Keller, *Phys. Rev. Lett.* **109**, 083002 (2012).
- [128] C. P. J. Martiny, M. Abu-samha, and L. B. Madsen, *Journal of Physics B: Atomic, Molecular and Optical Physics* **42**, 161001 (2009).
- [129] G. N. Gibson, M. Li, C. Guo, and J. Neira, *Phys. Rev. Lett.* **79**, 2022 (1997).
- [130] T. K. Kjeldsen, L. B. Madsen, and J. P. Hansen, *Phys. Rev. A* **74**, 035402 (2006).
- [131] G. Lagmago Kamta and A. D. Bandrauk, *Phys. Rev. A* **70**, 011404(R) (2004).
- [132] M. Shapiro and P. Brumer, *Quantum Control of Molecular Processes* (Wiley, New York, 2012).
- [133] P. Brumer and M. Shapiro, *Chem. Phys. Lett.* **126**, 541 (1986).
- [134] D. Tannor and S. A. Rice, *J. Chem. Phys.* **83**, 5013 (1985).
- [135] D. Tannor, R. Kosloff, and S. A. Rice, *J. Chem. Phys.* **85**, 5805 (1986).
- [136] A. P. Peirce, M. A. Dahleh, and H. Rabitz, *Phys. Rev. A* **37**, 4950 (1988).
- [137] W. M. Haynes, ed., *CRC Handbook of Chemistry and Physics*, 93rd ed. (CRC press, 2012).
- [138] E. Ventura, M. Dallos, and H. Lischka, *J. Chem. Phys.* **118**, 1702 (2003).
- [139] M. Peric and S. D. Peyerimhoff, *J. Chem. Phys.* **102**, 3685 (1994).
- [140] P. Plessis and P. Marmet, *Int. J. of Mass Spect. and Ion Proc.* **70**, 23 (1986).
- [141] M. Peric, B. Engels, and M. Hanrath, *Chem. Phys.* **238**, 33 (1998).
- [142] M. Peric and B. Engels, *Chem. Phys.* **238**, 47 (1998).
- [143] E. M. L. Ohrendorf, F. Tarantelli, and L. S. Cederbaum, *J. Chem. Phys.* **92**, 2984 (1990).
- [144] R. Thissen, J. Delwiche, J. M. Robbe, D. Duflot, J. P. Flament, and J. H. D. Eland, *J. Chem. Phys.* **99**, 6590 (1993).
- [145] B. D. Esry and H. R. Sadeghpour, *Phys. Rev. A* **68**, 042706 (2003).

- [146] X. Urbain, B. Fabre, E. M. Staicu-Casagrande, N. de Ruelle, V. M. Andrianarijaoana, J. Jureta, J. H. Posthumus, A. Saenz, E. Baldit, and C. Cornaggia, *Phys. Rev. Lett.* **92**, 163004 (2004).
- [147] C. Cornaggia and P. Hering, *Phys. Rev. A* **62**, 023403 (2000).
- [148] H. Cherkani-Hassani, S. Cherkani-Hassani, D. S. Belic, J. J. Jureta, J. Lecointre, and P. Defrance, *Euro. Phys. J. D* **58**, 85 (2010).
- [149] H. Cherkani-Hassani, S. Cherkani-Hassani, D. S. Belic, J. J. Jureta, J. Lecointre, and P. Defrance, *Euro. Phys. J. D* **58**, 95 (2010).
- [150] H. Cherkani-Hassani, S. Cherkani-Hassani, D. S. Belic, J. J. Jureta, J. Lecointre, and P. Defrance, *Euro. Phys. J. D* **58**, 75 (2010).
- [151] S. J. King and S. D. Price, *J. Chem. Phys.* **127**, 174307 (2007).
- [152] M. Gryzinski, *Phys. Rev.* **138**, A336 (1965).
- [153] N. A. Medvedev, A. E. Volkov, N. S. Shcheblanov, and B. Rethfeld, *Phys. Rev. B* **82**, 125425 (2010).
- [154] S. Chelkowski and A. Bandrauk, *Phys. Rev. A* **71**, 053815 (2005).
- [155] A. Jaron-Becker, *Selected Topics in Quantum Electronics*, *IEEE Journal of* **18** (2012).
- [156] J. L. Hansen, L. Holmegaard, J. H. Nielsen, H. Stapelfeldt, D. Dimitrovski, and L. B. Madsen, *J. Phys. B: At. Mol. Phys.* **45**, 015101 (2012).
- [157] T. K. Kjeldsen, C. Z. Bisgaard, L. B. Madsen, and H. Stapelfeldt, *Phys. Rev. A* **71**, 013418 (2005).
- [158] R. Velotta, N. Hay, M. B. Mason, M. Castillejo, and J. P. Marangos, *Phys. Rev. Lett.* **87**, 183901 (2001).
- [159] X. X. Zhou, X. M. Tong, Z. X. Zhao, and C. D. Lin, *Phys. Rev. A* **71**, 061801(R) (2005).
- [160] X. Y. Jia, W. D. Li, J. Fan, J. Liu, and J. Chen, *Phys. Rev. A* **77**, 063407 (2008).
- [161] H. Akagi, T. Otobe, A. Staudte, A. Shiner, F. Turner, R. Dörner, D. Villeneuve, and P. Corkum, *Science* **325**, 1364 (2009).

- 
- [162] O. Smirnova, Y. Mairesse, S. Patchkovskii, N. Dudovich, D. Villeneuve, P. B. Corkum, and M. Y. Ivanov, *Nature* **460**, 972 (2009).
- [163] P. von den Hoff, I. Znakovskaya, S. Zherebtsov, M. F. Kling, and R. Vivie-Riedle, *Appl. Phys. B* **98**, 659 (2010).
- [164] J. P. Farrell, S. Petretti, J. Förster, B. K. McFarland, L. S. Spector, Y. V. Vanne, P. Decleva, P. H. Bucksbaum, A. Saenz, and M. Gühr, *Phys. Rev. Lett.* **107**, 083001 (2011).
- [165] E. Runge and E. K. U. Gross, *Phys. Rev. Lett.* **52**, 997 (1984).
- [166] M. Musia and R. J. Bartlett, *Chem. Phys. Lett.* **384**, 210 (2004).
- [167] S. Petretti, A. Saenz, A. Castro, and P. Decleva, *Chem. Phys.* **414**, 45 (2013).
- [168] R. Murray, M. Spanner, S. Patchkovskii, and M. Y. Ivanov, *Phys. Rev. Lett.* **106**, 173001 (2011).
- [169] R. Murray, W.-K. Liu, and M. Y. Ivanov, *Phys. Rev. A* **81**, 023413 (2010).
- [170] J. Ortigoso, M. Rodriguez, M. Gupta, and B. Friedrich, *J. Chem. Phys.* **110**, 3870 (1999).
- [171] M. Swart, P. T. van Duijnen, and J. G. Snijders, *J. Mol. Spectrosc.* **458**, 11 (1998).
- [172] National Institute of Standards and Technology <http://cccbdb.nist.gov/exp2.asp?casno=74862>, access: 2014-06-24.
- [173] T. S. Zyubina, Y. A. Dyakov, S. H. Lin, A. D. Bandrauk, and A. M. Mebel, *J. Chem. Phys.* **123**, 134320 (2005).
- [174] D. Duflot, J.-M. Robbe, and J.-P. Flament, *J. Chem. Phys.* **102**, 355 (1994).
- [175] V. R. Bhardwaj, D. M. Rayner, D. M. Villeneuve, and P. B. Corkum, *Phys. Rev. Lett.* **87**, 253003 (2001).
- [176] M. Lein, *J. Phys. B: At. Mol. Phys.* **36**, L155 (2003).
- [177] S. Weber, M. Oppermann, M. Ivanov, and J. Marangos, *J. Mod. Opt.* **60**, 1379 (2013).
- [178] J. Liu, D. Liu, and Y. Zhou, *Physica Scripta* **85**, 025329 (2012).

- [179] A. Senftleben, T. Pflüger, X. R. dna O. Al-Hagan, B. Najjari, D. Madison, A. Dorn, and J. Ullrich, *J. Phys. B: At. Mol. Phys.* **43**, 081002 (2010).
- [180] A. Senftleben, O. Al-Hagan, T. Pflüger, X. Ren, D. Madison, A. Dorn, and J. Ullrich, *J. Chem. Phys.* **133**, 044302 (2010).
- [181] J. Colgan, O. Al-Hagan, D. H. Madison, A. J. Murray, and M. S. Pindzola, *J. Phys. B: At. Mol. Phys.* **42**, 171001 (2009).
- [182] J. Colgan, M. S. Pindzola, F. Robicheaux, C. Kaiser, A. J. Murray, and D. H. Madison, *Phys. Rev. Lett.* **101**, 233201 (2008).
- [183] C. R. Stia, O. A. Fojón, P. F. Weck, J. Hanssen, and R. D. Rivarola, *J. Phys. B: At. Mol. Phys.* **36**, L257 (2003).
- [184] J. C. A. Lower, E. Ali, S. Bellm, E. Weigold, A. Harris, C. G. Ning, and D. Madison, *Phys. Rev. A* **88**, 062705 (2013).
- [185] O. Al-Hagan, C. Kaiser, D. Madison, and A. J. Murray, *Nature Phys.* **5**, 59 (2008).
- [186] C. Champion, J. Hanssen, and P.-A. Hervieux, *J. Chem. Phys.* **117**, 197 (2002).
- [187] C. Champion, J. Hanssen, and P.-A. Hervieux, *J. Chem. Phys.* **121**, 9423 (2004).
- [188] J. Gao, D. H. Madison, and J. L. Peacher, *Phys. Rev. A* **72**, 020701(R) (2005).
- [189] J. D. Bultth-Williams, S. M. Bellma, D. B. Jones, H. Chaluvadi, D. H. Madison, C. G. Ning, B. Lohmann, and M. J. Brunger, *J. Chem. Phys.* **136**, 024304 (2012).
- [190] M. Brauner, J. S. Briggs, and H. Klar, *J. Phys. B: At. Mol. Phys.* **22**, 2265 (1989).
- [191] L. F. Canto and M. S. Hussein, *Scattering Theory of Molecules, Atoms and Nuclei* (World Scientific, 2013).
- [192] J. Burkardt, “Routine for spherical Lebedev integration,” (2010), available at [http://people.sc.fsu.edu/~jburkardt/f\\_src/sphere\\_lebedev\\_rule/sphere\\_lebedev\\_rule.f90](http://people.sc.fsu.edu/~jburkardt/f_src/sphere_lebedev_rule/sphere_lebedev_rule.f90), access:2014-04-14.
- [193] J. Burkardt, “Routine for Legendre polynomials,” (1999), available at [http://people.sc.fsu.edu/~jburkardt/f\\_src/legendre\\_polynomial/legendre\\_polynomial.f90](http://people.sc.fsu.edu/~jburkardt/f_src/legendre_polynomial/legendre_polynomial.f90), access: 2014-02-06.
- [194] A. R. Barnett, “Routine for Coulomb functions,” (1991), available at <http://www.fresco.org.uk/programs/barnett/COUL90.FOR>, access: 2014-04-24.

- [195] A. R. Barnet, “Routine for Bessel functions,” (1991), available at <http://www.fresco.org.uk/programs/barnett/SBESJY.FOR>, access: 2014-04-24.
- [196] T. Ooura, “Routine for Gamma function,” (1996), available at <http://www.kurims.kyoto-u.ac.jp/~ooura/gamerf.html>.
- [197] J. Burkhardt, “Routine for Clebsch-Gordan coefficients,” (2007), available at [http://people.sc.fsu.edu/~jburkardt/f77\\_src/clebsch\\_gordan/clebsch\\_gordan.f](http://people.sc.fsu.edu/~jburkardt/f77_src/clebsch_gordan/clebsch_gordan.f)